

Reconstructing Primordial Curvature Perturbations via Scalar-Induced Gravitational Waves with LISA

Jonas El Gammal^{1, a}, Aya Ghaleb,^b Gabriele Franciolini^{2, c}, Theodoros Papanikolaou,^{def} Marco Peloso,^{gh} Gabriele Perna^{3, gh}, Mauro Pieroni,^c Angelo Ricciardone,^{ij} Robert Rosati^{4, k}, Gianmassimo Tasinato,^{blm}

Matteo Braglia,ⁿ Jacopo Fumagalli,^o Jun'ya Kume,^{ghr} Enrico Morgante,^{pq} Germano Nardini,^a Davide Racco,st Sébastien Renaux-Petel,^u Hardi Veermäe,^v Denis Werth,^u and Ivonne Zavala^b

(For the LISA Cosmology Working Group)

^a*Department of Mathematics and Physics, University of Stavanger, NO-4036 Stavanger, Norway*

^b*Department of Physics, Faculty of Science and Engineering, Swansea University, Singleton Park, SA2 8PP, Swansea, United Kingdom*

^c*CERN, Theoretical Physics Department, Esplanade des Particules 1, Geneva 1211, Switzerland*

^d*Scuola Superiore Meridionale, Largo San Marcellino 10, 80138 Napoli, Italy*

^e*Istituto Nazionale di Fisica Nucleare (INFN), Sezione di Napoli, Via Cinthia 21, 80126 Napoli, Italy*

^f*National Observatory of Athens, Lofos Nymfon, 11852 Athens, Greece*

^g*Dipartimento di Fisica e Astronomia "G. Galilei", Università degli Studi di Padova, via Marzolo 8, I-35131 Padova, Italy*

^h*INFN, Sezione di Padova, via Marzolo 8, I-35131 Padova, Italy*

ⁱ*Dipartimento di Fisica "Enrico Fermi", Università di Pisa, Largo Bruno Pontecorvo 3, Pisa I-56127, Italy*

^j*INFN, Sezione di Pisa, Largo Bruno Pontecorvo 3, Pisa I-56127, Italy*

^k*NASA Marshall Space Flight Center, Huntsville, AL 35812, USA*

^l*Dipartimento di Fisica e Astronomia, Università di Bologna*

^m*INFN, Sezione di Bologna, I.S. FLAG, viale B. Pichat 6/2, 40127 Bologna, Italy*

¹Corresponding author: jonas.el.gammal@rwth-aachen.de

²Project coordinator: gabriele.franciolini@cern.ch

³Corresponding author: gabriele.perna@phd.unipd.it

⁴Project coordinator: robert.j.rosati@nasa.gov, NASA Postdoctoral Program Fellow

ⁿCenter for Cosmology and Particle Physics, New York University, 726 Broadway, New York, NY 10003, USA

^oDepartament de Física Quàntica i Astrofísica and Institut de Ciències del Cosmos (ICC), Universitat de Barcelona, Martí i Franquès 1, 08028 Barcelona, Spain

^pDipartimento di Fisica, Università di Trieste, Strada Costiera 11, I-34151 Trieste, Italy

^qINFN, Sezione di Trieste, Via Valerio 2, 34127 Trieste, Italy

^rResearch Center for the Early Universe (RESCEU), Graduate School of Science, The University of Tokyo, Hongo 7-3-1 Bunkyo-ku, Tokyo 113-0033, Japan

^sInstitut für Theoretische Physik, ETH Zürich, Wolfgang-Pauli-Str. 27, 8093 Zürich, Switzerland

^tPhysik-Institut, Universität Zürich, Winterthurerstrasse 190, 8057 Zürich, Switzerland

^uInstitut d'Astrophysique de Paris, UMR 7095 du CNRS et de Sorbonne Université, 98 bis bd Arago, 75014 Paris, France

^vKeemilise ja bioloogilise füüsika instituut, Rävala pst. 10, 10143 Tallinn, Estonia

ABSTRACT: Many early universe scenarios predict an enhancement of scalar perturbations at scales currently unconstrained by cosmological probes. These perturbations source gravitational waves (GWs) at second order in perturbation theory, leading to a scalar-induced gravitational wave (SIGW) background. The LISA detector, sensitive to mHz GWs, will be able to constrain curvature perturbations in a new window corresponding to scales $k \in [10^{10}, 10^{14}] \text{Mpc}^{-1}$, difficult to probe otherwise. In this work, we forecast the capabilities of LISA to constrain the source of SIGWs using different approaches: *i*) agnostic, where the spectrum of curvature perturbations is binned in frequency space; *ii*) template-based, modeling the curvature power spectrum based on motivated classes of models; *iii*) ab initio, starting from first-principles model of inflation featuring an ultra-slow roll phase. We compare the strengths and weaknesses of each approach. We also discuss the impact on the SIGW spectrum of non-standard thermal histories affecting the kernels of SIGW emission and non-Gaussianity in the statistics of the curvature perturbations. Finally, we propose simple tests to assess whether the signal is compatible with the SIGW hypothesis. The pipeline used is built into the [SIGWAY](#) code.

Contents

1	Introduction	1
2	Early universe models leading to enhanced curvature spectra	5
2.1	Single field inflation	5
2.2	Multi-field inflation	6
2.3	Other classes of models	7
2.4	A simple benchmark scenario: single field USR	7
3	Modeling the curvature power spectrum	9
3.1	Model independent parameterization: binned spectrum approach	10
3.2	Analytical templates for curvature spectra	11
3.2.1	Smooth templates	11
3.2.2	Templates with oscillations	12
3.3	Computation of \mathcal{P}_ζ in single field USR scenarios	14
4	Computation of the scalar-induced GW background	18
4.1	Source of GWs at second order in the scalar perturbations	19
4.2	Radiation-dominated era	21
4.3	Transition from an early matter-dominated to the radiation-dominated era	22
4.4	Computation of SIGW with the binned spectrum approach	23
4.5	Non-Gaussian imprints on the SIGW spectrum	23
5	Mock signal reconstructions with the SGWBinner and SIGWAY codes	26
5.1	Data streams from LISA TDI channels	27
5.1.1	Instrumental noise	28
5.1.2	Astrophysical foregrounds	29
5.2	Analysis of the simulated data	31
6	Results	33
6.1	Binned spectrum method	34
6.2	Template based method	36
6.2.1	Smooth spectra	36
6.2.2	Spectra with oscillations	41
6.3	Single field USR inference	46
6.4	Non standard thermal histories	49
6.5	Non-Gaussian effects on SIGWs	51
7	Testing the scalar-induced hypothesis	56
8	Conclusions	59

A SIGWAY code: technicalities	63
A.1 Perturbations in USR scenarios: code structure	63
A.2 Computation of SIGWs from the spectrum of curvature perturbations	64
A.3 Computation of SIGWs using binned coefficients	65
A.4 Computation of SIGWs including primordial NGs	65
A.5 Inference	67
B Challenges with binned analyses and a large number of bins	67
C Testing the resolvability of Non-Gaussian corrections: Additional plots	70
D Testing the scalar-induced hypothesis: Additional plots	70

1 Introduction

The Laser Interferometer Space Antenna (LISA) [1] represents a groundbreaking gravitational wave (GW) observatory aimed to probe and impact our understanding of fundamental physics, astronomy, and cosmology [2–4]. With the first-ever direct probe of the stochastic gravitational-wave background (SGWB) in the millihertz frequency range, LISA provides the opportunity to unveil processes that occurred in the first stages of the Universe, including inflation [5, 6]. Probing a primordial SGWB at millihertz frequencies corresponds to exploring comoving scales that lie between those accessible to ground-based GW interferometers and those probed by pulsar-timing arrays, cosmic microwave background (CMB), or large-scale structure surveys. These scales correspond to comoving wavenumbers in the range $k \sim [10^{10}, 10^{14}] \text{Mpc}^{-1}$. Several cosmological models (see e.g. refs. [7–10] for reviews) predict a measurable SGWB at these scales, often without any other complementary distinctive signature, placing LISA in a unique position to test these scenarios.

Inflationary models exhibiting amplified scalar fluctuations are one of the candidates for sourcing an SGWB in the LISA frequency band. Enhanced scalar fluctuations generate scalar-induced gravitational waves (SIGWs) at second order in perturbations [11–20], resulting in a potentially large SGWB. Amplified scalar fluctuations naturally arise in single-field inflationary scenarios with features in the potential like those leading to ultra-slow-roll (USR) phases, multi-field setups, and mechanisms such as preheating or early matter-dominated eras. Intriguingly, the same perturbations that seed the SIGWs can also trigger the formation of primordial black holes (PBHs) [21–25]. SIGWs in the millihertz frequency band arise in correspondence with the asteroidal-mass window for PBHs, a viable candidate for addressing the dark matter puzzle [26–28]. By detecting or setting upper bounds on SIGWs, LISA would not only shed light on the inflationary epoch but also on dark matter and non-astrophysical black hole formation channels. This makes SIGWs a high-gain, well-motivated target for LISA.

SIGWs are also powerful tools to investigate non-Gaussianity (NG) in the early universe since their production is highly sensitive to the statistical properties of scalar curvature fluctuations [29–38]. NG is typically characterized by parameters such as f_{NL} , which quantifies NG at the bispectrum level (three-point correlation function), and τ_{NL} , which appears in the trispectrum (four-point correlation function). Earlier analysis have focused on contributions to the SIGW involving f_{NL} , [39–50]. More recent studies have extended this analysis to higher-order NG terms [45, 51–53]. Recently, a Fisher forecast analysis for LISA about NG has been performed in [53]. The tensor power spectrum of SIGWs is directly related to the four-point correlation function of the curvature fluctuations. Such a correlation function has both connected and disconnected contributions. While the latter contributes only to the Gaussian SIGW power spectrum, the former is directly linked to the trispectrum through the τ_{NL} parameter [49], which is the key observable to constrain NG from SIGWs.

The detection and characterization of the primordial SGWB is one of the most challenging objectives of the LISA mission [54]. LISA is a signal-dominated detector, where a multitude of transient or quasi-monochromatic events overlap in time and frequency with the stochastic superposition of all unresolved astrophysical events and, potentially also with a significant primordial SGWB. Additionally, the stationary component of the instrumental noise can mimic a SGWB to some extent. Completing the LISA science program for the SGWB therefore requires:

- i)* Determining whether a primordial SGWB is present in the data.
- ii)* Reconstructing the SGWB frequency shape and, if possible, its statistical properties.
- iii)* Setting upper limits on cosmological sources of SGWB not supported by the data.
- iv)* Constraining the parameters of the most likely SGWB source candidates.

ESA and NASA plan to address these tasks through the so-called “global fit”, a data analysis procedure where modules fitting each class of sources (galactic binaries, supermassive black hole binaries, SGWB, etc.) iterate until convergence [54]. Recently, successful prototype global fit analyses became available in the literature [55–57], tested on the *Sangria* LISA Data Challenge (LDC) dataset [58], which contains no primordial SGWB. It is still an open question how the global fit should support a primordial SGWB search, and how the SGWB properties should be represented in the detection catalogs that the space agencies will publish. A recent study [59] has attempted to perform an SGWB search directly on the global fit residual.

In this work, we aim to bridge these gaps by providing elements of the global fit SGWB module useful for the tasks *i)* - *iv)* in the presence of a SGWB due to SIGWs. To develop and test our rationale, we work in the limit that all resolvable events have been precisely reconstructed¹, leaving us with data containing the stationary component of the noise, the

¹Although this optimistic working hypothesis may seem unrealistic, it is the correct one to use in a global fit module. All current implementations of the global fit are based on a blocked Gibbs sampling scheme, where each source type is sampled independently, assuming a perfect subtraction of the other source types.

SIGW background, and the foregrounds from the unresolved galactic and extragalactic binaries.

As we focus on SIGW sources, we perform an analysis starting from the properties of the source curvature power spectra $\mathcal{P}_\zeta(k)$ of the source, instead of the GW energy density $\Omega_{\text{GW}}(f)$ generated by these power spectra.

Concerning *i)* and *ii)*, we prototype a model-agnostic method that reconstructs the power spectrum $\mathcal{P}_\zeta(k)$ by binning it in frequency space. This approach allows for maximal flexibility in capturing unknown SIGW features. It is however not as agnostic as other generic SGWB searches [60–66] since it requires, by construction, a SIGW source, i.e. a SGWB that can be derived as the proper convolution of a generic $\mathcal{P}_\zeta(f)$. Due to this additional information, the method is expected to be more sensitive to SIGW signals than other fully-agnostic approaches. It can be particularly useful for placing upper bounds on the SIGW amplitude if no signal is detected in the LISA data, or act as a key ingredient for SIGW model selection if a signal is present.

On the other hand, if the computational resources available to the mission allow running the global fit for every SGWB template, several modules for the template-based SIGW reconstruction have been conceived since the first iterations of the global fit.² The advantage of such a possibility is clear: the more signal characterization is included in the search, the higher the sensitivity to that signal. This process also reduces the risk of SGWB misreconstructions that the global fit might absorb into the parameter estimation of other sources. To address the points *i)* and *ii)* above within this framework, we collect several well-motivated inflationary models with known $\mathcal{P}_\zeta(k)$ predictions, we design template classes that effectively parameterize these $\mathcal{P}_\zeta(k)$, and we prototype the SIGW template-based searches for them.

Accurately performing *i)* and *ii)* enables LISA to identify the most favored SIGW models and then proceed with tasks *iii)* and *iv)*. Accordingly, we implement a prototype data analysis pipeline, choosing the USR inflationary setup as a representative example. In particular, we develop a fast numerical algorithm determining $\mathcal{P}_\zeta(k)$ once the inflationary model parameters are known. Thanks to its speed, the algorithm allows for rapid likelihood evaluations in the fundamental-parameter space, enabling direct inference on the USR model parameters from GW data.

As a proof of concept, we further perform inference on $\mathcal{P}_\zeta(k)$ in cosmological scenarios where standard assumptions on Gaussianity of curvature perturbations and on the standard thermal history of the Universe are relaxed. We evaluate the SIGW energy density sourced by non-Gaussian contributions parametrized by τ_{NL} , resorting to the local ansatz emerging from a perturbative expansion of scalar fluctuations. This contribution is known to modify

By periodically alternating which source type is being sampled over, imperfect source subtraction and source type confusion are properly included and fully modeled in the resulting posterior. When working after the global fit, with one sample of the residual as we assume in this work, these possible degeneracies are not fully modeled. Additionally, if the global fit has experienced a convergence failure (the MCMC is still “burning in”), unmodeled source power may still be in the data and lead to false detections of an SGWB. Ref. [59] studies how this convergence failure affects stochastic background recovery in the available prototype global fit residuals.

²See ref. [67] for other template-based reconstructions suitable for inflationary models.

its frequency profile compared to the Gaussian counterpart [41, 42, 46, 49, 52, 53]. Since for models of inflation with local type NG, where the curvature perturbation is dominated by one degree of freedom, τ_{NL} and f_{NL} are related, we take advantage of such a relation to forecast the ability of LISA of probing NG, focusing the analysis on f_{NL} and discussing its implications for τ_{NL} . It is worth mentioning that, as recently argued by [68], the effects of NG on the SIGW background may not always be accurately captured by an expansion around a Gaussian field. Properly accounting for the full impact of intrinsic non-linearities may significantly suppress or enhance the spectrum compared to the predictions based on the local ansatz. Achieving this would require the development of fully non-perturbative approaches to compute the SIGW spectrum, which are beyond the scope of this work. Finally, we perform some diagnostic tests to assess whether the reconstructed signal is consistent with the SIGW hypothesis. Such tests could help to rule out a scalar-induced origin as a viable explanation for some SGWB spectral shapes.

The core of our numerical analysis is implemented in the `SIGWAY` code.³ This stand-alone `Python` code addresses tasks *i) - iv)* for SIGW signals by offering the following functionalities:

- A fast vectorized numerical integrator for computing the SGWB resulting from any spectrum of primordial curvature fluctuations of modes reentering the Hubble radius during radiation domination or a phase of early matter domination.
- An integration algorithm for computing the SGWB assuming a binned spectrum of $\mathcal{P}_\zeta(k)$ for agnostic reconstructions of \mathcal{P}_ζ .
- Solvers for the background- and perturbation equations of motion for the inflaton in a single-field scenario that can be called by the SIGW integrator starting from the inflaton Lagrangian.
- Capabilities for computing the SGWB including non-Gaussian contributions for a lognormal shape of \mathcal{P}_ζ .
- Functionality for pairing to the `SGWBinner` pipeline [61, 62] for computing the LISA likelihood, and performing inference on the parameters governing the primordial curvature fluctuations.

The paper is organized as follows. In Sec. 2 we review some representative models predicting enhanced power spectra of curvature perturbations. In Sec. 3 we identify functional forms that describe the shapes of the aforementioned spectra in terms of effective parameters. In Sec. 4 we describe the analytic and numerical tools that we implement in the `SIGWAY` code. The functionality of the `SGWBinner` code that is relevant for performing inference is briefly described in Sec. 5. Sec. 6 illustrates, for representative benchmark signals, how the elements built in this work help tackle the key tasks *i) - iv)*, including testing whether the SIGW hypothesis is compatible with the putative signal in Sec. 7. Finally, Sec. 8 presents our main conclusions, while App. A and App. B discuss technicalities and subtleties regarding the proposed SIGW signal reconstruction and interpretation.

³<https://github.com/jonasegammal/SIGWAY>

Notation. We indicate with k the comoving wavenumber while with f the associated frequency $f = k/2\pi$. For scales relevant to LISA, we translate wavenumbers in units of Hz using $c = \text{Hz Mpc}/(1.023 \times 10^{14})$. For presentation purposes, we differentiate between frequencies and momenta arbitrarily denoting them with units of Hz and s^{-1} , respectively. As usually done in the literature, we report the GW spectral energy density Ω_{GW} multiplied by the rescaled Hubble rate $h = H_0/(100 \text{ km/s/Mpc})$ squared. Finally, we indicate vectors with bold symbols (e.g. $\vec{x} \equiv \mathbf{x}$) while their magnitude with the lower-case letter.

2 Early universe models leading to enhanced curvature spectra

In this section, we summarise the main classes of models predicting enhanced curvature power spectra at small scales, which can lead to potential GW signatures in LISA.

2.1 Single field inflation

In the simplest models of inflation, a single scalar field known as the inflaton moves gradually down its potential under the influence of Hubble friction, resulting in a slow-roll (SR) phase. The generated fluctuations are nearly scale-invariant, Gaussian, and adiabatic: they freeze on super-Hubble scales, producing a universe that is statistically homogeneous and isotropic [69–73].

In certain models, however, the inflaton potential in the Einstein frame can contain features such as a flat region or a mild bump that causes the field velocity to decrease rapidly in a brief USR⁴ phase [74–79] followed by another SR or a constant-roll phase [80, 81]. The shape of the enhanced spectral features is determined by the amplification of the curvature perturbations during the USR phase, as well as by the specifics of the transition into the USR era. If the field accelerates significantly during that transient epoch, it can cause sizeable spectral modulation, and even be the dominant source of amplification. The resulting perturbations deviate significantly from scale invariance, exhibiting the strongest amplification for wavelengths exiting the horizon around the USR era.

Generically, models of this kind can be subdivided into four categories: *i*) Quasi-inflection points and plateaus [44, 79, 82–112]; *ii*) Upward [113, 114] or downward [114–117] steps; *iii*) Models in which the inflaton rolls through a global minimum/double-well potentials [118–123]; and *iv*) Potentials with stacked features/oscillating potentials [124–130]. It was also suggested that models going beyond a non-minimally coupled inflaton, e.g. within modified gravity theories, can introduce features in terms other than the inflaton potential or the non-minimal coupling [131–147]. See e.g. [148] for a model-building review. Even though the literature on these models is quite vast, many scenarios predict a curvature power spectrum that is enhanced at small scales with similar properties. In particular, most models, especially those in category *i*), produce a single peak in the power spectrum that is approximately captured by a broken power law. However, models with sharp features

⁴We consider a slightly broader definition of USR, which is often characterized by $\eta_H \equiv -\ddot{H}/(2H\dot{H}) = 3$ (or $\eta \equiv \dot{\epsilon}/(H\epsilon) = -6$) and can be realized on a flat plateau. However, models considered in the literature often exhibit a small bump instead, which results in $\eta_H > 3$ due to the curvature of the potential. We will include such deviations in our definition of USR.

can produce spectral oscillations at and after the peak in the power spectrum. Such enhancement mechanisms are mainly in the categories *ii*) and *iii*). Non-standard potentials in category *iv*) can also deviate strongly from this picture.

We finish this section with a note on the theoretical consistency of these enhancing mechanisms. There has been significant debate about the potential impact of loop corrections, induced by the enhanced modes during an USR phase, on long-wavelength scales, with some even challenging the validity of perturbative computations in these scenarios. This discussion is also relevant for the possible interpretation of a stochastic signal as originating from SIGW. The question of whether these corrections can become sufficiently large to undermine the predictive power of inflationary models related to PBH and SIGW has been also explored in Res. [149–159], while other studies have questioned the very existence of these corrections and proposed an argument against their existence [160–164].

2.2 Multi-field inflation

Hybrid/multi-field inflation. Given the high number of degrees of freedom within multi-field inflationary setups, we can separate and control more efficiently two stages responsible respectively for the generation of nearly scale-invariant primordial curvature perturbations on large CMB scales, and for enhanced curvature perturbations on small scales which lead to the production of SIGWs. Hybrid/multi-field models of inflation tend to generate slowly-growing lognormal-like peaks in the curvature power spectrum [165–170] while strong deviations from a geodesic trajectory in field space may lead to sharp peaks and features such as spectral oscillations in \mathcal{P}_ζ [171–177].

Curvaton models Within curvaton scenarios [178], one can realize setups with the curvaton field being characterized by a steep blue spectrum either due to interactions with the inflaton or other degrees of freedom during inflation [179, 180] or due to a non-trivial kinetic term [181, 182]. In particular, within axion-like curvaton setups, the curvaton field is identified with the phase of a complex field whose modulus decreases rapidly during inflation [183–186]. We should also highlight that in any curvaton model the curvature perturbations on small scales originate from non-adiabatic curvaton field fluctuations during inflation, leading to a non-Gaussian probability distribution function for the primordial curvature perturbations [187–190] with important consequences at the level of the SIGW signal [42, 53, 191, 192] (but see also [193]).

Axion-gauge field coupling Enhanced scalar [194] and tensor [194, 195] modes can be produced by gauge fields amplified by their pseudo-scalar $\phi F\tilde{F}$ coupling with a rolling inflaton or spectator [196, 197] axion during inflation. The gauge field amplitude is exponentially sensitive to the axion velocity, thus providing naturally blue signals. These enhanced curvature modes can lead to PBH and SIGW [40, 198–200]. The precise shape of these signals is sensitive to the axion evolution, which is significantly impacted by the backreaction of the amplified gauge fields, which is recently being explored via lattice simulations [201–204].

2.3 Other classes of models

Preheating. During the preheating phase following inflation, as the inflaton field undergoes coherent oscillations around the minimum of its potential, a striking phenomenon emerges: the resonant amplification of quantum inflaton field fluctuations, which drives particle production [205, 206]. These enhanced quantum fluctuations are accompanied by a resonant amplification of the scalar metric fluctuations (usually quoted as metric preheating [207–210]), or, in other terms, with enhanced curvature perturbations, responsible for the generation of SIGWs [211] and potentially for PBH formation [212–214] (see however [215] for an assessment on the role of non-linearities and anharmonicities). Most studies have focused on multi-field inflationary setups since in such scenarios the enhancement of entropic (isocurvature) fluctuations can give rise to the enhancement of the adiabatic/curvature fluctuations in the broad resonance regime [216–221]. This leads to a notable amplification of the primordial curvature power spectrum, deviating from the standard scale-invariant behavior at small scales [222–224]. Interestingly, recent works also suggest that a parametric amplification of the curvature perturbations can occur even in the narrow regime in the case of single field inflation [212–215, 225]. We should also note that these gravitational waves are typically peaked at MHz or GHz frequencies far above those of LISA, although some scenarios do allow for a peak in LISA’s range [226].

Matter Bouncing Scenarios. In non-singular matter bouncing cosmological models [227], the matter contracting phase inevitably amplifies super-horizon curvature perturbations. This enhancement can lead to an enhanced primordial curvature power spectrum on small scales compared to the ones probed by CMB. As these perturbations cross the cosmological horizon, either during the contracting phase [228–230] or the expanding Hot Big Bang phase [231, 232], they can lead to the abundant production of SIGWs.

Early PBH domination. At distances much larger than the mean PBH separation length, a population of PBHs can be viewed as an effective pressureless fluid. One can then treat this PBH fluid within the context of cosmological perturbation theory showing that the PBH energy fluctuations are isocurvature in nature [233, 234] and can convert to adiabatic curvature perturbations in an early matter-dominated era driven by light PBHs ($m_{\text{PBH}} < 10^9 \text{g}$) occurring before BBN. Interestingly enough, these PBH-induced curvature perturbations can source abundant SIGWs detectable by GW observatories [233–235]. Notably, these PBH associated SIGWs [236, 237] can serve as a novel portal to probe primordial non-Gaussianities (NGs) [238, 239] at small scales ($k > \text{Mpc}^{-1}$) as well the underlying gravity theory [240–242] and Hawking evaporation [243–250].

2.4 A simple benchmark scenario: single field USR

In this work, we consider one of the simplest realizations of the single-field scenarios discussed in the previous section. This class of models is described by the inflaton potential in the Einstein frame, $V(\phi)$. The corresponding action can be written as

$$\mathcal{S} = \int d^4x \sqrt{-g} \left(\frac{1}{2} M_{\text{p}}^2 R - \frac{1}{2} (\partial^\mu \phi)^2 - V(\phi) \right), \quad (2.1)$$

where R is the Ricci scalar and M_{P} is the reduced Planck mass. Assuming a flat FLRW background geometry $ds^2 = -dt^2 + a^2 dx_i^2$, where a is the scale factor, the background evolution is governed by the Friedmann equation (dots indicate time derivatives)

$$3M_{\text{P}}^2 H^2 = \dot{\phi}^2/2 + V(\phi), \quad (2.2)$$

with $H = \dot{a}/a$, and the Klein-Gordon equation (a prime denotes a derivative with respect to the field)

$$\ddot{\phi} + 3H\dot{\phi} + V'(\phi) = 0. \quad (2.3)$$

In order to produce an enhancement of perturbations at LISA scales, and at the same time comply with CMB bounds at large scales, the inflationary potential should feature a shallower region or an inflection point, which breaks the SR evolution exponentially decelerating the field velocity.

In the class of models considered here, the dynamics can be understood in relatively simple terms. In SR, the inflaton evolves with a negligible acceleration, and the SR solution gives $\dot{\phi} = -V'/(3H)$. As the inflaton begins to approach the inflection point, the SR conditions are violated primarily due to a rapid change in the second SR parameter. Having almost reached the local maximum ϕ_* , the inflaton will spend $\mathcal{O}(10)$ e -folds crossing it and its evolution is thus dictated by $\ddot{\phi} + 3H\dot{\phi} + \eta_V(\phi_*)H^2(\phi - \phi_*) \simeq 0$, where $\eta_V \equiv M_{\text{P}}^2 V''/V$ denotes the second potential SR parameter. The two solutions of this equation describe two phases: First, a USR-like phase in which the inflaton rapidly decelerates, which leads to an amplification of the power spectrum. Second, a subsequent constant roll or a SR phase that is dual to the initial USR-like phase [81, 251].

The linear superposition of these solutions describes a smooth transition between these epochs. The second SR parameter $\eta_V(\phi_*)$ determines the spectral slope after the peak $n_s - 1 = 3(1 - \sqrt{1 - (4/3)\eta_V(\phi_*)})$. Thus, as exact USR ($\eta_V(\phi_*) = 0$) would produce a scale-invariant spectrum at scales *above* the spectral peak, the violation of scale invariance in the UV is directly related to the deviation from an exact USR.

As an example, we consider the potential given by the rational function proposed in [82] (see also [85, 252])

$$V(\phi) = \frac{\lambda}{12} \phi^2 (vM_{\text{P}})^2 \left(6 - 4b_l \frac{\phi}{vM_{\text{P}}} + 3 \frac{\phi^2}{(vM_{\text{P}})^2} \right) \left(1 + b \frac{\phi^2}{(vM_{\text{P}})^2} \right)^{-2}. \quad (2.4)$$

The presence of an inflection point is enforced by setting

$$b = (1 + b_f) \left[1 - \frac{b_l^2}{3} + \frac{b_l^2}{3} \left(\frac{9}{2b_l^2} - 1 \right)^{2/3} \right], \quad (2.5)$$

where we included a tuning parameter b_f allowing for deviation from perfect inflection points (with $b_f > 0$ the inflection point becomes a shallow minimum). The field ϕ appearing in the action (2.1) is canonically normalized, and minimally coupled to gravity. This is a proxy for more realistic models in which the inflaton field has a quartic potential and couples non-minimally to gravity via a $\xi R\phi^2$ term, see e.g. [83, 84, 99, 253]. After moving

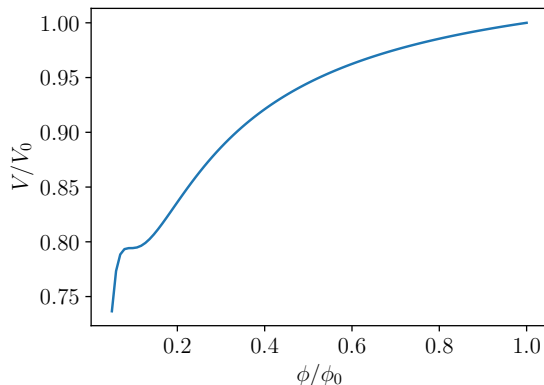


Figure 1. Example of a single field model (2.4), with our benchmark parameters (2.6), leading to an early SR phase consistent with CMB data as well as an USR phase which leads to an enhancement of perturbations within the LISA frequency range.

to the Einstein frame, the factor in the denominator appears, which flattens the potential at large field values. In this case, one would further need to canonically normalize the field, and possibly add logarithmic corrections to the coefficients of the monomials in Eq. (2.4). We do not discuss the origin of such a potential, as our goal is solely to provide a simple representative model to work with.

We define our benchmark potential by choosing the following parameters (close to the ones used in [252])

$$\begin{aligned} \lambda &= 1.4731 \times 10^{-6}, & v &= 0.19688, \\ b_l &= 0.71223, & b_f &= 1.87 \times 10^{-5}, \end{aligned} \quad (2.6)$$

leading to good agreement with CMB (within 3σ of current Planck 2018 data [254]) and at the same time to a peak of the curvature spectrum: $\mathcal{P}_\zeta(k_{\text{peak}}) \simeq 10^{-3}$ at LISA scales. In Eq. (2.6) we report 5 significant digits because of the required tuning of the USR potential [252]. In Sec. 3.3 we describe how to compute the spectrum of curvature perturbations in detail. The benchmark potential is depicted in Fig. 1, where we have arbitrarily normalized the axes using the initial values $\phi_0 = 3M_{\text{P}}$ and $V_0 = 2.3 \cdot 10^{-10} M_{\text{P}}^4$, which are set well before the SR phase that governs the CMB scales.

3 Modeling the curvature power spectrum

Throughout this paper, we describe the metric as a small perturbation of the FLRW metric in the longitudinal (conformal Newtonian) gauge

$$ds^2 = g_{\mu\nu} dx^\mu dx^\nu = -a^2(1 + 2\Phi)d\eta^2 + a^2 \left[(1 - 2\Phi)\delta_{ij} + \frac{1}{2}h_{ij} \right] dx^i dx^j, \quad (3.1)$$

where η is the conformal time, and we neglect vector perturbations and anisotropic stress (and so we can identify the two scalar Bardeen potentials, $\Phi = \Psi$).

At linear order in perturbation theory, the time and momentum dependence of the scalar potential Φ can be factored out by introducing the transfer function $T(\eta, k)$: the

Bardeen’s potential is related to the gauge-invariant comoving curvature perturbation $\zeta(\mathbf{k})$ by

$$\Phi(\eta, \mathbf{k}) = \frac{3 + 3w}{5 + 3w} T(\eta, k) \zeta(\mathbf{k}) \quad (3.2)$$

where w is the equation of state characterizing the fluid dominating the energy density in the universe. In a radiation-dominated universe, $w = 1/3$, and the prefactor becomes $2/3$. As long as a mode k is super-Hubble ($k\eta < 1$), its evolution is frozen and the transfer function tends to 1. For a homogeneous and isotropic universe, the two-point function of curvature perturbations reads

$$\langle \zeta(\mathbf{k}_1) \zeta(\mathbf{k}_2) \rangle \equiv (2\pi)^3 \delta(\mathbf{k}_1 + \mathbf{k}_2) P_\zeta(k_1) \equiv (2\pi)^3 \delta(\mathbf{k}_1 + \mathbf{k}_2) \frac{2\pi^2}{k_1^3} \mathcal{P}_\zeta(k_1), \quad (3.3)$$

where we introduced the dimensionful power spectrum $P_\zeta(k)$, and the dimensionless one $\mathcal{P}_\zeta(k)$. We adopt different methodologies to model the primordial curvature power spectrum $\mathcal{P}_\zeta(k)$ generated in various inflationary models, by:

- Developing a model-independent parametrization of the spectrum, enabling an agnostic reconstruction approach;
- Constructing analytical templates for $\mathcal{P}_\zeta(k)$. These templates are motivated by specific scenarios and are consequently less flexible than the previous case. However, given the lower number of parameters controlling the templates as well as their simple analytical descriptions, they alleviate the computational challenges posed by models which would require expensive computation of the curvature power spectrum;
- Establishing a robust pipeline for the computation of primordial curvature power spectra $\mathcal{P}_\zeta(k)$ for the benchmark model described in Sec. 2.

3.1 Model independent parameterization: binned spectrum approach

In this section, we discuss a parameterization of the power spectrum \mathcal{P}_ζ in terms of a *binned spectrum approach*, which is useful in developing a template-independent procedure for computing the SIGW. We represent the curvature power spectrum as a sum of discrete components defined within small momentum intervals. Specifically, we decompose \mathcal{P}_ζ as a sum of $N - 1$ top hat functions as

$$\mathcal{P}_\zeta(p) = \sum_{i=1}^{N-1} A_i \Theta(p - p_i) \Theta(p_{i+1} - p). \quad (3.4)$$

The coefficients A_i – which can be approximated as constants – represent the amplitude of the spectrum within the i -th bin. The latter is defined within the momentum boundaries p_i and p_{i+1} , using the Heaviside step functions $\Theta(p)$.⁵ Any curvature spectrum \mathcal{P}_ζ can then be associated with a specific vector A_i of the coefficients appearing in Eq. (3.4).

⁵One could extend this approach to include a tilt of the spectrum at each bin and enforcing continuity for adjacent bins, at the cost of doubling the parameters controlling the power in each bin. We leave this, and other possible extensions for future work.

Therefore, our computation does not require an *a priori* choice of a particular template for the momentum dependence of $\mathcal{P}_\zeta(p)$.

The SIGW depends quadratically on \mathcal{P}_ζ using convolution integrals. Hence, we can expect that the ansatz (3.4) allows us to express the SIGW in terms of the double sum of (model-dependent) vector components A_i , contracted over a general, model-independent matrix kernel. In Sec. 4.4 we elaborate a simple procedure aimed at performing this task.

3.2 Analytical templates for curvature spectra

We divide the list of templates into classes depending on their properties. We can define “smooth shapes” and shapes with features.

3.2.1 Smooth templates

We divide this class of templates into two cases:

Lognormal (LN). A typical class of spectral peaks can be characterized by a LN-shape

$$\mathcal{P}_\zeta^{\text{LN}}(k) = \frac{A_s}{\sqrt{2\pi\Delta^2}} \exp\left[-\frac{1}{2\Delta^2} \log^2(k/k_*)\right]. \quad (3.5)$$

Such spectra appear e.g. in a subset of hybrid inflation and curvaton models, as well as from axion-gauge field coupling, see the discussion in Sec. 2. This template can describe scenarios in which the peak is typically narrow and symmetric in log space. Interestingly, this template allows for an analytic derivation of the GW power spectrum in the broad/narrow peak approximations $\Delta \gg 1$ or $\Delta \ll 1$ (see Ref. [255] and improvements in [256]). We will consider the following benchmark scenario choosing

$$\log_{10} A_s = -2.50, \quad \log_{10} \Delta = \log_{10}(0.5) \approx -0.301, \quad \log_{10}(k_*/s^{-1}) = -2.00. \quad (3.6)$$

Broken power law (BPL). Another broad class of spectra is encountered, for instance, in single field inflation and curvaton models and can be described by a BPL

$$\mathcal{P}_\zeta^{\text{BPL}}(k) = A_s \frac{(\alpha + \beta)^\gamma}{\left(\beta (k/k_*)^{-\alpha/\gamma} + \alpha (k/k_*)^{\beta/\gamma}\right)^\gamma}, \quad (3.7)$$

where $\alpha, \beta > 0$ describe respectively the growth and decay of the spectrum around the peak, while γ is an $\mathcal{O}(1)$ model dependent parameter. The normalization is such that $\mathcal{P}_\zeta^{\text{BPL}}(k) = A_s$ at the peak. This template provides a very close approximation to the shape of \mathcal{P}_ζ obtained from single-field USR scenarios. There, one typically finds $\alpha \simeq 5 - |1 - 2\eta_H| \approx 4$ [80, 81, 257], where η_H is the second Hubble SR parameter (see footnote 4) *before* the USR phase, which is typically close to SR, that is, $\eta_H \ll 1$. For this template, it is possible to find an analytic GW spectrum with $\gamma = 1$, see [258]. We will use the following benchmark with parameters

$$\begin{aligned} \log_{10} A_s &= -2.71, & \log_{10}(k_*/s^{-1}) &= -1.58, \\ \alpha &= 3.11, & \beta &= 0.221, & \gamma &= 1.25. \end{aligned} \quad (3.8)$$

which provides a curvature power spectrum whose peak is within LISA’s sensitivity and that fits the spectrum produced in the ab initio USR scenario described below (see Sec. 3.3).

3.2.2 Templates with oscillations

Oscillations in the primordial power spectrum have been extensively studied to seek for deviations from the standard SR inflationary paradigm mainly at scales relevant for CMB or large-scale structure (see e.g. [34, 38, 259, 260]). These oscillations, denoted as primordial features, typically arise due to a sudden transition during inflation [261], occurring over a short time-scale of the order of one e -fold. SIGW provides an opportunity to probe such primordial features at small-scales (\ll Mpc) [173, 175, 262–264]. Specifically, if the mechanism responsible for the enhancement in \mathcal{P}_ζ is active when modes are sufficiently deep inside the horizon, the resulting spectrum exhibits oscillations of order one. Due to their large amplitude, these oscillations could potentially leave their imprints and be detected in the SGWB. This phenomenon can occur in both single-field and multi-field inflationary models. As benchmarks for these large amplitude oscillations, we will consider a small-scale feature induced by a genuine multi-field mechanism and, secondly, weaker oscillations arising from a rapid transition between SR and USR phases in single-field inflation.

Turns in multi-field inflation. In multi-field inflationary setups, a common phenomenon is the presence of turns in the field space, being equivalent to the inflationary trajectory deviating from a geodesic in field space. This bending is quantified through the parameter η_\perp , measuring the acceleration of the inflationary trajectory perpendicular to its direction [265, 266] or equivalently the deviation of the trajectory from a geodesic in the target field space. One then can show that sharp and strong (large η_\perp) turns can lead to the following curvature power spectrum, modulated by order-one rapid oscillations⁶ [171–173]

$$\mathcal{P}_\zeta^{\text{ST}}(\kappa) = \mathcal{P}_\zeta^{\text{env}}(\kappa) \left[1 + (\kappa - 1) \cos \left(2e^{-\frac{\delta}{2}} \eta_\perp \kappa \right) + \sqrt{(2 - \kappa)\kappa} \sin \left(2e^{-\frac{\delta}{2}} \eta_\perp \kappa \right) \right] \Theta(2 - \kappa), \quad (3.9)$$

and the envelope

$$\mathcal{P}_\zeta^{\text{env}}(\kappa) = A_s \exp(-2\eta_\perp \delta) \exp \left[2\sqrt{(2 - \kappa)\kappa} \eta_\perp \delta \right] / [4(2 - \kappa)\kappa], \quad (3.10)$$

where A_s denotes the amplitude of the power spectrum in the absence of transient instability and $\kappa \equiv k/k_*$ with k_* being associated with the maximally enhanced scale, deep inside the cosmological Hubble sphere at the time of the sharp turn. The parameter δ is the duration in e -folds of the turn. $\delta \gtrsim \log \eta_\perp$ stands for broad turns and $\delta \lesssim \log \eta_\perp$ stands for sharp turns. Finally, $\Theta(x)$ denotes the Heaviside theta function.

We define a parameterization in which the oscillations are switched off via the parameter $F \in [0, 1]$, continuously interpolating between (3.9) when $F = 1$ and (3.10) when $F = 0$

$$\mathcal{P}_\zeta(k) = F \mathcal{P}_\zeta^{\text{ST}}(k) + (1 - F) \mathcal{P}_\zeta^{\text{env}}(k). \quad (3.11)$$

We consider the benchmark scenario whose parameters are given by

$$\begin{aligned} \log_{10} A_s &= -1.5, & \log_{10} (k_*/s^{-1}) &= -1.5, \\ \delta &= 0.5, & \eta_\perp &= 14, & F &= 1. \end{aligned} \quad (3.12)$$

⁶Equation (3.9) assumes the entropic field to be massless during the turn. Generalized expressions for other mass choices can be found in [173], where the qualitative features remain analogous.

Rapid transitions between SR and USR phases. In most USR/inflection-point scenarios, the transition from the initial SR phase to the USR-like phase depends on the properties of the potential. In the presence of sufficiently sharp transitions between these phases the spectrum of curvature perturbations deviates from a BPL profile due to oscillatory features.

A fully analytic spectrum can be obtained when the initial SR to USR transition is instantaneous. In that case, the peak can be described as (Eq. (3.8) in [81])

$$\mathcal{P}_\zeta(k) = \frac{\kappa^2}{4\pi} \left| -\frac{\Gamma(1 + \nu_{\text{II}})}{\zeta_1} (\kappa/2)^{-\nu_{\text{II}} + \frac{1}{2}} J_{\nu_{\text{II}}}(\kappa) H_{\nu_{\text{I}}}(\kappa) \right. \\ \left. + \frac{\Gamma(\nu_{\text{II}})}{\zeta_2} (\kappa/2)^{-\nu_{\text{II}} + \frac{3}{2}} [J_{\nu_{\text{II}}}(\kappa) H_{\nu_{\text{I}}-1}(\kappa) + J_{\nu_{\text{II}}+1}(\kappa) H_{\nu_{\text{I}}}(\kappa)] \right|^2, \quad (3.13)$$

where, $\kappa = k/k_*$, $H_\nu(x)$ and $J_\nu(x)$ denote the Hankel- and Bessel functions of the first kind, respectively, k_* is the scale of the mode that exits the Hubble sphere during the SR to USR transition, and ν_{I} and ν_{II} are related to the spectral slopes in the attractor phases before and after the transition as $n_s = 2(2 - \nu)$. The first line does not contribute to the peak and can be omitted in case there is no sensitivity to spectral features away from the peak. The parameters ζ_1 , ζ_2 control the amplitude at the IR (or CMB) scales and the peak, respectively.

This spectrum resembles a broken power law with a modulation around the peak. This modulation has a period of $2k_*$ and is damped as $1/k$. It is generated in an instantaneous SR to USR transition and is typically suppressed or removed when the transition is non-instantaneous [81, 267, 268]. In this way, such oscillations carry information about the evolution of the inflaton during the transition. Moreover, spectral oscillations can be greatly enhanced in some cases. For instance, when the inflaton rolls through a deep minimum before entering the USR phase [118–123].

We can test for the sensitivity of LISA to resolve these oscillations. To this aim, we only consider the second line of the spectrum (3.13), which describes the peak, and consider a generalized form⁷

$$\mathcal{P}_\zeta^{\text{osc}}(k) = F\mathcal{P}_\zeta^{\text{osc,B}}(k) + (1 - F)\mathcal{P}_\zeta^{\text{osc,BPL}}(k), \quad (3.14)$$

where $F \in [0, 1]$ and with

$$\mathcal{P}_\zeta^{\text{osc,B}}(k) = \pi^2 \kappa^{5-2\nu_{\text{II}}} A_s \left| J_{\nu_{\text{II}}}(2\kappa) H_{\nu_{\text{I}}-1}^{(1)}(2\kappa) + J_{\nu_{\text{II}}+1}(2\kappa) H_{\nu_{\text{I}}}^{(1)}(2\kappa) \right|^2, \quad (3.15)$$

$$\mathcal{P}_\zeta^{\text{osc,BPL}}(k) = A_s \left[\left(\kappa^{7/2-\nu_{\text{I}}} \frac{(\nu_{\text{I}} + \nu_{\text{II}})\Gamma(\nu_{\text{I}} - 1)}{\Gamma(\nu_{\text{II}} + 2)} \right)^{-\gamma} + \left(\kappa^{3/2-\nu_{\text{II}}} \right)^{-\gamma} \right]^{-2/\gamma}. \quad (3.16)$$

The rewriting in terms of the two contributions in Eqs. (3.15) and (3.16) is equivalent to (3.13) when imposing $F = 1$, but it is done to separate the smooth BPL contribution from

⁷For notational simplicity, the template uses a different normalization and scaling of the argument than (3.13).

the one including the oscillations. This way, changing F smoothly transitions between an oscillating ($F = 1$) and a non-oscillating $F = 0$ power spectra.

The shape of the BPL template is recovered using (3.7) with $\nu_I = (7 - \alpha)/2$ and $\nu_{II} = (3 + \beta)/2$ when $\alpha \leq 5$. To obtain an exact match with (3.7) the normalization and the momenta must also be rescaled so that $\mathcal{P}_\zeta^{\text{BPL}}(k) = n\mathcal{P}_\zeta^{\text{osc,BPL}}(bk)$, where

$$n \equiv b^\beta (1 + \beta/\alpha)^\gamma, \quad b \equiv \left[\frac{4(\alpha/\beta)^\gamma \Gamma((\beta + 7)/2)^2}{(-\alpha + \beta + 10)^2 \Gamma((5 - \alpha)/2)^2} \right]^{\frac{1}{\alpha + \beta}} \quad (3.17)$$

or, equivalently, as $A_s \rightarrow nA_s$ and $k_* \rightarrow k_*/b$. The benchmark scenario corresponds to

$$\begin{aligned} \log_{10} A_s &= -2.58, & \log_{10}(k_*/\text{s}^{-1}) &= -2.02 \\ \nu_I &= 1.95, & \nu_{II} &= 1.61, & \gamma &= 1.67, & F &= 1. \end{aligned} \quad (3.18)$$

We fix the parameters to match the BPL template in the limit $F = 0$.

3.3 Computation of \mathcal{P}_ζ in single field USR scenarios

The benchmark model we introduced in Sec. 2.4 is based on a single-field model of inflation featuring a phase of USR. We now describe in detail how to compute the spectrum of curvature perturbations using linear perturbation theory.

As a warm-up, let us define the system of equations in terms of dimensionless variables rescaled to the corresponding relevant quantities. This typically improves the numerical stability of a code computing the spectrum of curvature fluctuations. We define

$$x \equiv \phi/M_{\text{P}}, \quad U(x) \equiv V(\phi)/V_0, \quad (3.19)$$

where we introduce the suffix 0 to indicate the quantities evaluated at the initial conditions of the background evolution. We can also define the dimensionless time and Hubble rate using

$$\tau \equiv tV_0^{1/2}/M_{\text{P}}, \quad h \equiv HM_{\text{P}}/V_0^{1/2}. \quad (3.20)$$

We can now change the evolution variable from time to the number of e -folds N , defined as $dN \equiv Hdt = hd\tau$, setting $N = 0$ at τ_0 . In this way, the background equations of motion (2.2) and (2.3) become

$$y' + 3 \left[1 - \frac{y^2}{6} \right] y + \frac{U_{,x}}{h^2} = 0, \quad (3.21a)$$

$$x' - y = 0, \quad (3.21b)$$

$$h' + \frac{(x')^2}{2} h = 0, \quad (3.21c)$$

where prime denotes derivatives with respect to N , while $U_{,x} \equiv dU(x)/dx$. The initial conditions for the inflaton and the Hubble parameters can be found assuming that initially, SR is satisfied, which for a given initial x_0 leads to

$$y_0 = -\frac{3}{U_{0,x}} \left(\sqrt{1 + \frac{2}{3}U_{0,x}^2} - 1 \right), \quad h_0 \equiv \frac{1}{\sqrt{6}} \left(\sqrt{1 + \frac{2}{3}U_{0,x}^2} - 1 \right)^{1/2}. \quad (3.22)$$

Finally, in the code, we keep track of the equation of state during inflation $w_{\text{inf}} \equiv p_\phi/\rho_\phi$, which can be written in our notation as $w = [(x')^2 - 3]/3$. As inflation stops when the equation of state becomes larger than $w > -1/3$, we stop the evolution when $(x')^2 = 2$.

The resulting inflationary background can be described by the evolution of the Hubble rate H . This is dictated by dynamical equations relating H to the SR parameters, which are defined as

$$\epsilon_H \equiv -\frac{\dot{H}}{H^2} = \frac{1}{2M_{\text{P}}^2} \left(\frac{d\phi}{dN} \right)^2 \equiv \frac{y^2}{2}, \quad (3.23)$$

$$\eta_H \equiv -\frac{\ddot{H}}{2H\dot{H}} = \epsilon_H - \frac{1}{2} \frac{d \log \epsilon_H}{dN} = \frac{y^2}{2} - \frac{y'}{y}, \quad (3.24)$$

where we introduced $y = x'$. Notice that our definition of η_H differs from another definition often used in the literature, which is expressed as $\dot{\epsilon}_H/(\epsilon_H H)$. During the USR phase, this definition equals approximately $-2\eta_H$ neglecting ϵ_H corrections.

As long as the SR approximation is valid, i.e. $\epsilon_H \ll 1$ and $\eta_H \ll 1$, the power spectrum of curvature perturbations (see e.g. [269]) is given by

$$\mathcal{P}_\zeta(k) = \frac{H_k^2}{8\pi^2 M_{\text{P}}^2 \epsilon_{H,k}} = \frac{V_0}{M_{\text{P}}^4} \left(\frac{h_k}{2\pi y_k} \right)^2, \quad (3.25)$$

where the suffix k indicates that these quantities are evaluated at Hubble crossing $k = aH$. Consequently, one can also show that the scalar spectral index $n_s - 1 \equiv d \ln \mathcal{P}_\zeta / d \ln k$ and the tensor-to-scalar ratio $r \equiv \mathcal{P}_h / \mathcal{P}_\zeta$ are given by the well-known expressions

$$n_s \approx 1 - 4\epsilon_H + 2\eta_H, \quad (3.26)$$

$$r \approx 16\epsilon_H, \quad (3.27)$$

at leading order in the SR parameters.

The approximations above can not be used in the context of USR scenarios, as the large deceleration of the inflaton velocity causes $\eta_H \sim \mathcal{O}(1)$ ($\eta_H = 3$ in the limit of exponential deceleration). We go beyond the SR approximation by solving the Mukhanov-Sasaki (MS) equation [270, 271]. Introducing momentarily the conformal time η such that $d\eta \equiv dt/a$, we can define the MS variable $v \equiv a\delta\phi$ in terms of the inflaton perturbations in the spatially flat gauge, which satisfies the EoM

$$\frac{\partial^2 v}{\partial \eta^2} + \left(k^2 - \frac{1}{z} \frac{\partial^2 z}{\partial \eta^2} \right) v = 0, \quad (3.28)$$

where $z \equiv a^2(\partial\phi/\partial\eta)/(\partial a/\partial\eta)$. We can relate the curvature perturbation to v at linear order in perturbation theory using $\zeta = v/z = H\delta\phi/(\partial\phi/\partial t) = \delta x/y$. Assuming initial adiabatic vacuum, each mode k is fixed in the asymptotic past at $\eta_{\text{in}} \ll -1/k$ as

$$v(\eta) = e^{-ik(\eta-\eta_{\text{in}})}/\sqrt{2k}, \quad (3.29)$$

which translates into boundary conditions for Eq. (3.28) of the form

$$v_{\text{in}} = \frac{1}{\sqrt{2k}}, \quad \frac{\partial v_{\text{in}}}{\partial \eta} = -i\sqrt{\frac{k}{2}}. \quad (3.30)$$

One can improve the stability of the numerical computation by defining a rescaled variable $\widetilde{\delta\phi} \equiv a_{\text{in}} e^{ik(\eta - \eta_{\text{in}})} \delta\phi \sqrt{2k}$ and the corresponding dimensionless quantity $\widetilde{\delta x} \equiv \widetilde{\delta\phi}/M_{\text{P}}$. The prefactor absorbs the sub-Hubble oscillations, simplifying the time evolution of the sub-Hubble phase. Next, we introduce the dimensionless momentum $\kappa \equiv kM_{\text{P}}/V_0^{1/2}$. Finally, moving to the number of e -folds as the time variable, the MS equation becomes

$$\frac{d^2 \widetilde{\delta x}}{dN^2} + \left(3 - \frac{1}{2}y^2 - \frac{2i\kappa}{e^{N_h}} \right) \frac{d\widetilde{\delta x}}{dN} + \left(\frac{U_{,xx} + 2U_{,xy}}{h^2} + 3y^2 - \frac{1}{2}y^4 - \frac{2i\kappa}{e^{N_h}} \right) \widetilde{\delta x} = 0, \quad (3.31)$$

to be solved with initial conditions $\widetilde{\delta\phi}_{\text{in}} = 1$, and $\widetilde{\delta\phi}'_{\text{in}} = -1$, while the curvature power spectrum is extracted using

$$\mathcal{P}_\zeta(k) = \frac{1}{4\pi^2} \frac{V_0}{M_{\text{P}}^4} \left(\frac{\kappa}{e^{N_{\text{in}}}} \right)^2 \frac{|\widetilde{\delta x}|^2}{y^2}. \quad (3.32)$$

In Fig. 2 we show the background evolution of $x(N)$, $y(N)$ and $h(N)$ obtained in the benchmark scenario (2.6). For convenience, we define N_{end} as the number of e -folds at the end of inflation. In the same plot (top panels), we report the evolution of the Hubble SR parameters and the curvature power spectrum. For simplicity, we identify the momentum with the corresponding time of Hubble crossing $k = a(N)H(N)$. On top, we also indicate the momentum in units of $1/s$. The CMB reference scale crosses the Hubble sphere $N - N_{\text{end}} = -58$ e -folds before the end of inflation, which is indicated with a dashed vertical line. In the top panel, the curvature power spectrum is shown both using the SR approximation (3.25) (blue line), which however fails to reproduce the spectrum around the peak where the USR phase takes place. We show with an orange line the full spectrum computed solving Eq. (3.31). At $k = 0.05/\text{Mpc}$ where the SR expressions (3.25)–(3.27) are valid, we find $\mathcal{P}_\zeta = 2.12 \times 10^{-9}$, $n_s = 0.952$, and $r = 0.00726$. These numbers are compatible with the latest observational bounds [254, 272]

$$\mathcal{P}_\zeta = (2.10 \pm 0.03) \times 10^{-9}, \quad n_s = 0.9649 \pm 0.0042, \quad r < 0.036 \quad (3.33)$$

at the scale $k_{\text{ref}} \equiv 0.05/\text{Mpc}$, reported here at 68% CL for A_s and n_s , and at 95% for r . The low value of n_s is a rather common feature of models featuring an USR phase not sufficiently far from the region of the potential controlling the CMB scales [83, 84, 99, 253], as it is the case if one considers enhancements in the LISA band. This benchmark USR scenario leads to a power spectrum within the LISA band which can be fitted with a BPL template with parameters (3.8).

Let us mention here that it was recently suggested that USR dynamics, in the extremal case of large spectral enhancement with $\mathcal{P}_\zeta \sim \mathcal{O}(10^{-2})$ leading to PBH formation, may violate perturbativity and induce loop corrections that could also affect much longer modes associated with the scales observed through the CMB [149]. While the existence and magnitude of this effect for soft modes is still under debate [128, 150–156, 158–164, 273–282], recent analyses show that for realistic transitions into and out of USR perturbativity is retained (see e.g. for analytical [152, 155, 159] and lattice results [283]). In this work, we restrict to adopting linear perturbation theory to compute the \mathcal{P}_ζ at the LISA scales and leave further refinements including loop corrections to the spectrum of curvature perturbations for future work.

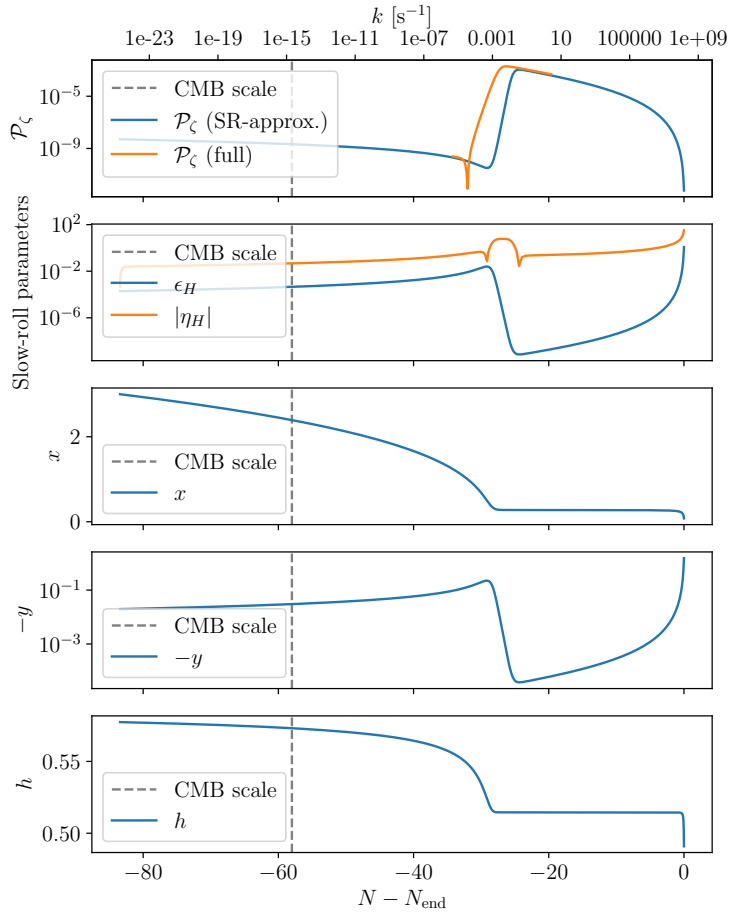


Figure 2. From top to bottom: curvature power spectrum \mathcal{P}_ζ ; Hubble SR parameters ϵ_H and η_H ; dimensionless inflaton field x ; dimensionless inflaton field velocity y ; rescaled Hubble parameter h . In the second panel, η_H is initially small and negative and it transitions to positive values close to $\eta_H \sim 3$ during the USR phase. All quantities are plotted as a function of the number of e -folds to the end of inflation. The vertical dashed lines indicate the epoch when the CMB pivot scale $k_{\text{ref}} = 0.05/\text{Mpc}$ crossed the Hubble sphere.

Non-Gaussianities. As a final note, let us comment on the NGs expected in this benchmark scenario. In this class of USR models, the peak in \mathcal{P}_ζ is generated during a brief phase of USR inflation, which transitions into constant-roll (i.e. constant η_H) inflation afterwards [81, 284, 285]. In these scenarios, NGs are controlled by the details of the transition between USR and the subsequent phase, which is related to the UV tilt of the spectrum [93, 286–288]. We can expect the non-linear curvature perturbation to take the form

$$\zeta = -\frac{2}{\beta} \log \left(1 - \frac{\beta}{2} \zeta_G \right) = \zeta_G + \frac{3}{5} f_{\text{NL}} \zeta_G^2 + \dots, \quad (3.34)$$

with $f_{\text{NL}} = 5\beta/12 \simeq 0.092$ in our benchmark scenario (3.8). Note, however, that this only takes into account the local generation of non-Gaussianity on super-Hubble scales by considering Gaussian inflaton fluctuations, while it has recently been shown using simulations that nonlinear interactions can also generate a large amount of non-Gaussianity intrinsic to the inflaton [283]. Finally, let us mention that such small NG for perturbations of the typical amplitude considered here would lead to negligible contributions to the SIGW spectrum (see more discussion in Sec. 4.5), even beyond standard perturbation theory [68].

4 Computation of the scalar-induced GW background

Primordial scalar perturbations are frozen during their super-Hubble evolution; only when re-entering the Hubble radius after inflation ends do they start evolving in time. Moreover, even if scalar, vector and tensor modes are independent at the first order in perturbation theory, they couple when going to higher orders in fluctuations. For example, scalar modes source tensor modes and thus produce GWs.⁸

In the metric defined in Eq. (3.1), we ignore tensor perturbations generated at first order $h_{ij}^{(1)}$ and consider scalar perturbations that act as a source of second order tensor modes at $h_{ij}^{(2)}$. The exact evolution of $h_{ij}^{(2)}$ can be obtained from the spatial part of the Einstein equations after applying the projection tensor \mathcal{T}_{ij}^{lm} , which selects the transverse-traceless component. In the absence of anisotropic stress, at second order (note that we drop the superscript indicating the order in perturbation theory from now on) one obtains [15, 16, 18, 19]

$$h_{ij}''(\eta, \mathbf{x}) + 2\mathcal{H}h_{ij}'(\eta, \mathbf{x}) - \nabla^2 h_{ij}(\eta, \mathbf{x}) = -4\mathcal{T}_{ij}^{lm}\mathcal{S}_{lm}(\eta, \mathbf{x}), \quad (4.1)$$

where ' is the derivative with respect to conformal time η , $\mathcal{H} = a'/a$ denotes the conformal Hubble parameter, and \mathcal{S}_{ij} is the source term

$$\mathcal{S}_{ij}(\eta, \mathbf{x}) = 4\Phi\partial_i\partial_j\Phi + 2\partial_i\Phi\partial_j\Phi - \frac{4}{3(1+w)}\partial_i\left(\frac{\Phi'}{\mathcal{H}} + \Phi\right)\partial_j\left(\frac{\Phi'}{\mathcal{H}} + \Phi\right). \quad (4.2)$$

In the last equation w is the equation-of-state parameter of the Universe, and the scalar perturbation $\Phi(\eta, \mathbf{x})$ can be related to the gauge-invariant comoving curvature perturbation ζ . Solving Eq. (4.1) in Fourier space, as we review in Sec. 4.1, we obtain the (time-averaged) dimensionless power spectrum $\mathcal{P}_h(\eta_f, k)$ of GWs at a time η_f after the end of their production. The fractional energy density of GWs per logarithmic interval in frequency is given by

$$\Omega_{\text{GW}}(\eta_f, k) \equiv \frac{\rho_{\text{GW}}(\eta_f, k)}{\rho_c(\eta_f)} = \frac{1}{24} \left(\frac{k}{\mathcal{H}(\eta)}\right)^2 \overline{\mathcal{P}_h(\eta_f, k)}, \quad (4.3)$$

with

$$\rho_{\text{GW}}(\eta) = \int d\ln k \rho_{\text{GW}}(\eta, k), \quad (4.4)$$

⁸The production of scalar modes from primordial tensor modes is discussed in [289, 290]. Moreover, very recently, SIGWs sourced by scalar-tensor perturbations have also been analyzed [291, 292].

the bar denoting an oscillation average and ρ_c is the critical energy density. GWs redshift as relativistic species and the current abundance of the GWB can be obtained by accounting for entropy injections in the standard thermal history of the Universe:

$$\Omega_{\text{GW}}(k)h^2 = \Omega_{r,0}h^2 \left(\frac{g_*(\eta_f)}{g_*^0} \right) \left(\frac{g_{*s}^0}{g_{*,s}(\eta_f)} \right)^{4/3} \Omega_{\text{GW}}(\eta_f, k). \quad (4.5)$$

Here g_* ($g_{*,s}$) are the relativistic degrees of freedom in energy (entropy), $\Omega_{r,0}h^2 = 4.2 \cdot 10^{-5}$ is the current radiation density if the neutrino were massless [293]. Assuming standard model degrees of freedom, one finds that [294]

$$c_g(\eta_f) \equiv \left(\frac{g_*(\eta_f)}{g_*^0} \right) \left(\frac{g_{*s}^0}{g_{*,s}(\eta_f)} \right)^{4/3} \simeq 0.39, \quad (4.6)$$

for η_f of relevance for LISA.

4.1 Source of GWs at second order in the scalar perturbations

The solution to Eq. (4.1) can be easily found in Fourier space, where the equation for the GW amplitude h for each polarization state s becomes

$$h_s''(\mathbf{k}, \eta) + 2\mathcal{H}h_s'(\mathbf{k}, \eta) + k^2h_s(\mathbf{k}, \eta) = 4\mathcal{S}_s(\mathbf{k}, \eta) \quad (4.7)$$

and where $\mathcal{S}_s(\mathbf{k}, \eta)$ encloses the Fourier transform of the (projected) source given by

$$\mathcal{S}_s(\mathbf{k}, \eta) = \int \frac{d^3\mathbf{p}}{(2\pi)^3} Q_s(\mathbf{k}, \mathbf{p}) f(|\mathbf{k} - \mathbf{p}|, p, \eta) \zeta(\mathbf{p}) \zeta(\mathbf{k} - \mathbf{p}). \quad (4.8)$$

In the latter equation, we introduced

$$f(|\mathbf{k} - \mathbf{p}|, p, \eta) = \frac{3(1+w)}{(5+3w)^2} \left[2(5+3w)T(|\mathbf{k} - \mathbf{p}|\eta)T(p\eta) + \frac{4}{\mathcal{H}^2}T'(|\mathbf{k} - \mathbf{p}|\eta)T'(p\eta) \right. \\ \left. + \frac{4}{\mathcal{H}}(T(|\mathbf{k} - \mathbf{p}|\eta)T'(p\eta) + T'(|\mathbf{k} - \mathbf{p}|\eta)T(p\eta)) \right] \quad (4.9)$$

and we introduced the curvature perturbation transfer function $T(k\eta)$, and the spherical coordinates (p, θ, ϕ) for the internal momentum \mathbf{p} and aligned the axes $(\hat{x}, \hat{y}, \hat{z})$ with $(e_+(\mathbf{k}), e_\times(\mathbf{k}), \mathbf{k})$ (with e_+, e_\times being the polarisation tensors for the GW) so that

$$Q_s(\mathbf{k}, \mathbf{p}) = e_s^{ij}(\hat{\mathbf{k}})p_i p_j = \frac{p^2}{\sqrt{2}} \sin^2 \theta \times \begin{cases} \cos 2\phi, & s = + \\ \sin 2\phi, & s = \times \end{cases}. \quad (4.10)$$

A solution to the Fourier transform of the inhomogeneous equation of motion for $h_{ij}(\eta, k)$, Eq. (4.1), can be obtained using the Green's function $G_{\mathbf{k}}(\eta, \bar{\eta})$, that solves the homogeneous equation

$$G_{\mathbf{k}}''(\eta, \bar{\eta}) + \left(k^2 - \frac{a''}{a} \right) G_{\mathbf{k}}(\eta, \bar{\eta}) = \delta(\eta - \bar{\eta}), \quad (4.11)$$

with the boundary conditions $\lim_{\eta \rightarrow \bar{\eta}} G_{\mathbf{k}}(\eta, \bar{\eta}) = 0$ and $\lim_{\eta \rightarrow \bar{\eta}} G'_{\mathbf{k}}(\eta, \bar{\eta}) = 1$. The Green's function depends on $k = |\mathbf{k}|$ by isotropy and can be expressed analytically in terms of Bessel functions as

$$k G_{\mathbf{k}}(\eta, \bar{\eta}) = \sqrt{x\bar{x}} [y_{\nu}(x)j_{\nu}(\bar{x}) - j_{\nu}(x)y_{\nu}(\bar{x})], \quad (4.12)$$

where $x = k\eta$, $\bar{x} = k\bar{\eta}$, and $\nu = 3(1-w)/[2(1+3w)]$ and j_{ν} and y_{ν} are respectively the spherical Bessel function of the first and second kind. For example, during RD, $kG_{\mathbf{k}}(\eta, \bar{\eta}) = \sin(x - \bar{x})\Theta(\eta - \bar{\eta})$, where Θ is the Heaviside function.

The amplitude of the tensor modes can then be written as

$$\begin{aligned} h_s(\mathbf{k}, \eta) &= 4 \int_{\eta_i}^{\eta} d\bar{\eta} G_{\mathbf{k}}(\eta, \bar{\eta}) \frac{a(\bar{\eta})}{a(\eta)} \mathcal{S}_s(\mathbf{k}, \bar{\eta}) \\ &= 4 \int_{\eta_i}^{\eta} d\bar{\eta} G_{\mathbf{k}}(\eta, \bar{\eta}) \frac{a(\bar{\eta})}{a(\eta)} \int \frac{d^3\mathbf{p}}{(2\pi)^3} Q_s(\mathbf{k}, \mathbf{p}) f(|\mathbf{k} - \mathbf{p}|, p, \bar{\eta}) \zeta(\mathbf{p}) \zeta(\mathbf{k} - \mathbf{p}), \end{aligned} \quad (4.13)$$

with s indicating the polarisation and η_i the initial emission time. The GW two-point function, needed to obtain the energy density of GWs as a function of the scalar power spectrum, is defined in terms of the GW power spectrum

$$\langle h^r(\eta, \mathbf{k}_1) h^s(\eta, \mathbf{k}_2) \rangle \equiv (2\pi)^3 \delta(\mathbf{k}_1 + \mathbf{k}_2) \delta^{rs} \frac{2\pi^2}{k_1^3} \mathcal{P}_h(k_1). \quad (4.14)$$

After substituting Eq. (4.12) into Eq. (4.13), the final expression for the second-order induced tensor power spectrum reads [295, 296]

$$\begin{aligned} \langle h^{s_1}(\eta, \mathbf{k}_1) h^{s_2}(\eta, \mathbf{k}_2) \rangle &= 16 \int \frac{d^3\mathbf{p}_1}{(2\pi)^3} \frac{d^3\mathbf{p}_2}{(2\pi)^3} Q_{s_1}(\mathbf{k}_1, \mathbf{p}_1) Q_{s_2}(\mathbf{k}_2, \mathbf{p}_2) \\ &\times I(|\mathbf{k}_1 - \mathbf{p}_1|, p_1, \eta_1) I(|\mathbf{k}_2 - \mathbf{p}_2|, p_2, \eta_2) \delta^{(3)}(\mathbf{k}_1 + \mathbf{k}_2) \langle \zeta_{\mathbf{p}_1} \zeta_{\mathbf{k} - \mathbf{p}_1} \zeta_{\mathbf{p}_2} \zeta_{\mathbf{k} - \mathbf{p}_2} \rangle. \end{aligned} \quad (4.15)$$

In the Gaussian case, where only the disconnected part of the trispectrum survives (hence the ‘‘d’’ in the following equation, we discuss in Sec. 4.5 the impact of primordial NG), one obtains

$$\overline{\mathcal{P}_{h,d}(\eta, k)} = 4 \int_0^{\infty} dv \int_{|1-v|}^{1+v} du \left[\frac{4v^2 - (1+v^2 - u^2)^2}{4uv} \right]^2 \overline{I^2(u, v, k, \eta)} \mathcal{P}_{\zeta}(kv) \mathcal{P}_{\zeta}(ku), \quad (4.16)$$

where we introduced the dimensionless variables

$$v \equiv \frac{p}{k}, \quad u \equiv \frac{|\mathbf{k} - \mathbf{p}|}{k}. \quad (4.17)$$

The overline stands for an oscillation average, and the kernel function $I(u, v, \eta)$ is defined in terms of Green's function as

$$I(|\mathbf{k} - \mathbf{p}|, p, \eta) = \int_{\eta_i}^{\eta} d\bar{\eta} G_{\mathbf{k}}(\eta, \bar{\eta}) \frac{a(\bar{\eta})}{a(\eta)} f(|\mathbf{k} - \mathbf{p}|, p, \bar{\eta}). \quad (4.18)$$

Since the integration domain of (4.16) is rectangular, for computational purposes, it is convenient to rotate the coordinates into

$$t \equiv u + v - 1, \quad s \equiv u - v \quad (4.19)$$

and the SIGW spectrum $\overline{\mathcal{P}_h(\eta, k)}$ can be then rewritten as

$$\overline{\mathcal{P}_h(\eta, k)} = 4 \int_0^\infty dt \int_0^1 ds \left[\frac{t(2+t)(1-s^2)}{(1-s+t)(1+s+t)} \right]^2 \overline{I^2(t, s, k, \eta)} \times \mathcal{P}_\zeta \left(k \frac{t+s+1}{2} \right) \mathcal{P}_\zeta \left(k \frac{t-s+1}{2} \right), \quad (4.20)$$

where the integration in s is restricted to positive values due to the integrand being an even function of s . The integration kernel $I(t, s, \eta)$ contains information about the time evolution of the source during emission, as well as the propagation of the emitted GWs after emission, and thus depends on the thermal history when the relevant modes re-entered the Hubble radius. Let us consider different assumptions on the thermal history in the following sections.

The generation of tensor modes at second-order in perturbation theory raises concerns about the potential gauge dependence of results commonly calculated in the Newtonian gauge. Unlike first-order tensor modes, which are gauge invariant, second-order tensor modes are gauge dependent [297]. During the phase when the source is still active, the result is expected to remain gauge-dependent, as one cannot directly identify the tensor mode with the freely propagating GW. However, when the source becomes inactive after the GWs are produced, it effectively decouples from the GWs. This happens for example during the radiation-dominated era of the Universe and in the other cases considered in this draft. Therefore, in the late-time limit well inside the cosmological horizon, tensor mode behaves as linear metric perturbations and the initial gauge dependence no longer affects the final result [298–301], ensuring that the spectra computed in this work are unaffected by this issue.

4.2 Radiation-dominated era

If the emission takes place in a RD universe, the kernel function in the deep sub-horizon regime $k\eta \rightarrow \infty$ takes the form [49, 295, 296]

$$\overline{I_{\text{RD}}^2(t, s, k\eta \rightarrow \infty)} = \frac{1}{2(k\eta)^2} I_A^2(u, v) [I_B^2(u, v) + I_C^2(u, v)] \quad (4.21)$$

where

$$\begin{aligned} I_A(u, v) &= \frac{3(u^2 + v^2 - 3)}{4u^3v^3}, \\ I_B(u, v) &= -4uv + (u^2 + v^2 - 3) \log \left| \frac{3 - (u+v)^2}{3 - (u-v)^2} \right|, \\ I_C(u, v) &= \pi(u^2 + v^2 - 3) \Theta(u + v - \sqrt{3}), \end{aligned} \quad (4.22)$$

u and v have been introduced above and again $\Theta(x)$ is the Heaviside function. Notice that the unphysical divergence obtained in the limit $|\mathbf{k} - \mathbf{p}| + p = \sqrt{3}k$, which is also retained in the spectrum produced by monochromatic scalar perturbations [18]. The factor of $\sqrt{3}$ originates from the (inverse) sound speed in RD appearing in the transfer function, and in the limit $|\mathbf{k} - \mathbf{p}| + p = \sqrt{3}k$ the contributions from some of the source terms add up

constructively and build up logarithmically over time [295]. Assuming RD up to $\eta \rightarrow \infty$ leads to this logarithmic divergence, which is regularized in the integral for \mathcal{P}_h if $\mathcal{P}_\zeta(k)$ is smooth enough (e.g. has a nonzero width), or if the emission time is finite. We do not introduce this regulator here, as it is numerically irrelevant for spectra with finite width [67].

4.3 Transition from an early matter-dominated to the radiation-dominated era

We further consider the alternative thermal history wherein an early matter-dominated (eMD) era may precede the RD era. We follow the prescription of [302], assuming a sudden transition at a conformal time $\eta = \eta_R$, where the subscript R indicates the reheating time [296]. In this scenario, the dominant contribution comes from GWs induced during the RD era by the scalar perturbations that have entered the horizon during an eMD era.

Interestingly, in this case, one observes a resonantly enhanced production of GWs. In particular, during the transition, the time derivative of the Bardeen potential Φ , which is the source of the SIGW signal, goes very quickly from $\Phi' = 0$ (since in an eMD era $\Phi = \text{constant}$) to $\Phi' \neq 0$ (see [234, 299] for more details), leading to an enhanced secondary tensor mode production sourced mainly by the $\mathcal{H}^2\Phi'^2$ term in Eq. (4.2). In a more physical scenario, the transition happens more gradually [303–305].

For the kernel function $I(t, s, k, \eta)$, one finds two dominant contributions at the onset of the late RD era, i.e. at $\eta = \eta_R$, when most of the GWs are expected to be produced [299, 306]. The first contribution to $I(t, s, k, \eta)$ is given by $k_{\text{max}}/k \sim 1$, at $t_0 = \sqrt{3} - 1$ [302]

$$\overline{I_{\text{RD,res}}^2}(t_0, s, k, \eta_R) \simeq Y \frac{9(-5 + s^2 + 2t + t^2)^4 x_R^8}{2^{17} 5^4 (1 - s + t)^2 (1 + s + t)^2} \text{Ci}^2(y), \quad (4.23)$$

where $x_R = k\eta_R$. The variable y is defined as $y \equiv \frac{|t+1-c_s^{-1}|x_R}{2c_s^{-1}} = \frac{|t+1-\sqrt{3}|x_R}{2\sqrt{3}}$, and Y is a fudge factor to absorb the uncertainty in the integration boundary, set here to be 2.3 as in [302]. At $t_0 = \sqrt{3} - 1$, the logarithmic singularity of the function Ci is reached, giving rise to the peak in the spectrum.

The second contribution to $I(t, s, k, \eta)$ comes from the wave-numbers satisfying $k_{\text{max}}/k \gg 1$, hence the integrations are dominated by the large t region $u \sim v \sim t \gg 1$. Therefore, the dependence on s is lost. Setting $s = 0$, the kernel function reads

$$\overline{I_{\text{RD,LV}}^2}(t \gg 1, s, k, \eta_R) \simeq \frac{9t^4 x_R^8}{2^{17} 5^4} \left[4\text{Ci}^2(x_R/2) + (\pi - 2\text{Si}(x_R/2))^2 \right]. \quad (4.24)$$

The integration region is

$$0 \leq s \leq 1 \quad \text{and} \quad 0 \leq t \leq -s + 2\frac{k_{\text{max}}}{k} - 1 \quad \text{for} \quad k \leq k_{\text{max}}, \quad (4.25)$$

and the result obtained from this integration region is then doubled to account for $s \rightarrow -s$. The two contributions are computed separately and added to give

$$\Omega_{\text{GW}}^{\text{eMDRD}} \simeq \Omega_{\text{GW}}^{(\text{LV})} + \Omega_{\text{GW}}^{(\text{res})}. \quad (4.26)$$

4.4 Computation of SIGW with the binned spectrum approach

In this section, we discuss in more detail the procedure sketched in Sec. 3.1 for computing the SIGW in terms of a template-free approach to the curvature power spectrum. We express the power spectrum as a sum over momentum bins, as in Eq. (3.4). The specific profile for the power spectrum \mathcal{P}_ζ is then associated with a vector of coefficients A_i . By plugging Eq. (3.4) into Eqs. (4.3) and (4.20), we recast the SIGW density into the sum

$$\Omega_{\text{GW}}(k) = \sum_{i,j}^{N-1} \Omega_{\text{GW}}^{(i,j)}(k) A_i A_j \quad (4.27)$$

performed over the momentum bins. The kernel for this sum is the matrix

$$\begin{aligned} \Omega_{\text{GW}}^{(i,j)}(k) &= \frac{1}{12} \left(\frac{k}{aH} \right)^2 \int_0^\infty dt \int_0^1 ds \left[\frac{t(2+t)(s^2-1)}{(1-s+t)(1+s+t)} \right]^2 \frac{1}{I^2(t,s,k,\eta)} \\ &\times \Theta(kv(s,t) - p_i) \Theta(p_{i+1} - kv(s,t)) \Theta(ku(s,t) - p_j) \Theta(p_{j+1} - ku(s,t)), \end{aligned} \quad (4.28)$$

where p_i, p_j are the boundaries of the momentum bins entering in Eq. (3.4).

Importantly, we stress that the matrix $\Omega_{\text{GW}}^{(i,j)}$ of Eq. (4.27) is *independent* of the specific scalar spectrum considered, and the information on \mathcal{P}_ζ is stored only in the coefficients A_i appearing quadratically in Eq. (4.27). This implies that the computation of Eq. (4.28) depends only on the kernel function, and its entries can be computed once for all for any given cosmology: for example, we can use one of the kernels discussed in Sec. 4.2 or Sec. 4.3. The nested integrals appearing in Eq. (4.28) should then be performed a single time for each kernel. Once $\Omega_{\text{GW}}^{(i,j)}$ is determined, it can be used to swiftly compute the resulting Ω_{GW} for *any* \mathcal{P}_ζ , by means of the contractions in Eq. (4.27). In fact, with this method, we reduce the problem of computing Ω_{GW} to perform the simple sum of Eq. (4.27).

This approach is useful in scenarios where the underlying shape of the curvature spectrum is not accurately known, for example, due to the presence of peaks or breaks, whose position depends on the underlying physics we wish to probe. In fact, the method allows us to scan over different sets of A_i components, swiftly computing the SIGW frequency profile, which can then be compared with data. Other approaches for reconstructing the properties of the underlying \mathcal{P}_ζ from SIGW data can be found for example in [307–309].

We tabulate the matrix (4.27) assuming a varying number of bins N in the range of relevance for LISA, which is $k \in [1.26 \times 10^{-4}, 6.28]/s$ both for the internal (i, j) indices, as well as external momentum k . This range is chosen to match the one used by the `SGWBinner` code adopted to perform the LISA forecasts. See the discussion in Sec. 5.

4.5 Non-Gaussian imprints on the SIGW spectrum

From the solution of the SIGW, Eq. (4.13), one can relate the tensor power spectrum to the four-point correlation function of the curvature perturbation, see Eq. (4.15). As anticipated above, the latter can be decomposed into disconnected and connected contributions, where the connected part vanishes when primordial fluctuations are drawn from a Gaussian distribution. The disconnected contribution gives rise to Eq. (4.16) that can

be solely expressed in terms of the scalar power spectrum $\mathcal{P}_\zeta(k)$. However, the connected contribution depends on the primordial trispectrum $\langle \zeta_{\mathbf{k}_1} \zeta_{\mathbf{k}_2} \zeta_{\mathbf{k}_3} \zeta_{\mathbf{k}_4} \rangle'_c = T_\zeta(\mathbf{k}_1, \mathbf{k}_2, \mathbf{k}_3, \mathbf{k}_4)$, whose corresponding tensor power spectrum reads [49]⁹

$$\begin{aligned} \overline{\mathcal{P}_{h,c}} &= \frac{1}{4\pi} \int_0^\infty dv_1 \int_{|1-v_1|}^{1+v_1} du_1 \int_0^\infty dv_2 \int_{|1-v_2|}^{1+v_2} du_2 \int_0^{2\pi} d\psi \\ &\times \frac{\cos(2\psi)}{(u_1 v_1 u_2 v_2)^{5/4}} [4v_1^2 - (1 + v_1^2 - u_1^2)^2] [4v_2^2 - (1 + v_2^2 - u_2^2)^2] \\ &\times \overline{I(u_1, v_1, k, \eta) I(u_2, v_2, k, \eta) \mathcal{T}_\zeta(u_1, v_1, u_2, v_2, \psi)}, \end{aligned} \quad (4.29)$$

and we use the variables u_i and v_i defined above. The dimensionless trispectrum function \mathcal{T}_ζ is defined as

$$\mathcal{T}_\zeta(\mathbf{k}_1, \mathbf{k}_2, \mathbf{k}_3, \mathbf{k}_4) = \frac{(k_1 k_2 k_3 k_4)^{9/4}}{(2\pi)^6} T_\zeta(\mathbf{k}_1, \mathbf{k}_2, \mathbf{k}_3, \mathbf{k}_4), \quad (4.30)$$

and is evaluated at $\mathbf{k}_1 = \mathbf{p}_1, \mathbf{k}_2 = \mathbf{k} - \mathbf{p}_1, \mathbf{k}_3 = -\mathbf{p}_2, \mathbf{k}_4 = -\mathbf{k} + \mathbf{p}_2$, with $\psi = \phi_1 - \phi_2$ the difference between the azimuthal angles of \mathbf{p}_1 and \mathbf{p}_2 with respect to \mathbf{k} . The integration kernel for emission during radiation domination is given by

$$\begin{aligned} \overline{I(u_1, v_1, k, \eta) I(u_2, v_2, k, \eta)} &= \frac{1}{2(k\eta)^2} I_A(u_1, v_1) I_A(u_2, v_2) \\ &\times [I_B(u_1, v_1) I_B(u_2, v_2) + I_C(u_1, v_1) I_C(u_2, v_2)], \end{aligned} \quad (4.31)$$

in terms of $I_{A,B,C}$ defined in Eq. (4.22) and with $x = k\eta$. As for the disconnected contribution, it is numerically convenient to change the integration variables from (u_i, v_i) to (t_i, s_i) , with

$$\int_0^\infty dv_i \int_{|1-v_i|}^{1+v_i} du_i(\dots) = \frac{1}{2} \int_0^\infty dt_i \int_{-1}^1 ds_i(\dots), \quad (4.32)$$

where we did not assume symmetry between positive and negative s , to retain full generality in this case.

On general grounds, the properties of the trispectrum and the symmetries of the kernel Eq. (4.31) enable one to split the connected contribution (4.29) into three inequivalent channels [49]. Hence, any trispectrum function of the unordered set $\{\mathbf{k}_1, \mathbf{k}_2, \mathbf{k}_3, \mathbf{k}_4\}$, can be written as

$$T_\zeta[\{\mathbf{k}_1, \mathbf{k}_2, \mathbf{k}_3, \mathbf{k}_4\}] = \tilde{T}_\zeta[(\mathbf{k}_1, \mathbf{k}_2, \mathbf{k}_3, \mathbf{k}_4)] + 23 \text{ perm.}, \quad (4.33)$$

where the individual contributions \tilde{T}_ζ are not in general invariant under permutations of their arguments. Moreover, it can be conveniently written as

$$T_\zeta = (T_s + T_t + T_u) + 7 \text{ perm.}, \text{ with } \begin{cases} T_s = \tilde{T}_\zeta[(\mathbf{k}_1, \mathbf{k}_2; \mathbf{k}_3, \mathbf{k}_4)] \\ T_t = \tilde{T}_\zeta[(\mathbf{k}_1, \mathbf{k}_3; \mathbf{k}_2, \mathbf{k}_4)] \\ T_u = \tilde{T}_\zeta[(\mathbf{k}_1, \mathbf{k}_4; \mathbf{k}_2, \mathbf{k}_3)] \end{cases}, \quad (4.34)$$

⁹In [49], which uses different conventions, their Eq. (2.6) should be divided by 4, as well as subsequent results. This has been corrected in [50] in a study of SIGWs including parity violation.

where the channels \mathfrak{s} , \mathfrak{t} and \mathfrak{u} correspond to the three unordered pairs $\{\{\mathbf{k}_1, \mathbf{k}_2\}, \{\mathbf{k}_3, \mathbf{k}_4\}\}$, $\{\{\mathbf{k}_1, \mathbf{k}_3\}, \{\mathbf{k}_2, \mathbf{k}_4\}\}$ and $\{\{\mathbf{k}_1, \mathbf{k}_4\}, \{\mathbf{k}_2, \mathbf{k}_3\}\}$ together with their “exchanged momenta” $\mathfrak{s} = |\mathbf{k}_1 + \mathbf{k}_2|$, $\mathfrak{t} = |\mathbf{k}_1 + \mathbf{k}_3|$ and $\mathfrak{u} = |\mathbf{k}_1 + \mathbf{k}_4|$ respectively, and where the seven permutations in (4.34) preserves the exchanged momentum of each channel. Furthermore one can show that the trispectrum-induced GW spectrum (4.29) can be written in terms of only three fundamental contributions corresponding to the seeds $T_{\mathfrak{s}}$, $T_{\mathfrak{t}}$ and $T_{\mathfrak{u}}$:

$$\overline{\mathcal{P}}_{h,c} = 8(\overline{\mathcal{P}}_{h,c}^{\mathfrak{s}} + \overline{\mathcal{P}}_{h,c}^{\mathfrak{t}} + \overline{\mathcal{P}}_{h,c}^{\mathfrak{u}}), \quad (4.35)$$

with $\overline{\mathcal{P}}_{h,c}^{\mathfrak{s}}$ simply corresponding to $\overline{\mathcal{P}}_{h,c}$ with T_{ζ} replaced by $T_{\mathfrak{s}}$, etc.

Computing from first principles the trispectrum generated in models relevant for GW astronomy is a difficult task, as these scenarios often involve a strong breaking of scale invariance as well as enhanced fluctuations that can jeopardize perturbative computations, see e.g. [114, 128, 130, 173, 283, 310–313]. In the following, we assume that the trispectrum is of the local τ_{NL} type:

$$T_{\zeta}^{\text{loc}} = \tau_{\text{NL}} [(P_{\zeta}(\mathfrak{s})P_{\zeta}(k_1)P_{\zeta}(k_3) + 3 \text{ perm.}) + (\mathfrak{s} \leftrightarrow \mathfrak{t}) + (\mathfrak{s} \leftrightarrow \mathfrak{u})]. \quad (4.36)$$

We give more details on the computation of the spectrum in the presence of local NGs in App. A.4.

Local NGs, typical of multi-field models, generically arise from the non-linear evolution of cosmological fluctuations on super-Hubble scales (see e.g. [36] for a review). Besides the τ_{NL} type, which emerges microscopically from the exchange of scalar particles through cubic interactions, the local trispectrum also acquires in general a g_{NL} component, coming from contact quartic interactions. However, its momentum dependence is such that it does not contribute to the GW spectrum, and hence we can disregard it for our purpose. We stress that our choice, Eq. (4.36), is a first methodological step motivated by simplicity, in particular because the momentum dependence of the trispectrum is fully characterized by the one of the power spectrum $P_{\zeta}(k)$, which is not the case in general (see [49] for a study of the impact of various trispectrum shapes on the GW spectrum). Let us also highlight a conceptual aspect. Several works in the literature consider a local ansatz in which the real-space curvature perturbation $\zeta(\mathbf{x})$ is expanded in powers of a Gaussian variable $\zeta_{\text{G}}(\mathbf{x})$ as

$$\zeta = \zeta_{\text{G}} + \frac{3}{5}f_{\text{NL}}\zeta_{\text{G}}^2 + \dots, \quad (4.37)$$

and compare the corresponding GW spectrum with the one obtained by keeping only the first term, fully characterized by the power spectrum $P_{\zeta_{\text{G}}}$, see e.g. [41, 42, 45, 46, 48, 52, 53, 277, 309, 314–317]. At leading order, such an expansion does lead to the trispectrum (4.36) with P_{ζ} replaced by $P_{\zeta_{\text{G}}}$, and $\tau_{\text{NL}} = (6f_{\text{NL}}/5)^2$. However, the nonlinear terms in Eq. (4.37) also imply that the curvature power spectrum does not coincide with $P_{\zeta_{\text{G}}}$. Instead, keeping only the quadratic term shown in Eq. (4.37) for definiteness, one finds the power spectrum

$$P_{\zeta}(k) = P_{\zeta_{\text{G}}}(k) + \frac{1}{2} \left(\frac{6}{5}f_{\text{NL}} \right)^2 \int \frac{d^3\mathbf{p}}{(2\pi)^3} P_{\zeta_{\text{G}}}(p) P_{\zeta_{\text{G}}}(|\mathbf{k} - \mathbf{p}|). \quad (4.38)$$

Hence, as described in [49], in this approach, one considers on similar grounds the impact of primordial NG on the SIGW, through the trispectrum, and the difference between a putative P_{ζ_G} to which we have no access, and the power spectrum of ζ which is anyway the only observable quantity. Again, we emphasize that the effects of non-linearities on the SIGW spectrum may not always be fully captured by the local ansatz, Eq. (4.37). As a result, the predicted amplitude of the resulting SGWB could differ significantly [68], potentially being suppressed or enhanced by several orders of magnitude.

In our analysis, whose results are shown in Sec. 6.5, we find it conceptually clearer to take as a benchmark the disconnected prediction from the purely Gaussian theory (4.16) with a given power spectrum $\mathcal{P}_\zeta(k)$, which will take to be of the log-normal form (3.5), and to compare it with the addition of the non-Gaussian, connected, contribution, Eq. (4.29) with trispectrum (4.36). Note that for the latter, the \mathfrak{s} -channel contribution vanishes as the corresponding \mathcal{T}_ζ in Eq. (4.29) does not depend on the azimuthal angle ψ . We are thus left with the two \mathfrak{t} and \mathfrak{u} contributions in Eq. (4.35). Overall, we stress that the parameter to be constrained from observations is τ_{NL} , which measures the non-Gaussian contribution to the SIGW spectrum coming from the trispectrum of curvature perturbations. On scales relevant to LISA, there is *a priori* no constraint on τ_{NL} except that it is positive in known concrete realizations of inflation. Its size is also *a priori* arbitrary, although from a theoretical perspective, perturbative control during inflation typically implies $\tau_{\text{NL}}\mathcal{P}_\zeta < 1$.

5 Mock signal reconstructions with the SGWBinner and SIGWAY codes

This section outlines the analysis method employed in this work. Before presenting the LISA data model adopted in our analysis (Sec. 5.1) and functionalities of the code (Sec. 5.2), let us briefly illustrate the measurement of GWs with LISA.

The observatory will consist of three satellites ($\alpha = 1, 2, 3$) that orbit at the vertices of an approximately equilateral triangle with sides about 2.5 million kilometers long. Each satellite contains two Test Masses (TMs), whose positions are constantly monitored, and two lasers emitting toward the other satellites. By monitoring the fractional Doppler frequency shifts of photons traveling along the arms between satellites, LISA measures the relative displacements of the TMs. The path connecting two satellites is typically dubbed “link” and the single link measurement can be denoted as $\eta_{\alpha\beta}(t)$, where the laser emitted from the satellite β at time $t - L_{\alpha\beta}/c$ is recorded at time t in the satellite α . These measurements are, however, dominated by laser frequency noise, which is expected to be several orders of magnitude greater than the required sensitivity [1]. To suppress this noise contribution, LISA will employ a post-processing technique called Time-Delay Interferometry (TDI) [318–326]. In practice, TDI can be understood as the operation of 3×6 matrix on the six single link measurements $\eta_{\alpha\beta}(t)$ [64, 327] that returns the three TDI channels where the laser frequency noise is strongly suppressed.

As in the previous studies using the SGWBinner code [61, 62, 67, 328, 329], in this work we assume for simplicity i) equal and static arm lengths and ii) equality of noise at each

link. While, in reality, these hypotheses will not be perfectly satisfied¹⁰, it has been shown that the signal reconstruction is almost unaffected by unequal (but static) arm length and unequal noise amplitudes [327, 332]. Under the equal and static arm length assumption, the so-called first-generation TDI variables suffice to achieve laser noise cancellation.¹¹ In the $\{X, Y, Z\}$ basis, they are expressed as

$$X \equiv (1 - D_{13}D_{31})(\eta_{12} + D_{12}\eta_{21}) + (D_{12}D_{21} - 1)(\eta_{13} + D_{13}\eta_{31}), \quad (5.1)$$

with Y and Z being cyclic permutations of X . Here $D_{\alpha\beta}$ is the delay operator acting on any time-dependent function $x(t)$ as $D_{\alpha\beta}x(t) = x(t - L_{\alpha\beta})$ and we take $L_{\alpha\beta} = L = 2.5 \times 10^9$ m. For SGWB signal searches, it is convenient to combine the XYZ variables to obtain the so-called AET basis [334, 335], defined as

$$A \equiv \frac{Z - X}{\sqrt{2}}, \quad E \equiv \frac{X - 2Y + Z}{\sqrt{6}}, \quad T \equiv \frac{X + Y + Z}{\sqrt{3}}, \quad (5.2)$$

which, in the limit of equal arms and equal noises, can be shown to have vanishing cross-correlations and simplify the likelihood computation. Moreover, due to its symmetric structure, the T channel strongly suppresses GW signals at small frequencies compared to instrumental noise. For this reason, the T channel can be treated as a quasi-null channel that is mostly sensitive to instrumental noise.¹²

5.1 Data streams from LISA TDI channels

We represent the three time-domain data streams as $d_i(t)$, where i runs over the channels of the TDI basis. These quantities are real-valued functions defined on the interval $[-\tau/2, \tau/2]$ with τ being the duration of a data segment. The Fourier transforms of these data streams are then given by

$$\tilde{d}_i(f) = \int_{-\tau/2}^{\tau/2} dt e^{2\pi i f t} d_i(t). \quad (5.3)$$

Our central assumption is that all transients including loud deterministic signals and glitches in the noise are subtracted from the time stream through some appropriate methods within the LISA global fit scheme [55–57, 337–339].¹³ That is, as adopted in previous studies [61, 62, 67, 328, 329, 332], the data considered in our analysis only contain the stochastic contributions to the noise, \tilde{n}_i^ν , and the stochastic signal \tilde{s}_i^σ due to the unresolved binary signals and, possibly, the SGWB:

$$\tilde{d}_i(f) = \sum_{\nu} \tilde{n}_i^\nu(f) + \sum_{\sigma} \tilde{s}_i^\sigma(f), \quad (5.4)$$

¹⁰With realistic orbits, LISA will not be perfectly equilateral and arm-lengths vary at the percent level [330] (see also Appendix A of [331]).

¹¹To account for non-static arm lengths and the associated Doppler shifts, the second-generation TDI variables [323, 324, 326, 333] would be required.

¹²The T channel does not remain a null channel in general with unequal and flexing arms and differing noise levels in the different spacecraft, although other quasi-null channels are available [336].

¹³See Ref. [340] for the application of simulation-based inference to the SGWB search performed by LISA in the presence of transient signals, which goes beyond the framework of purely stochastic analysis.

where ν and σ run over different noise and signal components, respectively. In the following, we will assume that all these components are stationary and obey Gaussian statistics with zero mean and variance given by

$$\langle \tilde{n}_i^\nu(f) \tilde{n}_j^{\nu*}(f') \rangle = \frac{1}{2} \delta(f - f') P_{N,ij}^\nu(f), \quad \langle \tilde{s}_i^\sigma(f) \tilde{s}_j^{\sigma*}(f') \rangle = \frac{1}{2} \delta(f - f') P_{S,ij}^\sigma(f), \quad (5.5)$$

where we define the one-side power-spectral density (PSD) (for $i = j$) and cross-spectral density (CSD) (for $i \neq j$) of noise and signal components as $P_{N,ij}^\nu(f)$ and $P_{S,ij}^\sigma(f)$, respectively. Assuming all these components to be uncorrelated with one another, we obtain

$$\begin{aligned} \langle \tilde{d}_i(f) \tilde{d}_j^*(f') \rangle &= \frac{1}{2} \delta(f - f') \left[\sum_\nu P_{N,ij}^\nu(f) + \sum_\sigma P_{S,ij}^\sigma(f) \right] \\ &\equiv \frac{1}{2} \delta(f - f') [P_{N,ij}(f) + P_{S,ij}(f)], \end{aligned} \quad (5.6)$$

where $P_{N,ij}(f)$ and $P_{S,ij}(f)$ are the total noise and signal PSDs and CSDs. By denoting the response functions for isotropic SGWB signals as $\mathcal{R}_{ij}(f)$ (see Refs. [62, 341] for expressions for this quantity), the SGWB (in either strain $S_h^\sigma(f)$ or abundance $\Omega_{\text{GW}}^\sigma(f)$) projected onto the data PSDs and CSDs can be expressed as

$$P_{S,ij}(f) = \mathcal{R}_{ij}(f) \sum_\sigma S_h^\sigma(f) = \mathcal{R}_{ij}(f) \frac{3H_0^2}{4\pi^2 f^3} \sum_\sigma h^2 \Omega_{\text{GW}}^\sigma(f), \quad (5.7)$$

where H_0 is the present Hubble constant and h is the normalized one as $H_0/h \simeq 3.24 \times 10^{-18}$ 1/s. Note again that under the assumptions stated above in this section, one finds that $\mathcal{R}_{ij}(f)$ is diagonal in the AET basis.

It is common practice to quantify the predicted primordial SGWB signal in terms of $h^2 \Omega_{\text{GW}}(f)$; therefore, for later convenience, we define

$$P_{N,ij}^\Omega(f) = \frac{4\pi^2 f^3}{3H_0^2} P_{N,ij}(f). \quad (5.8)$$

In the following, we provide more detailed descriptions of the noise PSDs in the AET basis and of the astrophysical foregrounds which are included in $h^2 \Omega_{\text{GW}}^\sigma(f)$.

5.1.1 Instrumental noise

Our current knowledge of the LISA noise is based on the LISA Pathfinder [342] and laboratory tests. As a first approximation, the stochastic component of the noise in each TDI channel can be grouped into two effective components: ‘‘Optical Metrology System’’ (OMS) noise and TM noise. The former accounts for noise in the readout frequency, such as laser shot noise, while the latter models the noise sources causing accelerations of the TMs, e.g., by environmental disturbances. Introducing the transfer functions for these two noise sources $\mathcal{T}_{ij,\alpha\beta}^\nu(f)$ (for details, see e.g. Refs. [62, 327, 333, 343]), which project those contributions onto the TDI channels, the total noise PSDs and CSDs can be expressed as

$$P_{N,ij}(f) = \sum_\nu P_{N,ij}^\nu(f) = \sum_{\alpha\beta} [\mathcal{T}_{ij,\alpha\beta}^{\text{TM}}(f) S_{\alpha\beta}^{\text{TM}}(f) + \mathcal{T}_{ij,\alpha\beta}^{\text{OMS}}(f) S_{\alpha\beta}^{\text{OMS}}(f)]. \quad (5.9)$$

As customary in the literature, we assume stationary, Gaussian, and uncorrelated noises at each link with identical spectral shapes given by

$$S_{\alpha\beta}^{\text{TM}}(f) = 7.7 \times 10^{-46} \times A_{\alpha\beta}^2 \left(\frac{f_c}{f}\right)^2 \left[1 + \left(\frac{0.4\text{mHz}}{f}\right)^2\right] \left[1 + \left(\frac{f}{8\text{mHz}}\right)^4\right] \times s, \quad (5.10)$$

$$S_{\alpha\beta}^{\text{OMS}}(f) = 1.6 \times 10^{-43} \times P_{\alpha\beta}^2 \left(\frac{f}{f_c}\right)^2 \left[1 + \left(\frac{2\text{mHz}}{f}\right)^4\right] \times s, \quad (5.11)$$

where $A_{\alpha\beta}$ and $P_{\alpha\beta}$ represent the amplitudes of the TM and OMS noises in the different links. Moreover, we have introduced $f_c \equiv (2\pi L/c)^{-1} \simeq 19\text{mHz}$ representing the characteristic frequency of the detector. As mentioned above, we assume the noise amplitudes for all links to be identical, i.e. $A_{\alpha\beta} = A_{\text{noise}}$ and $P_{\alpha\beta} = P_{\text{noise}}$, and, following the ESA mission specifications [54], with fiducial values $A_{\text{noise}} = 3$ and $P_{\text{noise}} = 15$. In this case, the noise spectra reduce to $S_{\alpha\beta}^{\text{TM}}(f) = S^{\text{TM}}(f, A)$ and $S_{\alpha\beta}^{\text{OMS}}(f) = S^{\text{OMS}}(f, P)$. With $\mathcal{T}_{ij,\alpha\beta}^\nu(f)$ in the equal arm length limit, the PSDs in the AET basis read

$$\begin{aligned} P_{N,\text{AA}}(f) &= P_{N,\text{EE}}(f) \\ &= 8 \sin^2 x \left\{ 4 [1 + \cos x + \cos^2 x] S^{\text{TM}}(f, A_{\text{noise}}) + [2 + \cos x] S^{\text{OMS}}(f, P_{\text{noise}}) \right\}, \end{aligned} \quad (5.12)$$

and

$$P_{N,\text{TT}}(f) = 16 \sin^2 x \left\{ 2 [1 - \cos x]^2 S^{\text{TM}}(f, A_{\text{noise}}) + [1 - \cos x] S^{\text{OMS}}(f, P_{\text{noise}}) \right\}, \quad (5.13)$$

where we have defined $x \equiv f/f_c$. Here the CSDs vanish, i.e. $P_{N,ij}(f) = 0$ ($i \neq j$), so that the noise covariance matrix is diagonal.

5.1.2 Astrophysical foregrounds

Numerous weak and unresolvable signals from astrophysical sources will superimpose incoherently generating astrophysical SGWB [4, 344–350]. There are at least two guaranteed components in the LISA band. Below a few millihertz, the dominant contribution will come from Compact Galactic Binaries (CGBs) mostly composed of Double White Dwarfs (DWDs) [351, 352]. At higher frequencies, another contribution is expected from all the extragalactic compact objects including Stellar Origin Binary Black Holes (SOBBHs) and binary neutron stars (BNS) [353]. In the remainder of this section, we provide the templates for these foreground components implemented in the `SGWBinner` code that was recently used in Refs. [67, 328, 329, 332].

Galactic foreground. This component represents the contribution from the unresolved sub-threshold mergers of CGBs that remain after the removal of loud signals from the population of CGBs in the galactic disk [354]. Due to the angular dependence of the response functions and LISA yearly orbit, this component exhibits an annual modulation. While, in principle, this characteristic can help distinguish the galactic component from other stationary contributions, e.g., by accounting for variations in each segment [331,

355, 356], we average over anisotropies, which leads to suboptimal (but conservative¹⁴) foreground extraction. Similarly, because this foreground is formed by the superposition of many unresolvable sources, it is expected to have Gaussian statistics. Recently, Refs. [59, 361, 362] have called into question whether the populations entering the foreground are sufficient for the central limit theorem to apply at all frequencies, and imply a Gaussian description of the foreground may be biased. The non-stationarity of the foreground also in principle induces some non-Gaussianity when time-averaging.

Nevertheless, we use the empirical model from Ref. [363], which describes the sky-averaged and Gaussian contribution by

$$h^2\Omega_{\text{GW}}^{\text{Gal}}(f) = \frac{1}{2} \left(\frac{f}{1 \text{ Hz}} \right)^{2/3} e^{-(f/f_1)^\alpha} \left[1 + \tanh \frac{f_{\text{knee}} - f}{f_2} \right] h^2\Omega_{\text{Gal}}, \quad (5.14)$$

where the value of f_1 and f_{knee} depends on the total observation time T_{obs} as

$$\begin{aligned} \log_{10}(f_1/\text{Hz}) &= a_1 \log_{10}(T_{\text{obs}}/\text{year}) + b_1, \\ \log_{10}(f_{\text{knee}}/\text{Hz}) &= a_k \log_{10}(T_{\text{obs}}/\text{year}) + b_k. \end{aligned} \quad (5.15)$$

The exponential factor $e^{-(f/f_1)^\alpha}$ accounts for the loss of stochasticity at higher frequency [363], while the last tanh term models the expected complete subtraction of CGBs signal at frequencies $f > f_{\text{knee}}$. In order to keep the notation compact, we define $\log_{10}(h^2\Omega_{\text{Gal}}) \equiv \alpha_{\text{Gal}}$. From Ref. [363], we set the fiducial values $a_1 = -0.15$, $b_1 = -2.72$, $a_k = -0.37$, $b_k = -2.49$, $\alpha = 1.56$, $f_2 = 6.7 \times 10^{-4} \text{ Hz}$ and $\alpha_{\text{Gal}} = -7.84$.

Extragalactic foreground. The extragalactic foreground, arising from the incoherent superposition of all extragalactic compact object mergers, includes potential contributions from SOBBHs, BNSs, EMRIs, and DWDs in their inspiral phase. In this work, we focus on only the SOBBH+BNS contribution, leaving any potential EMRI and DWD contribution to future work. Recent studies suggest that extreme mass-ratio inspirals can largely contribute to the foreground but only in somewhat extreme population synthesis scenarios [347]. Extragalactic DWDs may also be more abundant than previously estimated, with a relevant impact on the extragalactic foreground [349, 364] which ongoing analyses are verifying [365]. In the lack of a firmer understanding, we assume these contributions to be below the foregrounds of galactic binaries and extragalactic SOBBHs and BNSs.

We now focus on what we will assume to be the dominant contribution, the SOBBH and BNS foreground. The vast majority of these signals cannot be individually resolved by LISA [366–368] and, for the most part individual detections are possible for the few multi-band sources [369] (see [370], for a more accurate study of such sources). The best estimates for the populations of these objects are based on observations from ground-based detectors [371, 372]. Due to the relatively uniform distribution of the sources and the limited angular resolution of LISA, this component can be well modeled as an isotropic

¹⁴Keeping track of anisotropic nature of the signal, requires the analysis to be time-frequency. To consistently work this out, one would also need to keep track of the non-stationary nature of the noise (see e.g. [59, 357–360]) and the presence of gaps in the data.

SGWB signal with the power-law shape

$$h^2\Omega_{\text{GW}}^{\text{Ext}}(f) = h^2\Omega_{\text{Ext}} \left(\frac{f}{1\text{mHz}} \right)^{2/3}, \quad (5.16)$$

where $h^2\Omega_{\text{Ext}}$ is the amplitude at 1 mHz. Recent observations by LIGO-Virgo-KAGRA collaboration estimate the magnitude of SGWB signal from SOBBHs and BNS as [371]

$$\Omega_{\text{Ext}} = 7.2_{-2.3}^{+3.3} \times 10^{-10} \text{ at } f = 25 \text{ Hz}. \quad (5.17)$$

In order to keep the notation compact, we define $\log_{10}(h^2\Omega_{\text{Ext}}) \equiv \alpha_{\text{Ext}}$. Extrapolating this amplitude to the LISA band [348], yields the fiducial value $\alpha_{\text{Ext}} = -12.38$.

5.2 Analysis of the simulated data

In this section, we summarise the data analysis scheme implemented in the `SGWBinner` code (see Refs. [61, 62] for more details). Let us start with the generation of simulated data. Given the effective observation time T_{obs} and the number of segments N_d (which define the duration of each segment $\tau = T_{\text{obs}}/N_d$), the code generates the data $\tilde{d}_i^s(f_k)$ ($s = 1, \dots, N_d$) segment-by-segment in the frequency-domain. For each frequency bin f_k (spanning $[3 \times 10^{-5}, 0.5]$ Hz with spacing $\Delta f = 1/\tau$), N_d Gaussian realizations of the signal, noise, and foregrounds are generated with zero mean and variances defined by their respective PSDs. These data are then averaged over segments to define $\bar{D}_{ij}^k \equiv \sum_{s=1}^{N_d} d_i^s(f_k) d_j^{s*}(f_k) / N_d$, which gives an estimate of the total power at all frequencies. The next step consists of coarse-graining the data using inverse variance weighting. This results in a coarser set of frequency bins f_{ij}^k and a data set D_{ij}^k with weights n_{ij}^k , retaining similar statistical properties of the original dataset. Similarly to Refs. [62, 67, 328, 329, 332], we set $\tau = 11.4$ days ($\Delta f = 10^{-6}$ Hz), $N_d = 126$, and $T_{\text{obs}} = 4$ years in our analysis.

The likelihood employed in the code reads [62]

$$\ln \mathcal{L}(D|\boldsymbol{\theta}) = \frac{1}{3} \ln \mathcal{L}_{\text{G}}(D|\boldsymbol{\theta}) + \frac{2}{3} \ln \mathcal{L}_{\text{LN}}(D|\boldsymbol{\theta}), \quad (5.18)$$

with

$$\ln \mathcal{L}_{\text{G}}(D|\boldsymbol{\theta}) = -\frac{N_d}{2} \sum_{i \in \{\text{AET}\}} \sum_k n_{ii}^k \left[\frac{\mathcal{D}_{ii}^{th}(f_{ii}^k, \boldsymbol{\theta}) - \mathcal{D}_{ii}^k}{\mathcal{D}_{ii}^{th}(f_{ii}^k, \boldsymbol{\theta})} \right]^2, \quad (5.19)$$

$$\ln \mathcal{L}_{\text{LN}}(D|\boldsymbol{\theta}) = -\frac{N_d}{2} \sum_{i \in \{\text{AET}\}} \sum_k n_{ii}^k \ln^2 \left[\frac{\mathcal{D}_{ii}^{th}(f_{ii}^k, \boldsymbol{\theta})}{\mathcal{D}_{ii}^k} \right], \quad (5.20)$$

where the index k runs over the coarse-grained data points and $\mathcal{D}_{ii}^{th}(f, \boldsymbol{\theta})$ denotes the theoretical predictions for the data, depending on some parameters $\boldsymbol{\theta}$. The model can be further expressed as $\mathcal{D}_{ii}^{th}(f, \boldsymbol{\theta}) \equiv \mathcal{R}_{ii} h^2\Omega_{\text{GW}}(f, \boldsymbol{\theta}_{\text{cosmo}}, \boldsymbol{\theta}_{\text{fg}}) + P_{N,ii}^{\Omega}(f, \boldsymbol{\theta}_{\text{n}})$, with $\boldsymbol{\theta}_{\text{cosmo}}, \boldsymbol{\theta}_{\text{fg}}$ and $\boldsymbol{\theta}_{\text{n}}$ denoting the signal, foreground, and noise parameters, respectively. Notice that the diagonality of the AET basis has been exploited, and no cross terms appear in the likelihood. Given some priors $\pi(\boldsymbol{\theta})$ for the parameters, the posterior distribution reads

$$p(\boldsymbol{\theta}|D) \equiv \frac{\pi(\boldsymbol{\theta})\mathcal{L}(D|\boldsymbol{\theta})}{Z(D)}, \quad (5.21)$$

where $Z(D)$ is the model evidence defined as

$$Z(D) \equiv \int d\boldsymbol{\theta} \pi(\boldsymbol{\theta}) \mathcal{L}(D|\boldsymbol{\theta}) . \quad (5.22)$$

To compare the validity of two different models $M_i(\boldsymbol{\theta}_i)$, each characterized by a set of parameters $\boldsymbol{\theta}_i$, we can use the evidence Z_i as a measure of the quality of the models given the data. The *Bayes factor* for two models i, j is defined as $B_{ij} \equiv Z_i/Z_j$. This Bayes factor can then be compared to the Jeffreys' scale [373] to determine which model is favored by the data.

As key functionalities, the `SGWBinner` code offers *i)* model-agnostic signal reconstruction and *ii)* template-based signal reconstruction. The former fits the signal in each frequency bin using a power-law template, i.e. the signal parameters are

$$\boldsymbol{\theta}_{\text{cosmo}} = \{\alpha_1, n_{T,1}, \dots, \alpha_n, n_{T,n}\} , \quad (5.23)$$

with n denoting the number of bins. The number and width of the bins are dynamically adjusted as described in Refs. [61, 62]. In practice, this method enables a preliminary identification of the spectral shape of the signal, which can guide the choice of the template for the template-based analysis. For the latter, the vector of parameters of the cosmological component $\boldsymbol{\theta}_{\text{cosmo}}$ corresponds to the template parameters.

In this work, we assume the fiducial noise and foreground parameters to be

$$\boldsymbol{\theta}_{\text{n}} = \{A_{\text{noise}}, P_{\text{noise}}\}, \quad \boldsymbol{\theta}_{\text{fg}} = \{\alpha_{\text{Gal}}, \alpha_{\text{Ext}}\}, \quad (5.24)$$

while we assume that the other foreground parameters are known¹⁵, and $\boldsymbol{\theta}_{\text{cosmo}}$ is model dependent. Moreover, when fitting the simulated data, we use the same noise model applied to generate the data.¹⁶ Both for the noise and foreground amplitudes, we assume Gaussian priors centered on their fiducial values. For the former, we set the standard deviation to be 20% of the fiducial mean value. For α_{Gal} and α_{Ext} , we set the standard deviation to be 0.21 and 0.17, respectively. To sample the parameter space the code relies on the `Cobaya` [374] inference framework. To facilitate template-based analysis specifically for SIGW signals, we develop the dedicated `SIGWAY` code. As detailed in App. A, the `SIGWAY` code implements the parameterization of curvature perturbations discussed in Sec. 3 and performs the numerical computation of SIGW signals.

Finally, the code also supports Fisher analysis. In practice, the Fisher Information Matrix (FIM) can be computed by the continuous integral over the frequency range, expressed as

$$F_{ab} \equiv T_{\text{obs}} \sum_{i \in \{\text{AET}\}} \int_{f_{\text{min}}}^{f_{\text{max}}} df \left. \frac{\partial \ln \mathcal{D}_{ii}^{th}}{\partial \theta^a} \frac{\partial \ln \mathcal{D}_{ii}^{th}}{\partial \theta^b} \right|_{\boldsymbol{\theta}=\boldsymbol{\theta}_{\text{fid}}} , \quad (5.25)$$

where f_{min} and f_{max} represent the detector's minimal and maximum measured frequencies, assumed to be $f_{\text{min}} = 3 \times 10^{-5}$ Hz and $f_{\text{max}} = 0.5$ Hz [54]. If non-trivial (log-)priors

¹⁵The effect of loosening this assumption on the signal reconstruction has been discussed in Ref. [332].

¹⁶We note that any differences between the instrumental noise and the model could introduce bias. This issue will have to be closely monitored in future upgrades of the code.

are included in the analysis, the code consistently adds their derivatives to Eq. (5.25) to obtain the full FIM. The relative uncertainty on the reconstruction parameters can then be estimated from the covariance $\text{cov}_{ab} = F_{ab}^{-1}$. Given its computational efficiency, we also employed the FIM approach to assess the prospect of signal reconstruction with some level of accuracy. Note that in the case of SIGW signals, the FIM can be efficiently computed using the automatic differentiation feature of the JAX library [375] by applying the θ derivative in Eq. (5.25) directly to \mathcal{P}_ζ , before it is integrated to yield \mathcal{P}_h . We stress that the FIM formalism only works under the assumption that the likelihood is well approximated by a Gaussian distribution in the model parameters around the best fit (and that, when dealing with real data, the true values of the parameters lie within the region where the FIM is evaluated).

Finally, to complement the visualization of relative uncertainties in the parameter space, we will plot the signal-to-noise ratio (SNR) defined as

$$\text{SNR} \equiv \sqrt{T_{\text{obs}} \sum_{i \in \{\text{AET}\}} \int_{f_{\text{min}}}^{f_{\text{max}}} \left(\frac{P_{S,ii}^\sigma}{P_{N,ii}} \right)^2 df}, \quad (5.26)$$

which scales linearly with the signal amplitude.

6 Results

In this section, we summarise our main results presenting different analyses based on the SIGWAY code outlined in Sec. 5.2 (see App. A for more details). We adopt the three approaches discussed in Sec. 3, namely *i*) binned spectrum agnostic approach; *ii*) template-based approach; *iii*) first principle USR model of inflation – all limited to the leading order SIGW and assuming an RD universe. We then consider specific examples including non-standard early universe evolution and non-Gaussianities.

We report results for both Ω_{GW} and \mathcal{P}_ζ . In the former case, we include the noise curves as well as the foregrounds as discussed in Sec. 5. Since the SIGW backgrounds we consider are emitted at very high redshift, when scales currently associated with mHz re-enter the Hubble sphere, they contribute to the energy budget in the early Universe and can affect cosmological observables as any other relativistic free-streaming component beyond the standard model. In particular, the SIGW contributes to the effective number of neutrino species as $N_{\text{eff}} \equiv 3.044 + \Delta N_{\text{eff}}^{\text{GW}}$, with $\Delta N_{\text{eff}}^{\text{GW}} = \rho_{\text{GW}}/\rho_{\nu,1}$ and $\rho_{\nu,1}$ is the energy density of a single neutrino species. Specifically, the total (integrated) GW abundance is $\Omega_{\text{GW}} h^2 \simeq 1.6 \cdot 10^{-6} (\Delta N_{\text{eff}}^{\text{GW}}/0.28)$ [10]. Measurements of the CMB [293] and Baryon Acoustic Oscillations (BAO) constrain $\Delta N_{\text{eff}} \leq 0.28$ at 95% C.L. We report this bound for reference as shaded gray regions in the $\Omega_{\text{GW}} h^2$ plots.

Strong primordial density perturbations can lead to the copious formation of PBHs with masses of the order of the horizon mass $M_H = 1.3 \times 10^{-15} M_\odot [(k/\kappa_{\text{rm}})/\text{s}^{-1}]^{-2}$, where we kept track of the additional prefactor $\kappa_{\text{rm}} \equiv k r_m \sim \mathcal{O}(3)$ that relates the perturbation scale to the characteristic perturbation size r_m at Hubble crossing [376–379]. Thus, the overproduction of dark matter in the form of PBHs in the asteroid mass range implies

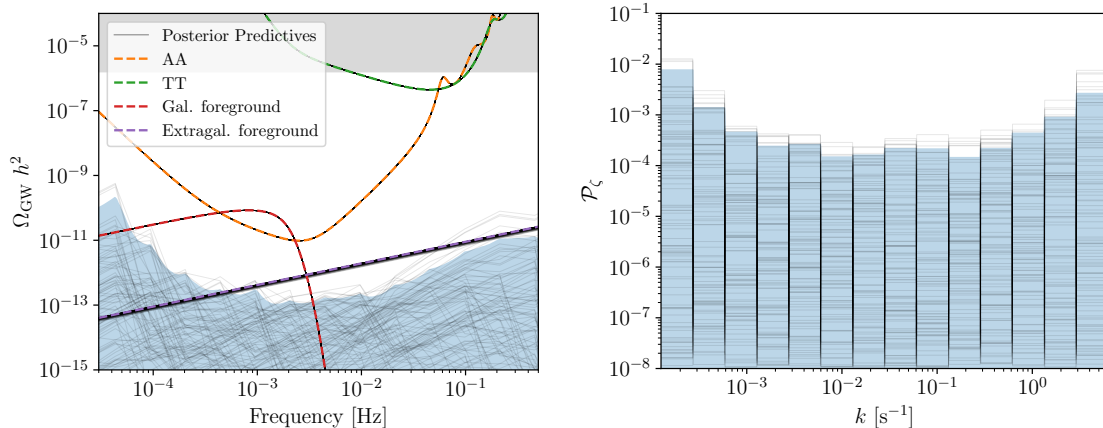


Figure 3. Posterior predictive distribution for both $\Omega_{\text{GW}} h^2$ (left panel) and \mathcal{P}_ζ (right panel). We represent the binned reconstruction of Sec. 6.1 in the case without an injected signal. The posterior saturates the lower bound of the prior for the amplitudes A_i , due to the absence of a resolvable signal. We therefore can only set upper bounds on both $\Omega_{\text{GW}} h^2$ and \mathcal{P}_ζ . The light blue line shows the 95% credible intervals, while the pale black lines individual realisations of a signal sampled from the parameters’ posterior distribution. The upper bound from ΔN_{eff} is shown with a gray shading.

a bound $\mathcal{P}_\zeta \leq \mathcal{O}(10^{-2})$ [257, 380, 381] on the scalar curvature perturbations and thus also on the strength of the SIGW in the mHz frequency band. The abundance and the mass distribution of PBHs depend on the shape of the curvature power spectrum, non-Gaussianities, and on the equation of state of the universe during their formation [28], so does the implied upper bound on SIGWs.

6.1 Binned spectrum method

In Fig. 3 we report the constraints obtained with the binned method (see Sec. 3.1 and 4.4) when injecting no SIGW signal. This analysis forecasts the model-independent upper bounds on both the SIGW energy density spectrum (left panel) and the primordial curvature power spectrum (right panel) in case of no SGWB detection at LISA: this only relies on observational data, without assuming a specific signal model. For this analysis, we assume that the spectrum is divided into $N = 15$ bins. The free parameters in this model are

$$\theta_{\text{cosmo}} = \{A_1, \dots, A_{15}\}. \quad (6.1)$$

In the left panel of Fig. 3 we indicate the posterior predictive distribution for Ω_{GW} with the shaded light blue region, denoting the 95% credible interval (CI). The upper bound effectively reflects the LISA sensitivity, which falls around two orders of magnitude below the noise components in the AA channel because of the long observation time $T_{\text{obs}} = 4\text{yr}$ (see Sec. 5.2). In the right panel, we then show how the LISA sensitivity translates into the \mathcal{P}_ζ parameter space. The figure displays the upper bounds on \mathcal{P}_ζ across the range of momenta k considered, which is $k \in [1.26 \times 10^{-4}, 6.28]/\text{s}$. The posterior saturates at the lower edge of the prior on the amplitude parameters $A_i > 10^{-8}$ reflecting the absence of detectable power beyond the noise level. The posterior predictive bands illustrate that the

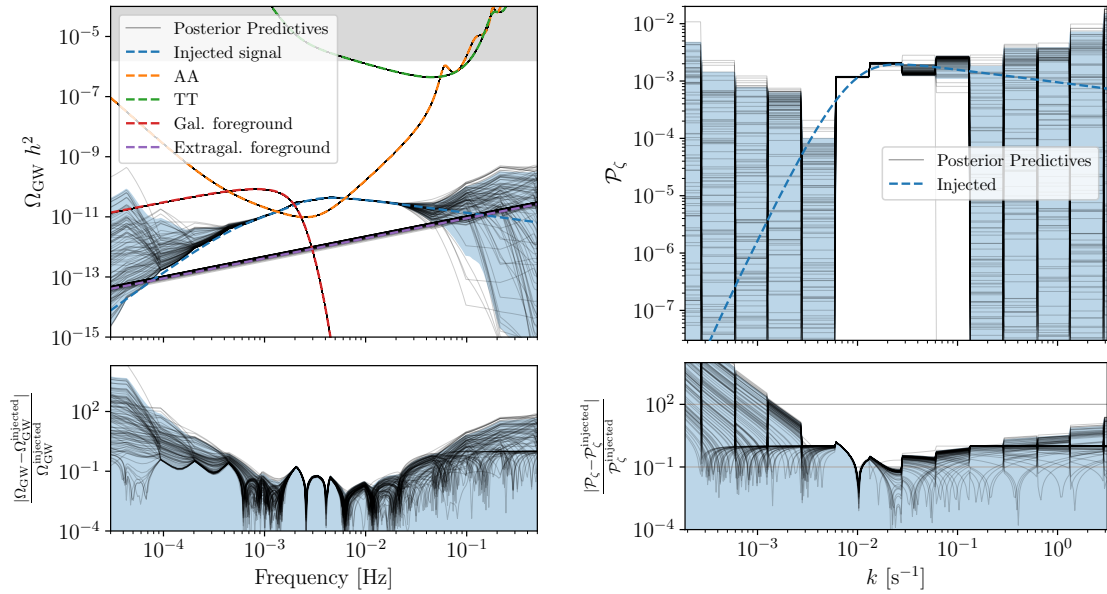


Figure 4. Same as Fig. 3, but simulating the observation of a signal obtained in the benchmark USR model scenario. The quantity \mathcal{P}_ζ is reconstructed with the model-independent binning method with 15 bins. The blue band in the upper panels shows the 90% (symmetric) credible interval, while the blue band in the bottom shows the 95% upper bound on the residuals.

method can constrain \mathcal{P}_ζ across several orders of magnitude in k . In the most sensitive range, this bound reaches $\mathcal{P}_\zeta \lesssim 2 \times 10^{-4}$.

This sensitivity is sufficient for probing a wide range of viable scenarios for asteroid mass PBHs. In particular, a non-detection of a SIGW by LISA would close the asteroid mass window for PBH dark matter formed from the collapse of moderately non-Gaussian curvature fluctuations, including models of PBHs from first-order phase transitions [382–384]. However, as with μ -distortion bounds on heavy PBHs [385–388], extremely strong non-Gaussianities could enhance PBH production and potentially allow evading these constraints. Such extreme scenarios and their theoretical consistency should be studied case by case.

In Fig. 4 we report the constraints obtained with the binned method when injecting the benchmark SIGW signal derived from the single field USR model of Sec 2.4. The curvature power spectrum has a BPL shape (see Eq. (3.7)), with a peak at around $\mathcal{P}_\zeta \sim 2 \cdot 10^{-3}$. Again, we use a template with $N = 15$ bins. In the left panel of Fig. 4, we show the injected SIGW signal (blue dashed line), along with the posterior predictive distribution (light blue band). Although the low number of bins reduces the frequency resolution of our model compared to the one achieved by LISA, the SIGW spectrum is well reconstructed, reaching a precision of the order of a few percent around the peak. At the edges of the observable range of frequencies, the blue bands widen up indicating a poor constraining power on the tail regions. The right panel of Fig. 4 indicates the SIGW bounds translate into four bins being well constrained in the range $k \sim [10^{-2}, 10^{-1}]/\text{s}$ with around $\mathcal{O}(10)\%$

precision, while the other ones being subject to an upper bound of similar amplitude as in Fig. 3.

One could in principle enhance the frequency resolution by using a template with a larger number of bins, at the cost of drastically increasing the computational cost of the Bayesian MCMC inference. In App. B we discuss these issues in more detail.

6.2 Template based method

In this section, we present a forecast on reconstructing the SIGW signal using a template-based method, addressing different scenarios discussed in Sec. 3.2.

6.2.1 Smooth spectra

Lognormal scalar spectrum. The first signal injection we consider is a log-normal shape of \mathcal{P}_ζ as defined in Eq. (3.5) with the benchmark values defined in Eq. 3.6, which we report here $\log_{10} A_s = -2.5$, $\log_{10} \Delta = \log_{10}(0.5)$, $\log_{10} (k_*/s^{-1}) = -2$. This produces a loud signal with the typical double peak being fully within the LISA band. This choice gives us a concrete measure of the precision that is achievable in measuring the SIGW background in this scenario for a reasonably loud signal. The free parameters for this approach are

$$\theta_{\text{cosmo}} = \{\log_{10} A_s, \log_{10} \Delta, \log_{10} (k_*/s^{-1})\}. \quad (6.2)$$

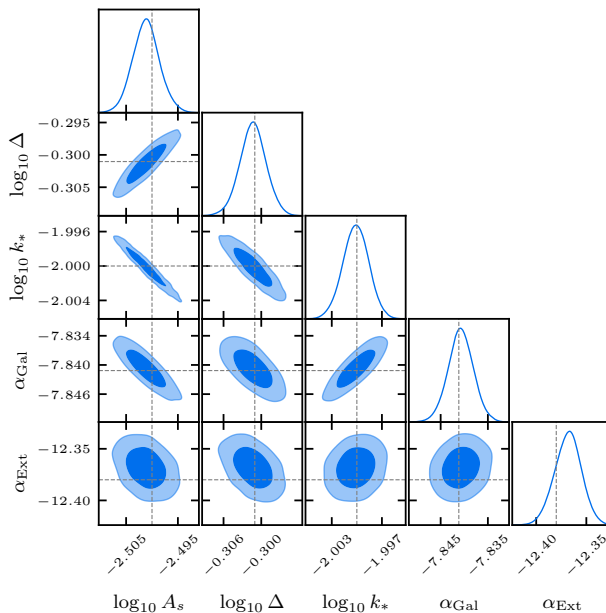


Figure 5. Corner plot with the posterior distribution for an injected LN spectrum \mathcal{P}_ζ , as defined in Eqs. (3.5) and (3.6). k_* is expressed in 1/s units.

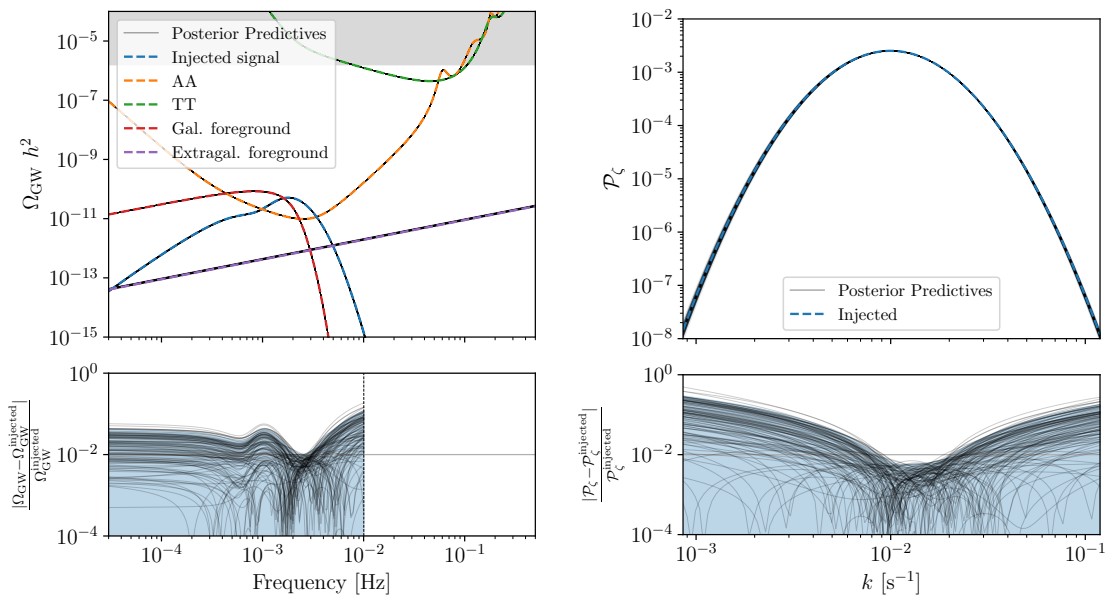


Figure 6. Same as Fig. 3, for an injected log-normal spectrum, as defined in Eqs. (3.5) and (3.6). In the left panel, we arbitrarily cut the posterior predictive where the signal falls below $\Omega_{\text{GW}} \lesssim 10^{-15}$.

Fig. 5 shows the posterior distribution for each parameter of the LN template, alongside the ones describing the galactic/extragalactic foregrounds. We omit in these plots the posterior distributions for the noise parameters, as they are weakly correlated with the others in all cases. The injected values are indicated with a dashed gray line. As we can see, due to the relatively high SNR of the injected signal, the parameters of this template are very accurately reconstructed, with \mathcal{P}_ζ being reconstructed with a relative error of a few percent at its peak. The correlation between A_s and Δ originates from the definition of \mathcal{P}_ζ . As customary in the literature [255], the amplitude at the peak is A_s/Δ , while A_s is the integrated power spectrum $\int_{-\infty}^{\infty} \mathcal{P}_\zeta d \log k = A_s$. Therefore, A_s enters the power spectrum only through the ratio A_s/Δ , thus the positive correlation between the two parameters. Defining A_s to be the peak amplitude would avoid this degeneracy. The correlation of A_s , k_* , and α_{Gal} is instead specific of our choice of fiducial parameters. As can be seen from the posterior predictive distribution in the left panel in Fig. 6, the injected signal is close enough to the galactic foreground that a slight increase in A_s with a decrease in k_* can be compensated by a small decrease in the background amplitude α_{Gal} . We expect that these correlations fade away with a larger injected k_* , when the signal and the galactic background are more distinct.

Fig. 6 shows the posterior predictive distribution for the SIGW (left panel) and curvature power spectrum (right panel). We see that the signal reconstruction achieves better than percent uncertainties on Ω_{GW} and \mathcal{P}_ζ around the peak. The uncertainty on the low-frequency tail of Ω_{GW} saturates at around a few percent, due to the universal behavior of the causality tail [389] sufficiently deep in the IR. See e.g. Appendix B of [67] for a dis-

clusion of logarithmic corrections to the IR tail of the SIGW spectrum. The uncertainty on the tails of \mathcal{P}_ζ remains low even at very small values, because of the rigid assumption about the LN template.

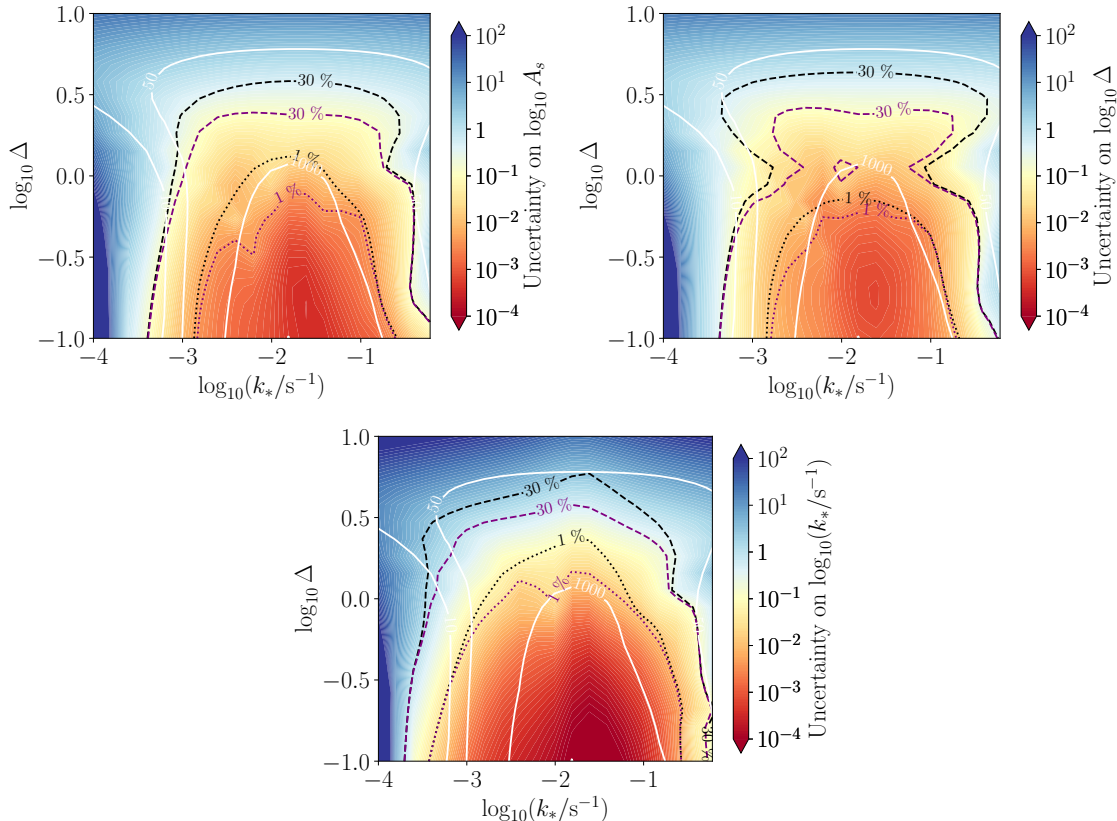


Figure 7. From left to right: Relative uncertainties of each of the parameters of the LN template, computed with an FIM forecast injecting an LN \mathcal{P}_ζ with fixed amplitude $\log_{10} A_s = -2.5$ and varying k_* and Δ . Black (purple) contours show uncertainties without (with) astrophysical foregrounds. The white line indicates SNR values.

In Fig. 7, we scan the parameter space in k_* and Δ estimating the relative uncertainties on all LN parameters using the FIM method. We fix the amplitude of \mathcal{P}_ζ to $\log_{10} A_s = -2.5$. The SIGW amplitude scales like $\Omega_{\text{GW}} \sim A_s^2$, and in the high SNR limit we expect the uncertainties on the parameter to scale inversely $\sim 1/A_s^2$. The results highlight the great sensitivity that is achievable on a SIGW background if the peak lies around the peak sensitivity of LISA, $k_* \sim 10^{-3} - 10^{-1} \text{ s}^{-1}$. In that range, the width Δ for an LN scalar spectrum can be measured with an accuracy of order 10% or better if $\Delta \lesssim \mathcal{O}(1)$. Notice from Fig. 7 that the purple contours, marking the sensitivity on the primordial SIGW background accounting for astrophysical foregrounds, degrade when k_* coincides with the expected peak of the white-dwarfs (WD) galactic foreground, and the two GW backgrounds are less distinguishable [390].

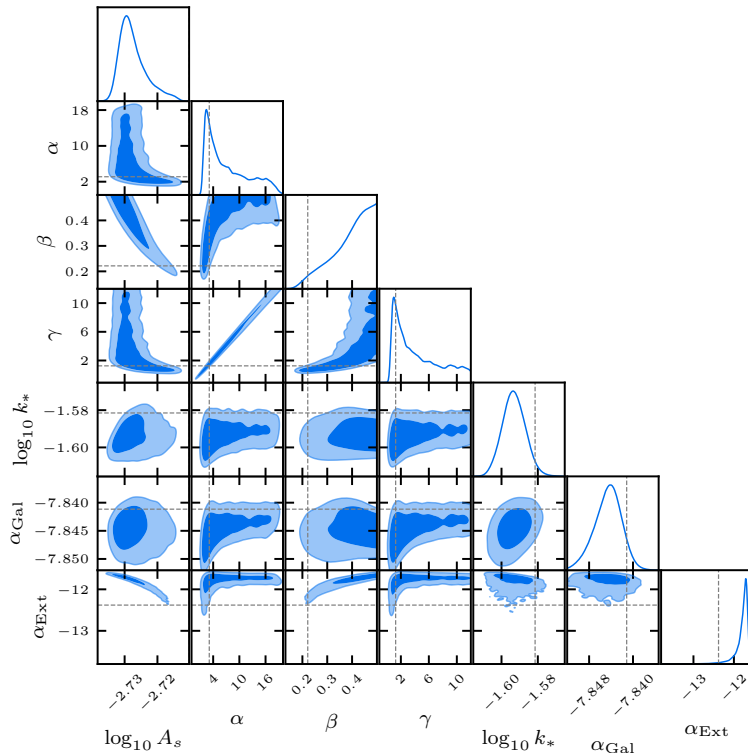


Figure 8. Same as Fig. 5, but for a recovered BPL curvature power spectrum assuming an injected signal motivated by the USR benchmark model. k_* is expressed in $1/s$ units.

Broken power law. The second injected signal is a BPL that is derived from the USR model discussed in Sec. 2.4 and 3.3, with input parameters as in Eqs. (3.7) and (3.8): $\log_{10} A_s = -2.71$, $\log_{10}(k_*/s^{-1}) = -1.58$, $\alpha = 3.11$, $\beta = 0.221$, $\gamma = 1.25$. We reconstruct the signal using a BPL template. The results of the reconstruction of the signal using the USR model will be discussed below. The free parameters for this approach are

$$\theta_{\text{cosmo}} = \{\log_{10} A_s, \log_{10}(k_*/s^{-1}), \alpha, \beta, \gamma\}. \quad (6.3)$$

In Fig. 8 we show a corner plot of the reconstructed parameters of the broken power-law template, while Fig. 9 displays the posterior predictive distribution for the SIGW (left panel) and curvature power spectrum (right panel). While the amplitude of the \mathcal{P}_ζ peak A_s and the peak position k_* are well reconstructed, the infrared (IR) spectral index α and the smoothing coefficient γ are poorly constrained, and α and γ appear to be very degenerate as the IR tail of the signal is hidden by the galactic foreground. This can be seen in the corner plot of Fig. 8 as well as from the right panel of Fig. 9, where the slope for $k < k_*$ has a large uncertainty. In order to reconstruct α and β with some precision, one would need to be sensitive to the tails of the signal outside the peak region. This would be only possible for a much larger signal, which nevertheless would have to compete with stringent bounds from PBH overproduction. With the relatively low SNR injected here, changes in the tilt can be traded for a smoother turnover around the peak, and vice versa.

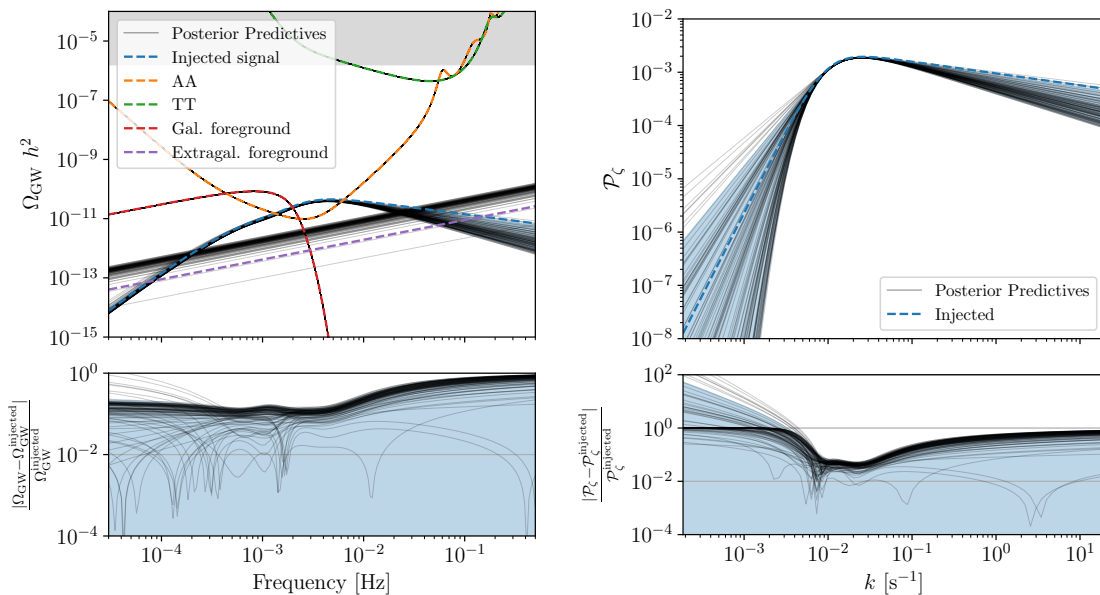


Figure 9. Same as Fig. 3, but for an injected signal from a BPL \mathcal{P}_ζ , recovered using the BPL template. The injected parameters are motivated by the USR benchmark model.

Furthermore, there is a residual correlation between β and γ , although it is less pronounced. Biases in A_s , β , and α_{Ext} are also evident due to their degeneracy in the high-frequency tail. Specifically, there is a tendency to reconstruct higher foreground values compared to the UV part of the SIGW spectrum. Importantly, we have verified that this bias is not an artifact introduced by the additional degeneracies induced by γ , which is correlated with both tilts and amplitude. This conclusion is supported by tests we ran with γ fixed to its injected value.

Notably, this bias does not appear when the same signal is reconstructed using the USR model. The USR model is inherently less flexible, and its UV tilt is better constrained, thereby mitigating the impact of degeneracies.

In Fig. 10 we show FIM estimates of uncertainties on the tilt parameters depending on the injected BPL shape and k_* . Tilts and γ can be independently resolved only if one observes with sufficient SNR the tail of the signal. Otherwise, a shallower (steeper) tilt can be traded off for a smoother (faster) transition. For this reason, in part of the parameter space explored in Fig. 10, we would obtain ill-conditioned FIM. In order to avoid this, only in this case we remove γ from the parameters of the FIM and fix it to the injected value.

The left panel of Fig. 10 shows the absolute uncertainty achievable on α in the (k_*, α) plane, and the right panel shows the same for β . We checked that these uncertainties do not depend on the injected value for the other tilt parameter. The slope of the IR tail of the GW spectrum is only mildly dependent on α , as discussed before, so most of the sensitivity comes from the signal in the frequency range around the peak. For this reason, the uncertainty on α reduces to 0.1 or better only if the SIGW is well within the LISA range, and on the right of the galactic WD foreground ($10^{-2} < k_*/s^{-1} < 10^{-1}$). Still,

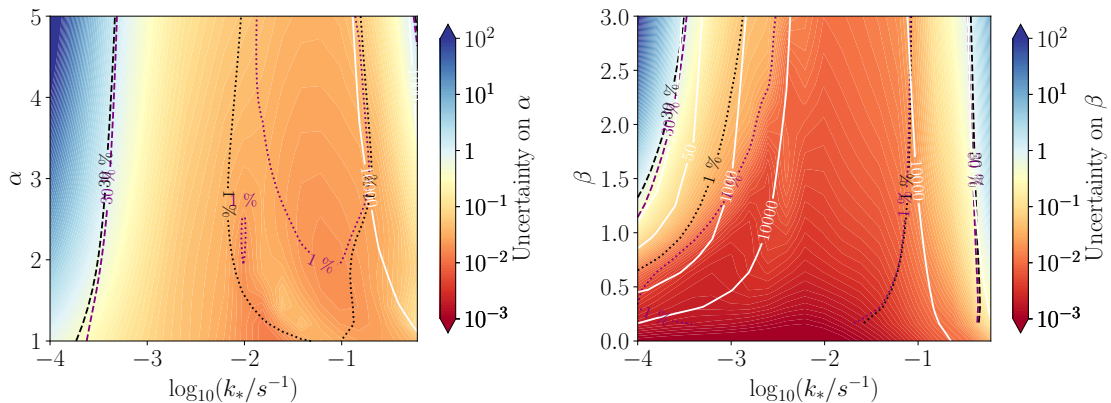


Figure 10. Uncertainty on α (left panel) and β (right panel) computed with the FIM approach for the broken power law \mathcal{P}_ζ . The remaining parameters injected are those of the benchmark scenario in Eq. (3.8). We fix γ to the injection to remove the degeneracies with the two tilts in the small SNR regions of the parameter space.

it is very interesting to notice that steep values of the tilt, higher than $\alpha \simeq 1.5$, which are fully covered by the causality tail $\Omega_{\text{GW}} \sim f^3$ [389, 391, 392] in the SIGW spectrum (up to log-corrections), can be well constrained, as information on the tilt is still retained in the shape of the double peak feature of the signal close to the dominant peak. The sensitivity to β (right panel of Fig. 10) is instead much better, as it determines the UV slope $\Omega_{\text{GW}}(f) \sim f^{-2\beta}$. Therefore, β cannot be measured with an uncertainty smaller than 0.1 only if the SIGW lies outside LISA’s peak range ($k_* > 10^{-1} \text{ s}^{-1}$) or if $\beta \gtrsim -2$, where the SIGW background falls too quickly in the UV.

6.2.2 Spectra with oscillations

Turns in multi-field inflation. As a benchmark example of a primordial feature in the power spectrum, we analyze a signal arising from turns in multi-field space as introduced in Sec. 3.2.2. The free parameters for this analysis are

$$\boldsymbol{\theta}_{\text{cosmo}} = \{\log_{10} A_s, \log_{10}(k_*/\text{s}^{-1}), \delta, \eta_\perp, F\}. \quad (6.4)$$

In Fig. 11 we show the posterior distributions for key parameters governing the sharp-turn scenario in multi-field inflation, along with the foreground parameters. The injection assumes the benchmark scenario where the parameters controlling the template (3.9) are fixed as in Eq. (3.12). We see that in this case, the parameter F is constrained to be close to unity with better than percent precision, showing the high sensitivity to the template oscillations. In this case, the signal amplitude and central scale k_* are weakly correlated, while the former is still positively correlated to both δ and η_\perp which control the enhancement factor. Due to the ideal location of the SIGW peak, we also observe weak correlations between the foreground parameters and the signal parameters.

Figure 12 shows the posterior predictive distribution for Ω_{GW} and \mathcal{P}_ζ . In this example, the main peak of the SGWB lies within the LISA sensitivity band and above both astro-

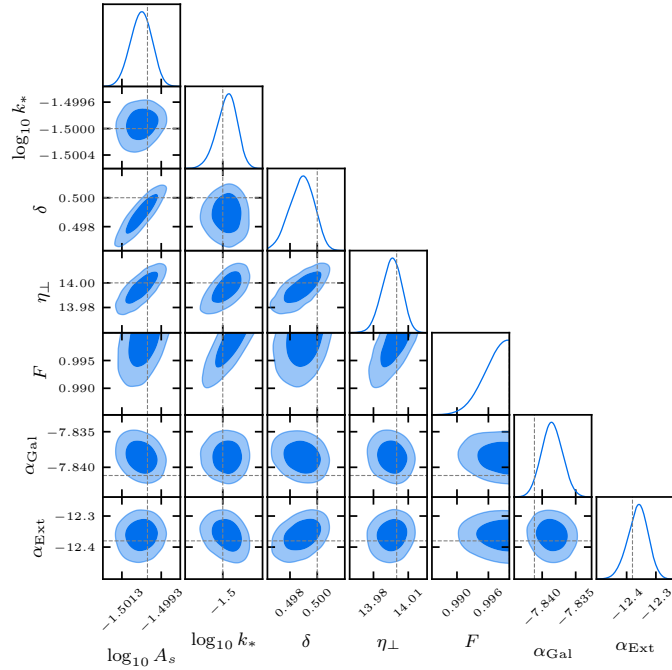


Figure 11. Same as Fig. 5, but for a simulated signal motivated by the multi-field scenario with sharp turns from (3.9). k_* is expressed in 1/s units.

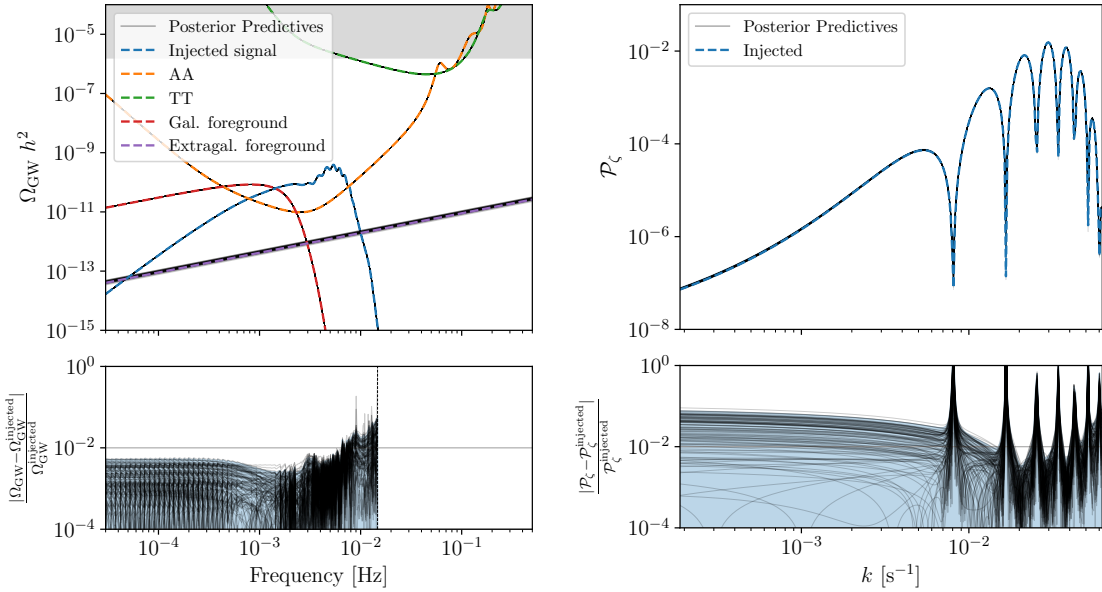


Figure 12. Same as Fig. 3, for the signal generated through a multi-field scenario with sharp turns from Eq. (3.9).

physical foregrounds. As a result, both the shape and amplitude of the peak in Ω_{GW} , along with the $O(20\%)$ modulations, are reconstructed at the percent level. Since the frequency

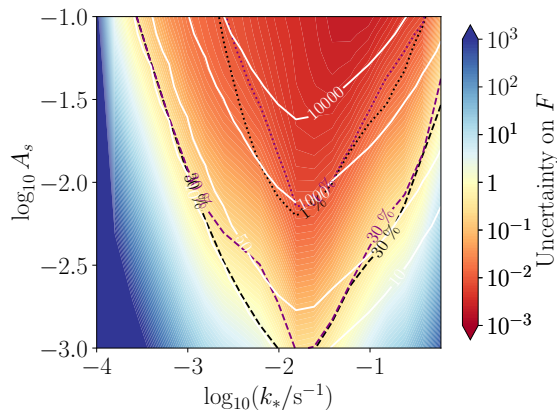


Figure 13. Fisher analysis for the oscillation template from multi-field inflation with turns. We vary k_* and A_s while keeping the remaining parameters fixed to the benchmark values (3.12).

of these modulations is linked to the oscillations in \mathcal{P}_ζ through the assumed thermal history at horizon re-entry, the oscillations are also reconstructed with high accuracy—see the right bottom plot. In this fortunate case, it would be possible to pinpoint the duration and strength of the field-space turn, as well as the inflationary time scale of the phenomenon. The latter is related to the oscillation frequency, as it is customary from the sharp feature phenomenon, while the former two can be disentangled by combining the peak amplitude, its location, and the frequency of the modulations.

Finally, the results of a Fisher analysis, highlighting the uncertainty in the parameter F associated with the oscillatory behavior, are presented in Fig. 13. There, we vary the power spectrum amplitude A_s and the position of the main peak, while keeping the other parameters fixed to the benchmark values discussed just above. This simplification is useful for illustrative purposes, as the parameters in the current model are not independent. Notably, when the signal is centered near the LISA sweet spot at $\log_{10}(k_*/s^{-1}) \simeq -2$, the oscillations can be accurately detected even with a moderate enhancement such as $\log_{10} A_s \simeq -3$.

Rapid transitions between SR and USR phases. The other injected spectrum with oscillatory features is characteristic of single field models with fast transitions from an SR to a USR phase described by Eqs. (3.13), (3.14). The free parameters for this analysis are

$$\theta_{\text{cosmo}} = \{\log_{10} A_s, \log_{10}(k_*/s^{-1}), \nu_I, \nu_{II}, F\}. \quad (6.5)$$

We consider the benchmark scenario with the input parameters listed Eq. (3.18): $\log_{10} A_s = -2.58$, $\log_{10}(k_*/s^{-1}) = -2.02$, $\nu_I = 1.95$, $\nu_{II} = 1.61$, $\gamma = 1.67$, $F = 1$. We perform the MCMC Bayesian inference modelling of the signal using the template (3.14), which allows us to turn on the oscillations smoothly by varying the parameter F from 0 to 1. The value $F = 0$ corresponds to a featureless BPL similar to the one considered above. Furthermore, we fix γ as the strong degeneracy between α and γ (see Fig. 8) makes sampling challenging and since our main concern lies in constraining F .

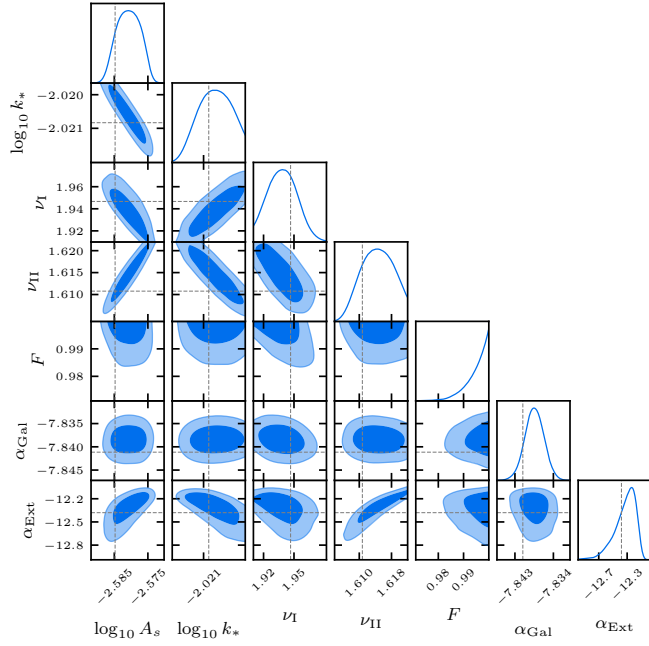


Figure 14. Same as Fig. 5, but for a simulated signal from Eq. (3.14). k_* is expressed in $1/s$ units. Note the injected value $F = 1$ is not visible sitting at the edge of the plot.

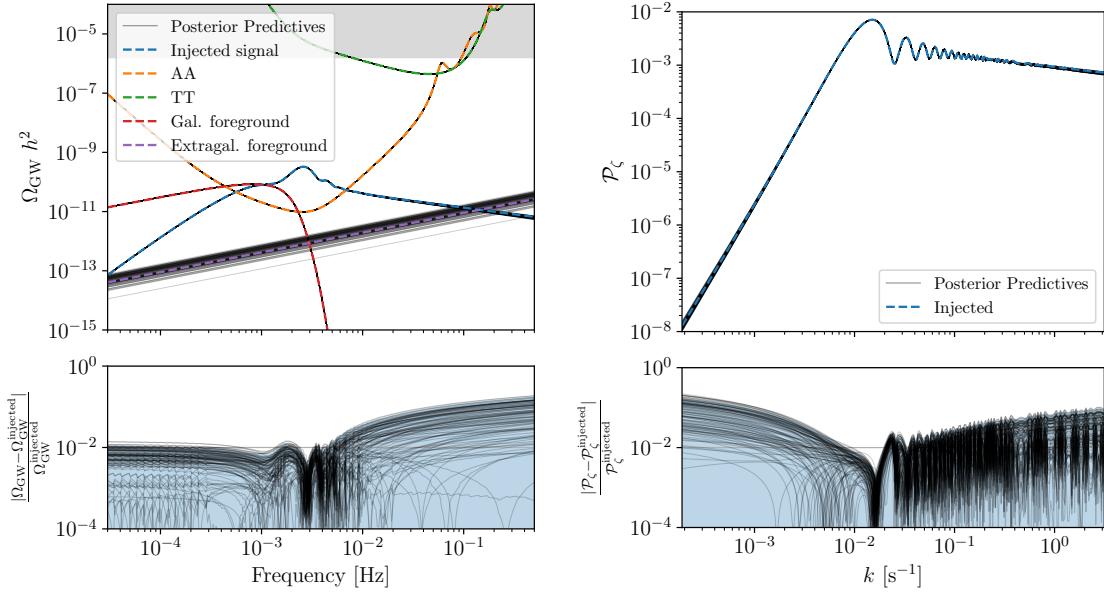


Figure 15. Same as Fig. 3, for the signal generated through a fast transition from SR to USR from (3.14). Both \mathcal{P}_ζ and Ω_{GW} are reconstructed very well.

In Fig. 14 we show the posterior distribution for each parameter of the signal and foregrounds. First of all, we see the parameter F controlling the relevance of the oscillations

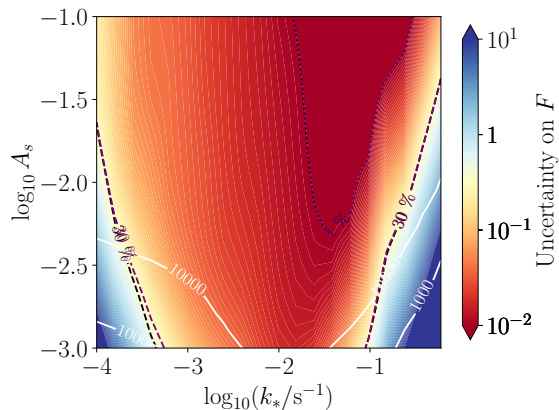


Figure 16. Absolute uncertainty on F estimated using the FIM for the oscillation template from a sharp transition between SR and USR. We vary $\log_{10} k_*$ and $\log_{10} A_s$ while keeping the remaining parameters fixed to the benchmark values (3.18).

over the smooth BPL is very tightly constrained around unity. This tells us the presence of oscillations can be resolved with high accuracy for such a high-SNR signal. The sensitivity to oscillations is mainly driven by the dominant peak, as we will discuss in the following. We also find tight correlations between the parameters, which are non-trivially connected in the signal template (3.13). In particular, we observe a strong correlation between the BPL tilts and the amplitude, due to the large impact of the former on the overall amplitude of the dominant peak. The negative correlation in the (A_s, k_*) plane is probably induced by the way the dominant peak, contributing to most of the SNR, can be adjusted, as one could lower the characteristic scale by enhancing the amplitude.

In Fig. 15 we show the posterior predictive distribution for both Ω_{GW} and \mathcal{P}_ζ . The presence of a dominant peak at scales around k_* in the right plot leads to a distinctive large enhancement of the SIGW signal around peak frequencies seen in the left plot. Additional oscillations in the SIGW spectrum can be observed at larger frequencies, although the second-order emission soon washes out further oscillations in the UV tail. The residuals of Ω_{GW} show that the IR tail of the signal is reconstructed at around the percent level, with a flat behavior due to the causality tail dominating the IR. On the other hand, the relative deviation grows larger than $\mathcal{O}(10)\%$ percent in the UV part of the plot, due to the finite precision at reconstructing ν_{II} . The best accuracy is obtained around the peak, as expected. Correspondingly, in the right plot, \mathcal{P}_ζ is reconstructed with better than percent accuracy around the peak, while the reconstruction degrades in both tails. The oscillations are reconstructed for a few cycles in k , while they are lost in the UV as seen in the bottom panel showing the relative deviation from the injected signal. The envelope of the out-of-phase oscillations behaves following the underlying power-law tail. Note that the tails are reconstructed better than in the pure BPL scenario, as in this template (3.14), the shape of the dominant peak also brings information on the parameter $\nu_{\text{I,II}}$ controlling the tails.

We perform a Fisher analysis focusing on the uncertainty on F , by varying $\log_{10} A_s$ and $\log_{10} k_*$, see Fig. 16. The oscillations are very well recovered, to $\mathcal{O}(10^{-2})$ uncertainty,

if the peak of the signal falls within the LISA band. This is because the oscillations in \mathcal{P}_ζ translate into oscillations mainly around the peak in the SGWB, as visible in Fig. 15.

6.3 Single field USR inference

In Fig. 17 we show the reconstruction capability of the USR model parameters of Sec. 2.4, obtained by running a MCMC Bayesian inference using the USR inflationary model with free parameters

$$\boldsymbol{\theta}_{\text{cosmo}} = \{\lambda, v, b_l, b_f\}. \quad (6.6)$$

controlling the inflaton potential. We assume that the CMB scale crosses the Hubble sphere $N = 58$ e -folds before the end of inflation. We therefore avoid modelling the reheating era, and postpone its inclusion for future work (see e.g. [393]). The input values determining the injected signal were introduced in Eqs. (2.4) and (2.6), but we report them here for convenience: $\lambda = 1.47312 \times 10^{-6}$, $v = 0.19688$, $b_l = 0.71223$, $b_f = 1.87 \times 10^{-5}$.

We understand the results as follows. The height of the peak in \mathcal{P}_ζ is proportional to λ and it is also sensitive to the tuning of b_f .¹⁷ This results in the negative correlation between λ and b_f . The self-coupling λ can be constrained, even though with only $\mathcal{O}(1)$ precision, because it controls the slope of the potential and therefore the SR parameter η_H before the inflection point, which determines the growth of \mathcal{P}_ζ before the peak as discussed below Eq. (3.7). The parameters b_l and v appear to be strongly correlated, meaning that the linear term in b_l/v in Eq. (2.4) gives the dominant dependence on b_l in the potential. The galactic background is well reconstructed due to its large magnitude, while the extragalactic one is completely hidden by the USR signal.

Figure 18 shows the posterior predictives in $\Omega_{\text{GW}} h^2$ and in \mathcal{P}_ζ . It is interesting to compare the right panel of this figure with that of Fig. 9, which is obtained with the same injected signal but a different template for the reconstruction. In the present case, the spectrum of scalar perturbations \mathcal{P}_ζ is reconstructed with excellent precision, even if LISA is sensitive only to the peak. This comes from the fact that the spectrum for the USR model has a universal slope $\sim k^4$ in the IR, whereas the IR slope is a free parameter for the BPL model.

The relatively large uncertainty on the overall potential amplitude $V(\phi)$ in Fig. 19 is due to the degeneracies between the overall scale $V_0 \sim \lambda v^4$ and the parameter b_f controlling the enhancement. As we are only constraining the enhanced part of the spectrum, there is a tight correlation between λ and b_f . Adding information from CMB data in the inference would reduce this uncertainty by adding an independent constraint on V_0 .

Comparison between different methods. We can compare the performance of different methods when fitting the same injected signal, which is taken to be the USR benchmark scenario. In Fig. 20 we show the upper bound at 95% C.L. on the relative difference between the posterior predictive distribution and the injected signal for the binned, template-based, and ab initio USR approaches.

¹⁷With other potential parameters fixed, we did find the approximate behavior $\mathcal{P}_\zeta \propto (1 - b_f/b_{f,*})^{-n}$ in the parameter region supporting peaked \mathcal{P}_ζ . Here, $b_{f,*}$ and $n > 2$ are parameters that depend on the remaining parameters of the potential. Such scaling is observed in other models [123].

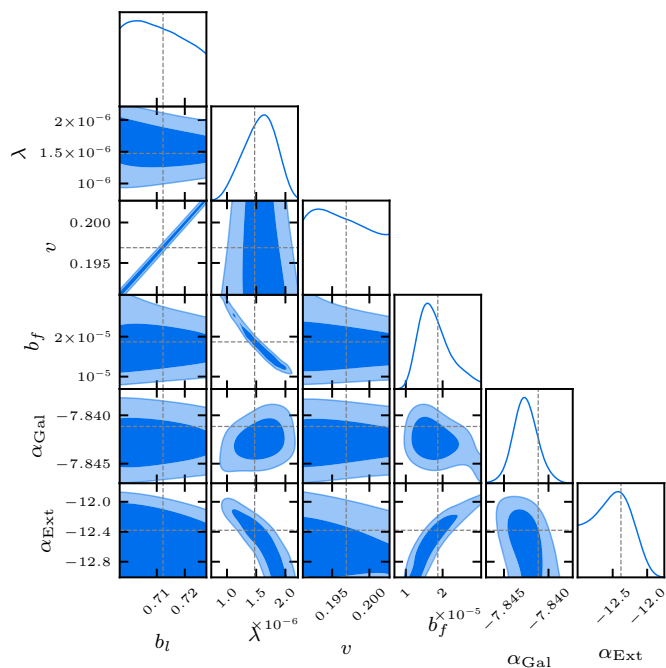


Figure 17. Same as Fig. 5, but for the UR reconstruction of the benchmark scenario.

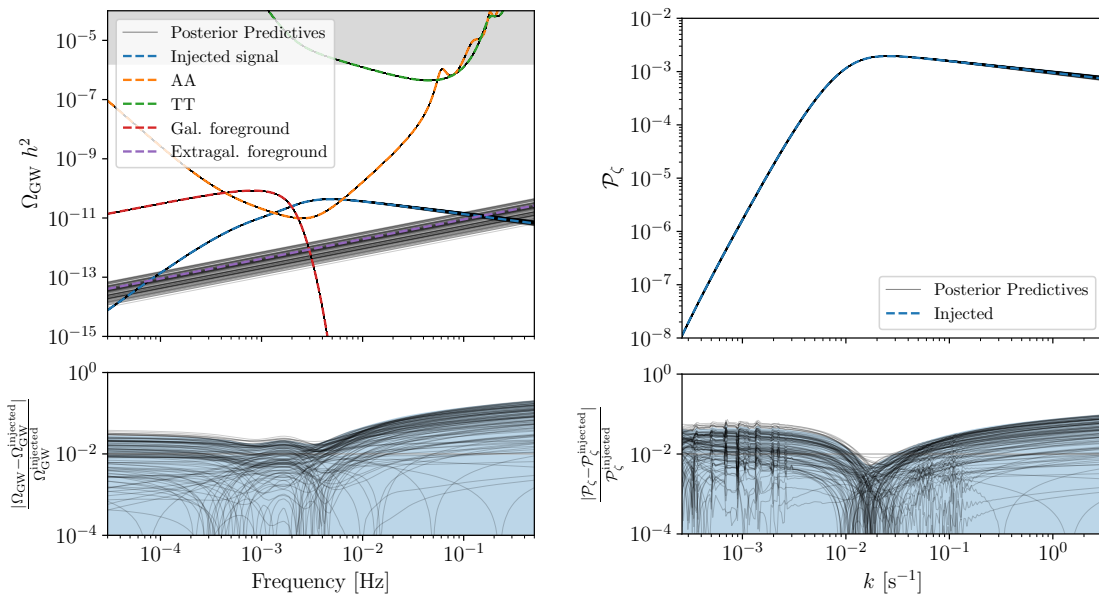


Figure 18. Same as Fig. 3, but for the UR reconstruction of the benchmark scenario.

We observe that the binned method provides a competitive constraint on $\Omega_{\text{GW}} h^2$ in the central frequencies close to the peak (barring oscillations induced by the poor resolution associated with choosing 15 bins). However, the constraint quickly degrades at both ends,

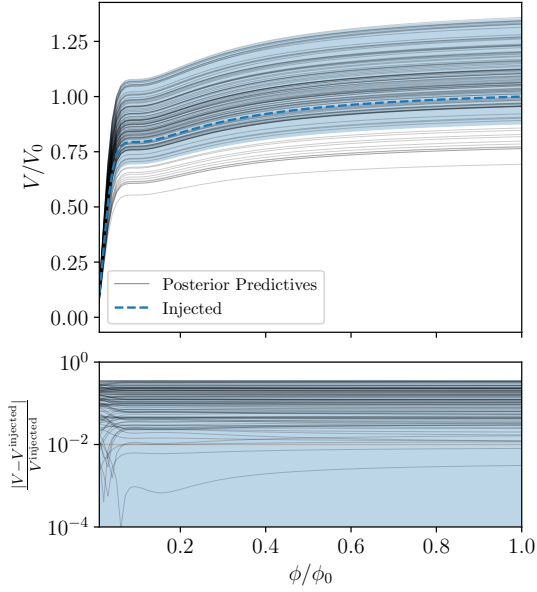


Figure 19. Posterior predictive distribution of the potential $V(\phi)$ for the USR reconstruction of the benchmark scenario.

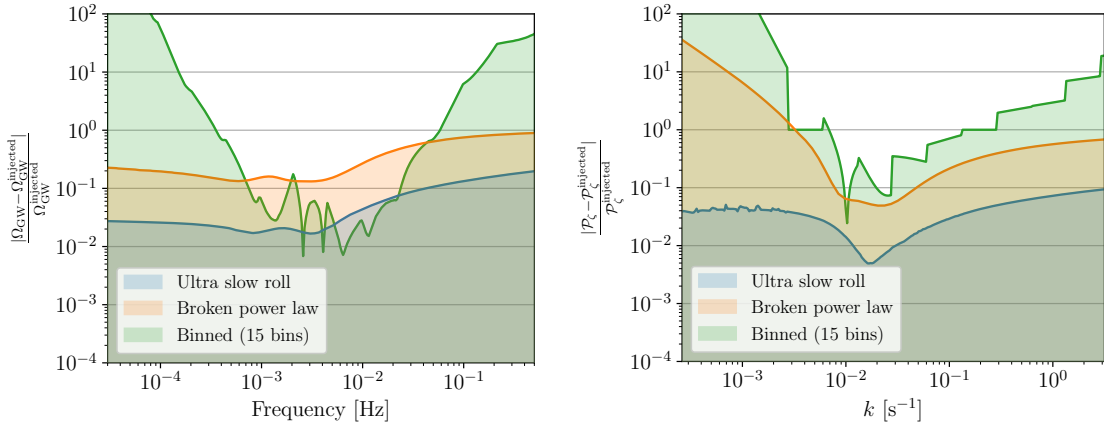


Figure 20. Comparison of the residuals between the three different methods for recovering the signal injected assuming the benchmark USR model.

due to the unconstrained curvature spectral amplitude there. The template-based method (assuming a priori a SIGW from a BPL scalar power spectrum) improves the reconstruction of the tails, but results in an overall loss of precision of a factor $\mathcal{O}(6)$ with respect to the posterior predictive derived assuming the USR scenario. This is most probably due to the larger number of parameters in the BPL template compared to the USR model, and the known degeneracy between γ and the two tilts around the peak.

Also, \mathcal{P}_ζ , shown in the right panel, is most tightly constrained when using the USR model, showing the effectiveness and robustness of our analysis pipeline in reconstructing the injected high SNR signal. The BPL template gives an intermediate result on the IR tail,

which, however, degrades much faster than USR, due to the limited information on the tail of the SIGW, which is mostly controlled by the causality tail. Finally, the binned method gives a worse reconstruction of both the IR and UV tail, due to the small information within the LISA band about these regimes, and the independence assumed in this method between the central bins (best constrained) and the ones on the sides.

Overall, the binned method proves to be a powerful approach to explore the interpretation of a primordial background at LISA within a more agnostic approach. The comparison with specific SIGW templates does not significantly outperform the binned method for the range of frequencies around the peak, which are the best constrained by LISA. However, consistently with expectations, adopting the correct USR model provides greater accuracy in capturing the features of the signal, leading to a more precise reconstruction. These findings demonstrate the power of also adopting inference analyses based on explicit *ab initio* models (of which USR is just an example) that could outperform traditional template-based approaches. This, of course, assumes one can identify the best early universe model through model comparison. We will come back to discussing how to compare different scenarios in Sec. 7.

6.4 Non standard thermal histories

Using information on the SIGW spectrum, LISA would be able to challenge the vanilla assumption that the SIGW was emitted during a RD era. As discussed in Sec. 4, the kernels entering the computation of the SIGW spectrum bring information about the equation of state around the epoch of SIGW emission.

A sudden transition from eMD era to the RD era. We exemplify this case by showing how LISA can constrain the SIGWs emitted within an alternative thermal history by considering an early period of matter domination (eMD). We further assume sudden reheating, as introduced in Sec. 4.3. As we discussed, during this eMD epoch Φ does not decay, leading to an enhancement of the SIGW spectra around the scale $k \gtrsim 1/\eta_R$. We take as a benchmark a nearly scale-invariant spectrum \mathcal{P}_ζ , with a cutoff at placed at k_{\max} . We simplistically describe the spectrum as

$$\mathcal{P}_\zeta(k) = A_s \Theta(k_{\max} - k), \quad (6.7)$$

with benchmark parameters

$$A_s = 2.1 \times 10^{-9}, \quad \eta_R = 2000 \text{ s}, \quad k_{\max} = 0.06 \text{ s}^{-1}. \quad (6.8)$$

Therefore the free parameters to examine in this case are

$$\boldsymbol{\theta}_{\text{cosmo}} = \{A_s, k_{\max}, \eta_R\}. \quad (6.9)$$

Our phenomenological parametrization should be regarded as a toy model, with the UV cut-off scale k_{\max} introduced to ensure perturbativity, as assumed when computing the SIGW. For this reason, given the fact that the energy density contrast grows linearly with the scale factor during a MD era, i.e. $\delta\rho/\rho \propto a$, one can associate k_{\max} as the scale at which

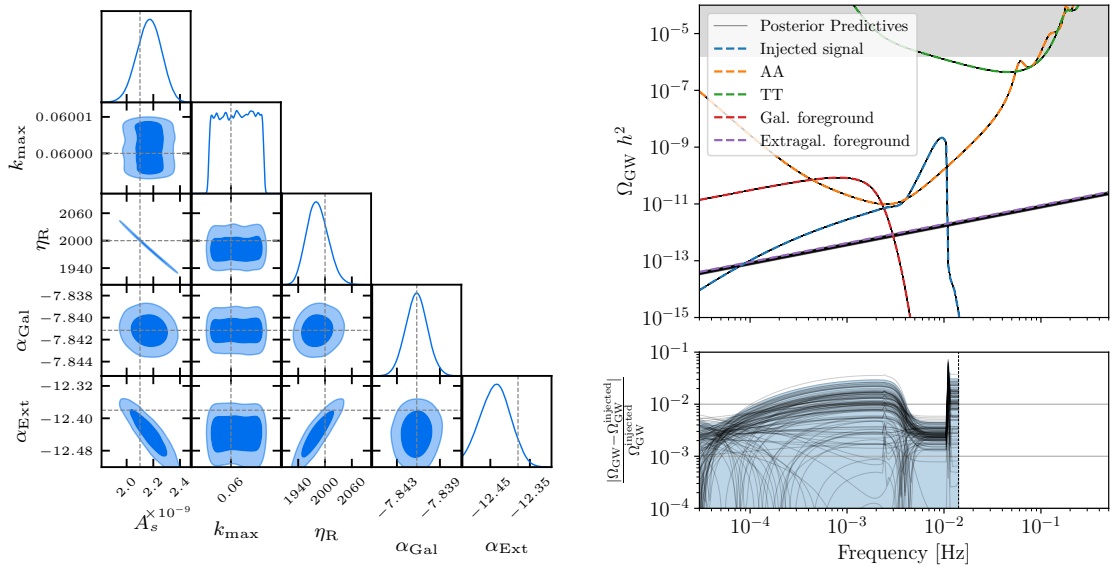


Figure 21. Left panel: Same as Fig. 5, but for the case of a nearly scale-invariant power spectrum and a sudden eMD to RD transition. k_{\max} and η_R are expressed in units of s^{-1} and s , respectively. Right panel: Corresponding posterior predictive distribution for $\Omega_{\text{GW}} h^2$. The notation used matches the one in Fig. 3.

the power spectrum of density contrast becomes unity, i.e. $\mathcal{P}_\delta(k_{\max}) = 1$ [302, 303, 394], although our actual choice is slightly more restrictive. One then can easily understand why k_{\max} depends on the scale we are probing, as the source is largest for modes that spent the most time within the horizon during the eMD era. While we do not model the non-linear part of the spectrum, it may lead to further observational signatures [211, 395–397]. Finally, the template (6.7) can be made more realistic by introducing a smooth cut-off.

The parameters of this template are accurately reconstructed as shown in Fig. 21 (left panel). We notice that η_R and A_s are strongly correlated, as the duration of the MD signal directly controls the growth of perturbations emitting SIGWs, which is therefore degenerate with the primordial amplitude. The cut-off scale is also strongly constrained, with a marginalised posterior distribution which is flat within a narrow range of scales corresponding to the resolution adopted in this forecast. It should be kept in mind, however, that more realistic spectra would feature a smoother drop-off, alongside a contribution from non-linear scales not included here, thus jeopardizing the relevance of the constraining power on k_{kmax} . In the right panel of Fig. 21, we show the posterior predictive distribution for the SIGW. We find the reconstruction to be accurate up to the cutoff scale (better than a few %). The SIGW spectrum is reconstructed well in the large-scale approximation, with the resonant amplification improving accuracy by an order of magnitude. The resonant peak is reconstructed with a larger accuracy due to its milder model dependence and due to its tilt being controlled by the resonant conditions (see discussion around Eq. (4.23)). Moreover, that part of the signal appears with a larger SNR in the LISA detector. The associated \mathcal{P}_ζ is accurately reconstructed as a flat spectrum with a maximum relative error

of order 10%.

Our numerical pipeline can also be applied to other scenarios for the thermal history of the early Universe. Of particular interest would be the study of time-dependent EoS parameters on the SIGWs, like in the case of smooth-crossovers [398, 399], analogous to the QCD phase transition.

6.5 Non-Gaussian effects on SIGWs

As discussed in Sec. 4.5, the tensor power spectrum of SIGWs receives contributions from the four-point correlation function of curvature perturbations. This contribution can be split into disconnected and connected terms. While the disconnected one depends only on the scalar power spectrum, the connected part arises from the primordial trispectrum, i.e. it is sensitive to primordial NG. And, as stressed in Sec. 4.5, for local NG, τ_{NL} would be the key observable to extract a constraint on NG from SIGWs. However, when the curvature perturbation originates from a single fluctuating degree of freedom beyond the inflaton, the parameters τ_{NL} and f_{NL} are connected as measures of higher-order correlations in the curvature perturbation, satisfying the relation $\tau_{\text{NL}} = (\frac{6}{5}f_{\text{NL}})^2$, which saturates the Suyama-Yamaguchi inequality [400]. This relation has relevant implications for SIGWs, generated by models characterized by local-type NG, since observational constraints on one parameter can indirectly provide bounds on the other, assuming a given model. In the following analysis, we adopt the strategy of performing the analysis considering f_{NL} as a parameter of the model and assume the shape (4.38) of the full power spectrum. We then discuss the implications for τ_{NL} that derive from the constraints on f_{NL} . In this case, we assume the curvature power spectrum to have a LN profile, (see Eq. 3.5)¹⁸ and as free parameters we use

$$\theta_{\text{cosmo}} = \{\log_{10} A_s, \log_{10} \Delta, \log_{10} (k_*/s^{-1}), f_{\text{NL}} \equiv 5/6\sqrt{\tau_{\text{NL}}}\}. \quad (6.10)$$

The left panel of Fig. 22 shows the absolute uncertainty associated with f_{NL} varying the parameter f_{NL} against $\log_{10}(k_*)$ computed using the FIM method. We fix the amplitude of \mathcal{P}_ζ to $\log_{10} A_s = -2$ and the width to $\log_{10} \Delta = -0.75$. The dashed black (purple) contour lines represent the relative percentage error associated with f_{NL} when astrophysical foregrounds are not included (or are included). The white vertical line indicates the SNR. Notice that for small and large values of k_* , f_{NL} exhibits higher uncertainties, whereas the intermediate range of $k_* \sim 10^{-2} - 10^{-1} s^{-1}$ shows the minimal uncertainties for f_{NL} . This suggests that tight constraints on f_{NL} can only be achieved within this specific range of k_* . Outside of this range, the errors increase notably, indicating less reliable measurements for f_{NL} . Even in the optimal case, the reconstruction of f_{NL} only reaches the percent level for large $f_{\text{NL}} \gtrsim 12.5$. Notice that, in the presence of foregrounds, the accuracy on f_{NL}

¹⁸Note that our choice of the LN \mathcal{P}_ζ assumes that the dimensionless primordial curvature fluctuations – including the higher order term coming from the trispectrum (the left-hand side of Eq. (4.38) multiplied by $k^3/2\pi^2$) – describe a lognormal. This practically isolates the effect of computing \mathcal{P}_ζ including non-Gaussian contributions *ab-initio* from the effect caused by a NG contribution on the computation of Ω_{GW} given \mathcal{P}_ζ . We will also compare our results to the LN case where only the Gaussian contribution is considered.

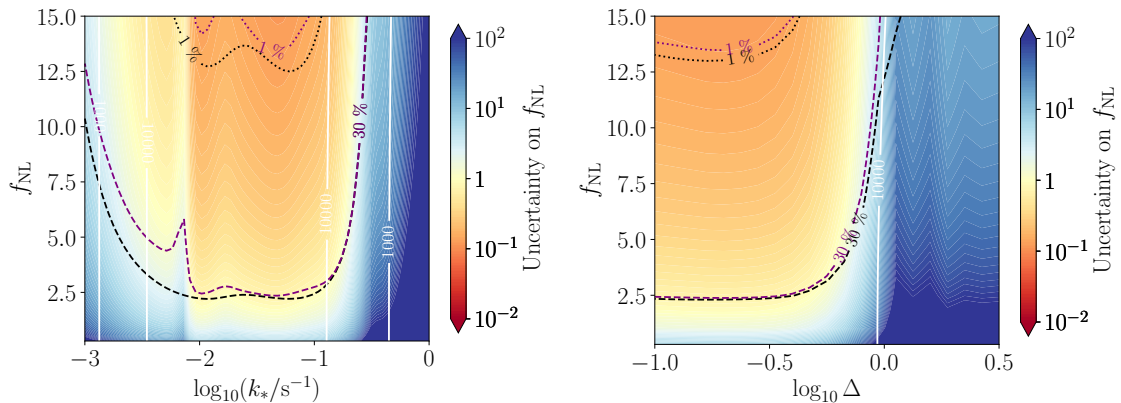


Figure 22. *Left panel:* Absolute uncertainties of each of the parameters in the case of an injected signal which includes NG and assuming the LN template with parameters fixed to $\log_{10} A_s = -2$ and $\log_{10} \Delta = -0.75$. *Right panel:* Same as the left panel, but varying Δ instead of k_* , for an injected signal which includes NG and assuming the LN template with parameters fixed to $\log_{10} A_s = -2$ and $\log_{10}(k_*/s^{-1}) = -1.4$.

slightly degrades, in particular when k_* coincides with the expected peak of the galactic foreground, i.e. when $k_* \sim 10^{-2.2} \text{ s}^{-1}$.

Similarly, the right panel of Fig. 22 shows the FIM absolute uncertainty associated with f_{NL} varying the parameter f_{NL} against $\log_{10} \Delta$. We fix the amplitude of \mathcal{P}_ζ to $\log_{10} A_s = -2$ and the peak scale to the optimal location $\log_{10}(k_*/s^{-1}) = -1.4$. In this case, the uncertainty when estimating f_{NL} is lower ($\lesssim 30\%$) in the region of $\log_{10} \Delta$ below -0.3 , while it significantly degrades for larger widths. This suggests that the most stringent measurements of f_{NL} will be obtained for relatively narrow curvature power spectra.

Given the relation between f_{NL} and τ_{NL} , improvements in the precision of the former directly translate into tighter constraints on the latter. The FIM analysis shows that percent-level accuracy on f_{NL} is achievable only for large f_{NL} , which in turn would correspond to a percent-level constraint on τ_{NL} . In favorable scenarios –where the peak scale k_* lies within $10^{-2} - 10^{-1} \text{ s}^{-1}$ and the spectral width $\log_{10} \Delta$ is relatively narrow – uncertainties in f_{NL} are minimal, restricting the allowed range of τ_{NL} . Conversely, when f_{NL} is less precisely determined, τ_{NL} remains poorly constrained.

The corner plot in Fig. 23 illustrates the posterior distributions of the SIGW signal parameters $\{\log_{10} A_s, \log_{10}(k_*/s^{-1}), \log_{10} \Delta\}$, including the primordial NG parameter f_{NL} , alongside the extragalactic and galactic background amplitude energy densities $\log_{10}(h^2 \Omega_{\text{Ext}}) \equiv \alpha_{\text{Ext}}$, $\log_{10}(h^2 \Omega_{\text{Gal}}) \equiv \alpha_{\text{Gal}}$. As in the other cases, we omit the LISA noise parameters $A_{\text{noise}}, P_{\text{noise}}$ from the corner plot as they are tightly constrained and weakly correlated with the rest. As first benchmark, we injected a template with $\log_{10} A_s = -2$, $\log_{10} \Delta = -0.75$, $\log_{10}(k_*/s^{-1}) = -2.3$ and $f_{\text{NL}} = 1$. On the right panel of Fig. 23, we report the corresponding reconstructed $\Omega_{\text{GW}} h^2$. For comparison, we also plot the GW energy density in the Gaussian case. Due to the low value of f_{NL} chosen, the reconstructed and Gaussian curves are almost superimposed, showing that the effects of NG are quite

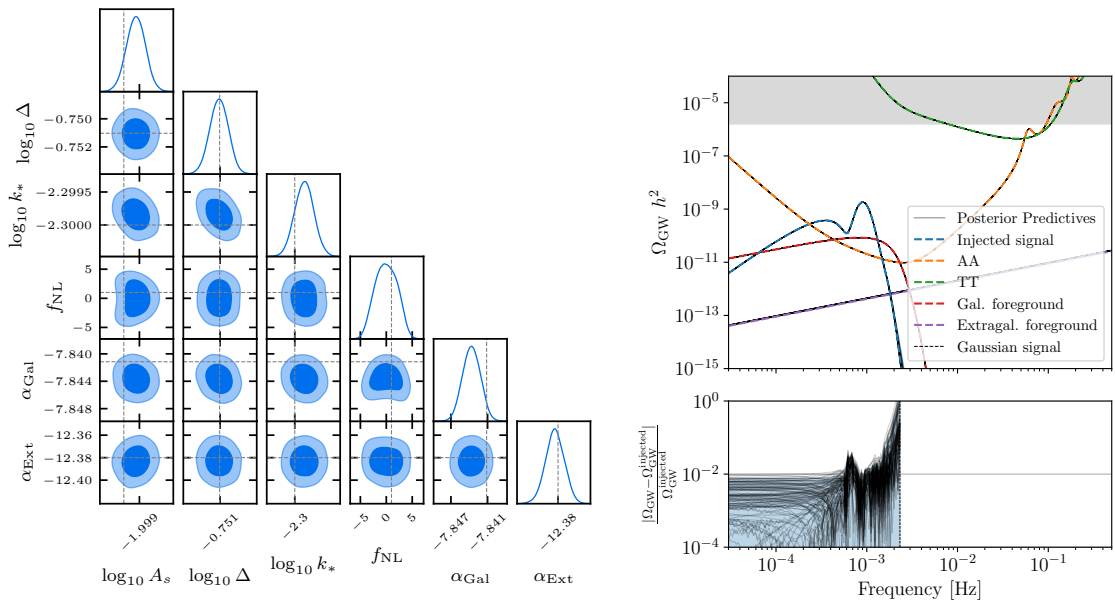


Figure 23. Posterior distribution for an injected signal which includes NG, $f_{\text{NL}} = 1$ and assuming the LN with $\log_{10} A_s = -2$, $\log_{10} \Delta = -0.75$, $\log_{10}(k_*/s^{-1}) = -2.3$.

mild in this case.

The marginalized posterior for f_{NL} exhibits a broad posterior distribution, ranging from -5 to 5 . This distribution indicates a large uncertainty in f_{NL} spanning roughly ± 3 at the 68% C.L. and is compatible with $f_{\text{NL}} = 0$. This suggests a limited constraining power of LISA on f_{NL} . For such a signal, the posterior shows a bimodal structure, that arises because f_{NL} enters quadratically in the GW spectral energy density through the trispectrum. As the observed value suggests compatibility with a Gaussian primordial distribution, the broad posterior distribution also implies that ruling out moderate NG will be challenging, emphasizing the need for improved precision or additional data to refine these estimates. The other parameters, such as the log-amplitude of the seed power spectrum ($\log_{10} A_s$), show a remarkable reconstruction, in line with the results of Sec. 6.2.1. Note however that we are injecting different values of $\{\log_{10} A_s, \log_{10}(k_*/s^{-1}), \log_{10} \Delta\}$. For a comparison to the fully Gaussian case with the same injection in \mathcal{P}_ζ see Fig. 30. The effect of adding the small NG correction $f_{\text{NL}} = 1$ on the recoverability of power spectral parameters $\{\log_{10} A_s, \log_{10}(k_*/s^{-1}), \log_{10} \Delta\}$ and foreground parameters $\{\alpha_{\text{Gal}}, \alpha_{\text{Ext}}\}$ is small in this case, indicating that a small NG contribution does not spoil the reconstruction of curvature power spectra parameters. This also indirectly supports our choice of not including NG corrections in the benchmark USR scenario discussed in Sec. 3.3, which is characterized by $f_{\text{NL}} \simeq 0.09$. However, notice the visible non-zero correlation between f_{NL} and both $\{\log_{10} A_s, \alpha_{\text{Gal}}\}$. The joint posterior $f_{\text{NL}} - \log_{10} A_s$ reflects the multimodality induced by the double peak structure of f_{NL} . Nevertheless, LISA can still strongly constrain the amplitude of the non-linear power spectrum. Hence the detection of the GWB is not strongly influenced by the primordial NG, which is beneficial for simplifying the analysis

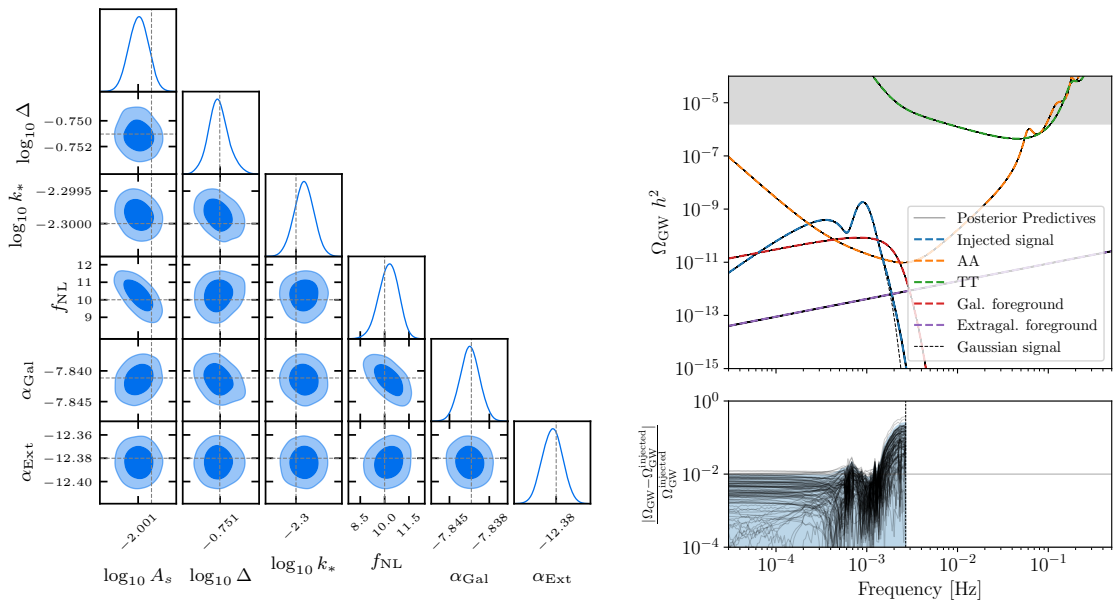


Figure 24. Same as Fig. 23 with $f_{\text{NL}} = 10$. Note that there is a second, identical mode at $f_{\text{NL}} = -10$ as only the square of f_{NL} enters Ω_{GW} . We omitted this mode.

when considering models predicting small NGs.

The posterior distributions for astrophysical foreground amplitudes are broader and show limited correlation with signal parameters. In contrast, instrumental noise parameters are tightly constrained and largely independent of signal estimation. This decoupling ensures robust estimation of the signal amplitude, enhancing the reliability of SGWB detection despite noise uncertainties.

Overall, the joint distributions show only weak correlations, indicating that each of these parameters can be inferred with a good degree of independence from the others.

The situation changes when considering a larger value of f_{NL} , as shown in Fig. 24. Specifically, we run the MCMC with the following injected template with $\log_{10} A_s = -2$, $\log_{10} \Delta = -0.75$, $\log_{10}(k_*/\text{s}^{-1}) = -2.3$ and $f_{\text{NL}} = 10$, differing from the previous benchmark only in the choice of f_{NL} . On the right panel, we report the reconstructed $\Omega_{\text{GW}} h^2$ as well as the Gaussian counterpart for comparison. Given the higher value of f_{NL} , the differences are now more evident, resulting in an enhancement of the UV tail, but also in a slightly higher peak and more smoothed minimum (not visible in Fig. 24). Now, the marginalized posterior distribution for f_{NL} shows only a narrow spread indicating that the estimate of f_{NL} is precise. The absolute value of f_{NL} has a mean reconstructed value that varies about ± 0.8 at the 68% C.L. which makes it incompatible with $f_{\text{NL}} = 0$.

As with the previous case, the non-linear power spectral parameters are tightly constrained and no significant bias is observed with respect to the injected values. Both k_* and Δ are very weakly correlated with f_{NL} , suggesting that their reconstruction is not heavily influenced when f_{NL} is large. However, $\log_{10} A_s$ shows a larger anti-correlation with the f_{NL} . An anti-correlation also appears between f_{NL} and α_{Gal} , probably induced by

the similar IR shape behavior. The tighter constraints associated with such a signal imply that higher levels of NG are easier to constrain, yielding clearer and more reliable effects.

The independence between f_{NL} and other parameters (except for $\log_{10} A_s$), indicated by the weak correlations, suggests robustness in parameter estimation. This means that uncertainties in f_{NL} do not drastically affect the inference of other parameters, resulting in more precise parameter constraints compared to the $f_{\text{NL}} = 1$ case. When f_{NL} is larger, the signal is more distinct, allowing for setting more stringent constraints on primordial NG. Note that the prior in Fig. 24 is restricted to positive values of f_{NL} . Similarly to Fig. 23 the posterior distribution has a second mode at $f_{\text{NL}} = -10$ since it only enters quadratically in the signal.

For the amplitude A_s considered in this case, the imprints due to possible inaccuracies in accounting for the full non-Gaussian behavior for some models of inflation are expected to be negligible when $f_{\text{NL}} = 1$, but could be substantial when $f_{\text{NL}} = 10$, as recently argued by [68]. For this analysis, we neglected those refinements. We further stress that for the enhanced amplitude of the power spectrum considered here, $f_{\text{NL}} = 10$ represents much larger deviations from Gaussianity than on CMB scales, because the expansion parameter determining the relative size of the trispectrum versus power spectrum is $\tau_{\text{NL}} \cdot \mathcal{P}_\zeta$. It is of order one in the current context, while less than 10^{-4} on CMB scales.

Concerning the implications for τ_{NL} , large uncertainties in f_{NL} directly translate into poor constraints on τ_{NL} . For example, for $f_{\text{NL}} = 1$ with a quite broad uncertainty of ± 3 , τ_{NL} could span from values close to zero (if $f_{\text{NL}} \approx 0$) up to $\simeq 23$ (if $f_{\text{NL}} \approx 4$), making it challenging to clearly identify a primordial NG signal. In this range, even moderate NGs become difficult to distinguish from a Gaussian spectrum. Without improved precision on f_{NL} , the corresponding τ_{NL} will remain poorly determined, limiting our ability to discriminate between different levels of primordial NG. When $f_{\text{NL}} = 10$, providing a more pronounced non-Gaussian signal, the corresponding $\tau_{\text{NL}} = \left(\frac{6}{5} \cdot 10\right)^2 = 144$ is now much more tightly constrained. Since the uncertainty in f_{NL} is roughly ± 0.8 , τ_{NL} varies up to a $\pm 15\%$ range. This tighter range is obviously better than the scenario with small f_{NL} . Hence, larger f_{NL} values significantly improve our ability to determine τ_{NL} , allowing LISA to better distinguish between different levels of primordial NG in the SGWB.

Finally, it is important to highlight that while Planck provides constraints that are very close to zero [254], indicating no evidence for primordial NG at large scales, the analysis we are performing for LISA focuses on NG at much smaller scales. LISA's ability to provide tight constraints on f_{NL} suggests that GW detection could play a crucial role in refining our understanding of primordial NG, particularly in scenarios where the signal is expected to be strong. In addition, the sensitivity of LISA to different scales compared to Planck provides an important cross-check, helping to verify any scale dependence for f_{NL} [401, 402]. Overall, while Planck remains a benchmark for CMB-based constraints on f_{NL} at large scales, LISA shows the potential of GW detectors to significantly advance the search for, and the characterization of primordial NG.

7 Testing the scalar-induced hypothesis

In this section, we outline a procedure to test the compatibility of the SIGW hypothesis with a possible SGWB detection. So far, our analysis assumed that the cosmological contribution of the SGWB originates from SIGWs. There are, however, many alternative sources of the SGWB that originate from different physical processes in the early universe. Our goal is to offer a practical approach for assessing the validity of the hypothesis explored in this work—namely, whether or not a hypothetically detected signal originates from enhanced scalar fluctuations of inflationary origin. To this end, we focus on two illustrative scenarios that are distinct in nature, leaving a detailed comparison of various early-universe signals—which is beyond the scope of this paper—for future work. We use the evidence (5.22) as an estimator for model selection. Specifically, given an injected signal, we consider different reconstruction techniques, for which we can compute the (log) evidence using the nested sampler PolyChord [403, 404].

It is important to note that the Bayes factor is a global estimator: it not only assesses the goodness of fit of a model to the data but also incorporates information about the prior volume and its compression as the prior transitions to the posterior. Additionally, given a similar fit to data, it naturally favors simpler models—those with fewer parameters—over more complex ones.

In the following analysis, the different approaches follow two distinct philosophies, depending on whether they assume, or not, that the signal originates from scalar-induced GWs:

1. Using the `SGWBinner` code [61, 62] we can use both a template-based [67], as well as a model-agnostic approach to reconstruct the signal in Ω_{GW} . This does not assume the underlying physics. The templates we use to fit the model in this case are informed by the injection, that is known to us. Of course, with real LISA data, these will be several shapes that are informed by physical processes that can potentially generate SGWBs. On the other hand, the binned approach of the `SGWBinner` divides the frequency space into bins by SNR and then fits a power law within each bin. This results in an agnostic reconstruction of Ω_{GW} .
2. By contrast, the various techniques presented in the previous sections assume that the signal we are considering is coming from SIGWs. Somewhat like with the `SGWBinner`, we can reconstruct the SGWB with the `SIGWAY` in two different ways. One option is to use a template-based approach (see Sec. 3.2), in which a template for \mathcal{P}_ζ is specified. A second possibility is to use the \mathcal{P}_ζ -agnostic (still assuming SIGW to be the source of the SGWB) binned approach, as described in Sec. 3.1.¹⁹ We choose the

¹⁹Let us note that there is a slight difference in the implementation of the binned $\mathcal{P}_\zeta(k)$ approach, compared to the binned Ω_{GW} . In the latter approach, the `SGWBinner` code dynamically selects the optimal number of bins before the nested sampling, based on the Akaike information criterium [405] (we refer the interested reader to the discussion around Eq. (3.6) of [61] for more details). On the other hand, such a feature has not been implemented in the `SIGWAY` code, as there are fundamental difficulties to attempting a similar approach in \mathcal{P}_ζ -space (see App. B for a detailed discussion) so the number of bins for $\mathcal{P}_\zeta(k)$ has to be chosen by hand.

Package	Method	Case 1: not SIGW signal	Case 2: SIGW signal
		$\log \left[Z(\Omega_{\text{GW}}^{\text{LN}}) \right] / 10^4$	$\log \left[Z(\mathcal{P}_\zeta^{\text{LN}}) \right] / 10^4$
SGWBinner	Template	0.5444	-0.5278
	Binned	-0.5625	-0.5479
SIGWAY	Template	-25.6078	-0.5203
	Binned	-25.7934	-2.712

Table 1. \log Bayes factors (normalized to a reference value 10^4) comparing the SGWB reconstruction (either using the injected model as a template, or a model-agnostic binned method) with the SIGW reconstruction for two signals: *i*) a log-normal power spectrum in Ω_{GW} which cannot be generated by SIGW (within the assumptions we are working in), *ii*) a log-normal power spectrum in \mathcal{P}_ζ which generates detectable SIGW. In bold we show the Bayes factors for the recovery which assumes the injected template. As expected, they are the best reconstructions for each injection.

number of bins $N_{\text{bins}} = 40$. For simplicity, in this Section, we assume the SIGW to be produced during the radiation-dominated era.

For illustrative purposes, we simulate the following two qualitatively different signals:

- **Case 1. Not SIGWs.** The first is a narrow lognormal in $\Omega_{\text{GW}}(f)$. This injection serves as an example of a signal that cannot be produced by SIGWs, assuming the modes reenter during RD. In this case, regardless of how narrow the peak in \mathcal{P}_ζ is, the generated SIGW will always exhibit the so-called “causality tail” proportional to f^3 . As a benchmark for this injection, we chose to reproduce the main peak of the double-peak background shown in the top-left panel of Fig. 11 in [67], with a slightly lowered amplitude. This amounts to choosing the following parameters: $\log_{10}(h^2\Omega_*) = -9.5$, $\log_{10}(f_*/\text{Hz}) = -2.21$, $\log_{10}(\rho) = -1.10$ in Eq. (2.8) of [67]. We will henceforth call this signal $\Omega_{\text{GW}}^{\text{LN}}$.
- **Case 2. SIGWs.** The second injection is instead derived from a SIGW scenario. We inject a lognormal power spectrum of curvature perturbations, see Eq. (3.5) and compute the resulting SGWB numerically. The power spectrum parameters used were: $\log_{10} A_s = -2.3$, $\log_{10} \Delta = -0.70$, $\log_{10}(k_*/\text{s}^{-1}) = -1.5$. The resulting shape in the SGWB can be described through the double-peak template in Eq. (2.10) of [67], with parameters $\{\log_{10}(h^2\Omega_*), \log_{10}(f_*/\text{Hz}), \beta, \kappa_1, \kappa_2, \rho, \gamma\} = \{-9.5, -5, 0.242, 0.456, 1.234, 0.08, 6.91\}$. With this choice, the main peak of the SIGW coincides with the injection of **Case 1**.

We fit each of the two injections using the four models specified above. The results of our analysis are summarized in Fig. 25 (see also Fig. 31 in App. D showing the reconstruction including foregrounds), and Tab. 1, which we now comment in order.

Let us begin with **Case 1**. The models that perform the worst in terms of model selection are the two based on the SIGW hypothesis (marked by the row SIGWAY). As shown in the left panels of Fig. 25, both the lognormal and binned $\mathcal{P}_\zeta(k)$ models attempt

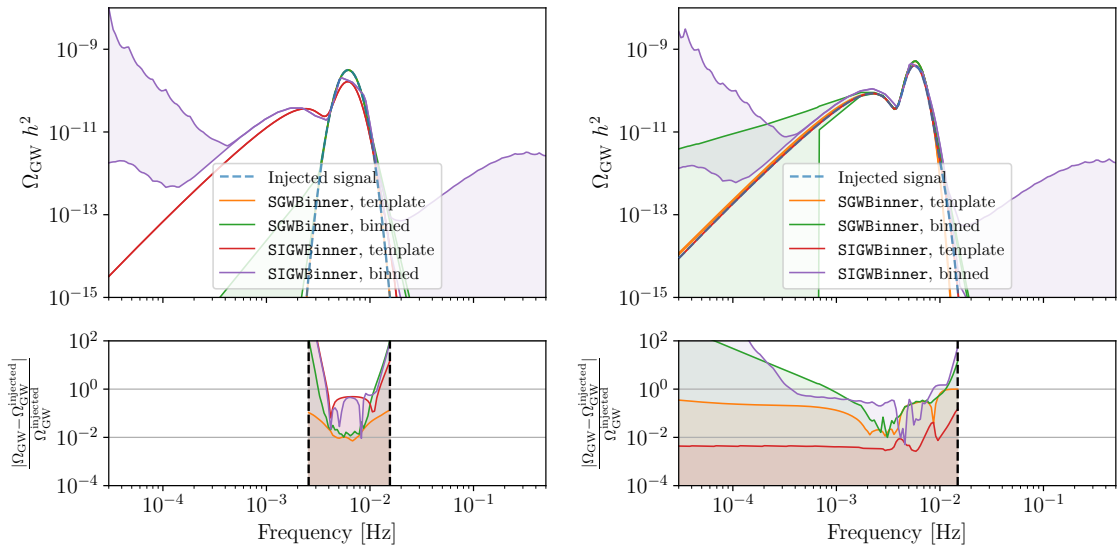


Figure 25. Reconstruction of Ω_{GW} for case 1 (left) and case 2 (right). We only show the reconstruction of the injected cosmological contribution to the SGWB. It is clearly visible that the two models that assume SIGWs cannot reconstruct the narrow log-normal peak in case 1 and therefore lead to much lower evidence. We denote the wrapper to perform the analysis using **SIGWAY** as **SIGWBinner** in this plot.

to fit the lognormal SGWB using the primary peak of the SIGW. However, the secondary peak at lower frequencies severely undermines the fit to the data, resulting in a very poor likelihood value. According to the Jeffreys’ scale (see Sec. 5.2), these models are decisively ruled out when compared to the two alternative hypotheses. As expected the the binned $\mathcal{P}_\zeta(k)$ performs worst, due to its significantly larger number of parameters.

We also fit the same injection using a lognormal template for Ω_{GW} (which corresponds to the true injection) and a binned Ω_{GW} reconstruction with **SGWBinner**. As illustrated in Fig. 25, both models reconstruct the signal very well, closely matching the injection. Furthermore, they yield very similar best-fit likelihood values with a preference for the lognormal template (matching the injected signal) due to its smaller number of parameters.

The main takeaway from Case 1 is that if a similar signal was detected, we could conclude with very high statistical significance that the signal does not have a scalar-induced origin.

We now discuss **Case 2**. In this case, all the models considered successfully capture the injected signal, which consistently falls within the reconstructed contours. Unlike the previous case, the Bayes factors are closer together, while still being orders of magnitude apart (we would like to stress that the differences quoted in Tab. 1 are $\log(Z)/10^4$). Even here, the worst performing models are the free reconstructions – whether in Ω_{GW} or $\mathcal{P}_\zeta(k)$ – as they introduce a large number of parameters despite achieving a good fit. However, their flexibility and agnostic nature make them useful in real data analysis, as they do not require specifying a particular template. Once the main features of the signal are identified, Tab. 1 demonstrates the power of specifying the model.

This injection is detected so well that even using a template for Ω_{GW} developed in [67, Eq. (2.10)] to accurately parameterize a SGWB induced by scalar perturbations, the model is decisively ruled out when compared to the true lognormal-in- $\mathcal{P}_\zeta(k)$ injection. This outcome arises both because the template in [67] is described by seven free parameters compared to three for the lognormal $\mathcal{P}_\zeta(k)$, and because the fit of the latter is slightly better. Despite the former template accurately approximating the signal, it remains a phenomenological model rather than the true description. It is also interesting to stress that, in case 2, the template-based **SIGWAY** method performs better than the template-based **SGWBinner** in reconstructing Ω_{GW} , as can be seen in the right column of Fig. 25. This improvement arises because the assumption of SIGWs enforces a more restricting shape for Ω_{GW} , characterized by a smaller number of parameters. In contrast, the **SGWBinner** imposes weaker restrictions in the reconstruction. On the other hand, when comparing the agnostic approaches, we see that the former gives slightly better Ω_{GW} reconstructions around the peak of the signal, with an oscillatory behavior of the residuals due to the finite resolution of the binned approach (40 bins). This result stresses the importance of adopting optimal modeling of the eventual cosmological scenario when reconstructing the signal (see also App. D).

All in all, the results of this section, although based on two illustrative examples, demonstrate that LISA has the potential to confirm the scalar-induced nature of the SGWB with high statistical significance. These results confirm that the true models (lognormal $\Omega_{\text{GW}}(f)$ and lognormal $\mathcal{P}_\zeta(k)$) achieve the best Bayes factors when appropriately matched. Alternative and binned models consistently show inferior fits, highlighting the distinctiveness of the injected signals.

However, it is important to stress, that not all SGWB that may appear in LISA lead to such a clear difference between signals that can or cannot be generated by SIGW. The characteristic double-peak structure that we observe with the injected $\mathcal{P}_\zeta^{\text{LN}}$ signal is only measurable by LISA if (a) the peak in \mathcal{P}_ζ is sufficiently narrow and (b) both peaks in Ω_{GW} happen to fall within the sensitivity of LISA. On the other hand, there are many potential shapes for \mathcal{P}_ζ where these conditions are not met. In these cases the SIGW signal can easily mimic one expected from other cosmological sources, potentially making it much harder to rule out models. We will leave a more detailed discussion of this for future work.

8 Conclusions

In this work, we investigated the potential of the LISA detector for reconstructing the SGWB sourced by second-order scalar perturbations. Three approaches were explored: A binned spectrum reconstruction, template-based methods, and a direct modeling approach rooted in first-principles scenarios (taken to be the single-field USR inflationary model for presentation purposes).

Our results demonstrate that the direct modeling approach yields the tightest constraints on the primordial curvature power spectrum \mathcal{P}_ζ , particularly capturing both the IR and UV tails of the signal with better precision than alternative methods, due to the stronger prior information inevitably included in the fit. This highlights the power of incor-

porating *ab initio* physics into signal reconstruction pipelines to leverage the constraining power of LISA observations at their best.

The binned spectrum reconstruction approach is complementary and proved effective in providing model-independent upper bounds on \mathcal{P}_ζ when the cosmological contribution to the SGWB is below the sensitivity. Capturing the overall shape of the SIGW spectrum with this approach proved to be difficult, due to a combination of missing SNR towards the edges of the LISA window and strong degeneracies between the bins when choosing a large number of them. Despite these shortcomings, it is possible – if a cosmological contribution to the SGWB is detected – to tell apart signals that can be SIGW from those that cannot, by Bayesian model selection.

In comparison, the template-based methods provided a more consistent reconstruction across frequencies, though they inherently rely on prior assumptions about the shape of the spectrum. The complementary strengths of these approaches suggest that an optimal reconstruction strategy would involve their combined use, with model-dependent templates guiding reconstructions and binned methods offering flexibility in capturing unanticipated spectral features or in setting bounds that are agnostic on the spectral shape.

We also examined the impact of going beyond the simplest vanilla cosmological scenarios on the SIGW reconstruction investigating the sensitivity of SIGW signals to early-universe physics. In particular, we included in our analysis the study of the effect of the transition from early matter-dominated to radiation-dominated eras, as well as the role of non-Gaussianity in the SIGW spectrum. Future research will include the study of the effect of a time-dependent equation-of-state parameter on the SIGW spectrum, as would be generated in the case of a smooth crossover [398, 399], such as in the QCD phase transition. Overall our analysis demonstrated how SIGW searches in LISA will provide constraints that vastly outperform those deduced from the effective number of relativistic species ΔN_{eff} and PBH overproduction bounds. In this regard, SIGW searches will also be an invaluable tool for probing the asteroid mass window of PBH dark matter.

Looking forward, several key avenues remain open for future work. On the phenomenological side, it remains an open question how well LISA will be able to constrain primordial non-Gaussianity or non-standard thermal histories while allowing for a fully non-parametric curvature power spectrum. In this work we have only quoted template-based constraints on these effects, e.g. in Figures 21 and 23, which do not consider possible degeneracies with the shape of the spectrum.

Concerning the binned approach to reconstructing \mathcal{P}_ζ , a more mature method that incorporates assumptions about the smoothness of the spectrum of scalar perturbations and addresses the computational difficulties with the binning will be needed in the future. It is likely that – even allowing for non-Gaussianities and non-standard thermal histories – some shapes of the SGWB cannot be scalar-induced and can be confirmed as signatures of directly sourced tensor perturbations, even without identifying a specific early-universe source.

On the theory side, future work should consider expanding the scope of single-field scenarios by exploring more general actions in the Jordan frame, incorporating non-minimal coupling and non-canonical kinetic terms (e.g. Eq. 2.1 of [83]). Also, going beyond single-

field USR models, first-principle multi-field inflationary scenarios merit investigation, as discussed in Sec. 2.2. In some cases, multi-field models can effectively be reduced to single field descriptions, making some of the techniques developed here already applicable, and enabling simpler parameter space scans as done in [406, 407]. A reverse engineering approach could be particularly valuable, where inflationary dynamics are modeled based on a minimal set of parameters, and the corresponding inflationary potential is reconstructed within single- or multi-field frameworks, as demonstrated in Refs. [268, 408]. Expanding the framework for computing the non-Gaussian signatures predicted in most SIGW models beyond the lognormal template in Sec. 4.5 could serve as a diagnostic tool for breaking degeneracies in cases where the SGWB spectrum alone is insufficient. Also, implementing the binned approach in scenarios with NGs could also allow us to reduce the computational costs of these analyses. While in this work we only considered the monopole signal, as non-Gaussianities may impact the large scale SIGW anisotropies, it would be interesting to include information from higher order in the multiple expansion of power in the sky [316, 409–411]. Finally, integrating these advanced modeling and reconstruction techniques into the global fit pipeline of LISA, as well as incorporating measurements from other experiments, will be essential for unlocking the mission’s full potential in probing the early universe’s cosmological landscape.

Acknowledgments. We thank Nicola Bartolo, Gaetano Luciano, Marco Merchand, Sabino Matarrese, and Toni Riotto for discussions and interactions in an early stage of this project. We acknowledge the LISA Cosmology Working Group members for seminal discussions. We especially thank the authors of refs. [67, 328, 329, 332] for the collaborative developments of the `SGWBinner` code upon which we built to produce many of the forecasts we presented in this work. The research of JF is supported by the grant PID2022-136224NB-C22, funded by MCIN/AEI/10.13039/501100011033/FEDER, UE, and by the grant/ 2021-SGR00872. RR was supported by an appointment to the NASA Postdoctoral Program at the NASA Marshall Space Flight Center, administered by Oak Ridge Associated Universities under contract with NASA. The work of EM is supported by the Italian Ministry of University and Research grant Rita Levi-Montalcini “New directions in axion cosmology”. EM acknowledges the support of Istituto Nazionale di Fisica Nucleare (INFN) through the *iniziativa specifica* TAsP. JE and GN acknowledge support by the ROMFORSK grant project no. 302640. TP acknowledges the contribution of the COST Action CA21136 “Addressing observational tensions in cosmology with systematics and fundamental physics (CosmoVerse)” and of the INFN Sezione di Napoli *iniziativa specifica* QGSKY. He acknowledges as well financial support from the Foundation for Education and European Culture in Greece. DR is supported by the UZH Postdoc Grant 2023 Nr.FK-23-130. During the course of this work, S.RP and DW were supported by the European Research Council under the European Union’s Horizon 2020 research and innovation programme (grant agreement No 758792, Starting Grant project GEODESI). The work of AG is supported by the UKRI AIMLAC CDT, funded by grant EP/S023992/1. The work of AG, GT, and IZ is partially funded by the STFC grants ST/T000813/1 and ST/X000648/1. The work of HV was supported by the Estonian Research Council grants PSG869 and RVT7 and the

Center of Excellence program TK202. M.Pe acknowledges support from Istituto Nazionale di Fisica Nucleare (INFN) through the Theoretical Astroparticle Physics (TAsP) project and from the MIUR Progetti di Ricerca di Rilevante Interesse Nazionale (PRIN) Bando 2022 - grant 20228RMX4A, funded by the European Union - Next generation EU, Mission 4, Component 1, CUP C53D23000940006. JK acknowledges support from the JSPS Overseas Research Fellowships and the INFN TAsP project. GP acknowledges partial financial support by ASI Grant No. 2016-24-H.0. AR acknowledges support from Istituto Nazionale di Fisica Nucleare (INFN) through the *iniziativa specifica* TEONGRAV and by the project BIGA - “Boosting Inference for Gravitational-wave Astrophysics” funded by the MUR Progetti di Ricerca di Rilevante Interesse Nazionale (PRIN) Bando 2022 - grant 20228TLHPE - CUP I53D23000630006.

Authors’ contribution. JE: Main developer of SIGWAY. Implementation and optimization of techniques discussed in App. A, coding the interface to SGWBinner. Co-coding different thermal histories. Running analyses and producing figures for all results except Secs. 6.5 and 7. Writing Secs. 6 and Appendices. Reviewing all draft. AG: Co-coding different thermal histories. Writing Secs. 4.3 and 6.4. Reviewing Sec. 3. GF: Proposing and coordinating the project with RR, including defining goals and managing tasks. Co-coding parts of SIGWAY, mainly on SIGW computations and the USR module. Writing and Reviewing all sections of the draft. TP: Co-coding kernel functions and different thermal histories. Writing Sec. 6.4 and parts of Secs. 2.1, 2.2, 2.3, 3.2 and 8. Reviewing Secs. 6.1, 6.2 and 6.3. MPE: Devising methods for computations in Sec. 3.3 and developing the algorithm for the binned spectrum approach, contributing to the code implementation. Writing Secs. 3.1 and 4.4. Reviewing Secs. 1, 2, 5, and 8. GP: Co-coding SIGW computations with NGs in SIGWAY. Running and producing Figs. for Sec. 6.5. Writing App. A.4 and Sec. 4. Reviewing Sec. 4. MPi: Co-coding SIGW computation in the SIGWAY and interfacing with SGWBinner. Writing Sec. 5. AR: Co-coding SIGW computations with NGs in SIGWAY. Running and producing Figs. for Sec. 6.5. Writing Sec. 6.5. Reviewing Sec. 1. RR: Proposing and coordinating the project with GF, including defining goals and managing tasks. Co-coding the USR module. Writing and Reviewing all sections of the draft. GT: Developing the algorithm for the binned spectrum approach, contributing to the code implementation. Writing Secs. 3.1 and 4.4. Reviewing the draft. MB: Running the analysis and writing of Sec. 7. JF: Running the analysis and writing of Sec. 7. Reviewing Secs. 7, 3.2.2, 2.2 and Sec. 2. JK: Coding SGWBinner. Writing Sec. 5. Reviewing Sec. 3. EM: Contributing to an early version of the USR code. Writing Secs. 2.1, 2.2, 2.4, 3.2, 3.3, 6.2, and 6.3. Reviewing all draft. GN: Writing Sec. 1. Reviewing all draft. DR: Writing Secs. 3 (intro), 4.1, 4.2, and 6.2.1. Reviewing Secs. 4 and 7. SRP: Devising and interpreting Sec. 4.5 and 6.5. Writing Sec. 4.5 and related elements in Secs. 4 and 6.5. Reviewing all draft. HV: Devising Secs. 2 and 3. Writing Secs. 2, 3, and 6.2. Reviewing Secs. 1, 6.4, 6.5, and 8. DW: Devising and interpreting Sec. 4.5. Reviewing Secs. 4.5, 1, and 8. IZ: Writing parts of Sec. 4 and reviewing Secs. 2, 3, and 4.

A SIGWAY code: technicalities

In this appendix, we describe some technical aspects of the SIGWAY code developed for the analysis performed in this work.

A.1 Perturbations in USR scenarios: code structure

Given a potential $V(\phi)$ inducing a USR phase, the curvature power spectrum is computed in three steps that are described below. $\mathcal{P}_\zeta(k)$ is then interpolated and $\Omega_{\text{GW}}h^2$ is computed as described in A.2.

Using the notation described in Sec. 3.3, the inputs in the code are:

- the inflaton potential $V(\phi)$;
- the number of e -folds from when CMB modes exit the Hubble horizon to the end of inflation $N_{\text{CMB}\rightarrow\text{end}}$.
- The initial conditions ϕ_0 and $\pi_0 = \phi'_0$.

The code then automatically defines the dimensionless variables in Eq. (3.19). For definiteness, in this paper, we have fixed $N_{\text{CMB}\rightarrow\text{end}} = 58$. Fixing the number of e -folds from the CMB scale to the end of inflation effectively allows us to set the correspondence between N and wavenumbers k . Fixing N_{CMB} also implicitly fixes the thermal history of reheating and subsequent phases. We do not model these eras for simplicity, but they would be fixed in a complete USR+reheating model. Also, we checked that the initial SR attractor would quickly pull the field space trajectory to the background evolution, and thus one could also assume negligible initial velocity for simplicity.

The computation then proceeds as follows:

1. Solve for the the background evolution using Eqs. (3.21). We evolve the dynamics until the first SR condition is violated ($\epsilon_H = 1$), collecting $x(N)$, $y(N)$ and $h(N)$. We denote the number of e -folds at the end of inflation N_{end} .
2. Compute the relation between the wave number k and the number of e -folds N at Hubble crossing using

$$k = k_{\text{CMB}} \frac{h(N)}{h_{\text{CMB}}} \exp(N - N_{\text{CMB}}), \quad (\text{A.1})$$

where $k_{\text{CMB}} = 0.05/\text{Mpc}$, $N_{\text{CMB}} = N_{\text{end}} - N_{\text{CMB}\rightarrow\text{end}}$ and $h_{\text{CMB}} = h(N_{\text{CMB}})$. With this, we can compute $\mathcal{P}_\zeta(k)$ in the SR approximation according to Eq. (3.25).

3. We are only interested in computing the spectrum of curvature perturbations beyond the SR approximation for modes of relevance for LISA. Once we have computed $k(N)$, a set of modes covering the LISA frequency band $\sim (10^{-5} - 10^{-1}) \text{ Hz}$ is selected and those modes are evolved according to Eq. (3.31) from N_{in} to N_{out} , where N_{in} and N_{out} can be set by the user. We found $N_{\text{in}} = N - 3$ and $N_{\text{out}} = N + 7$, where N is the horizon crossing time of the mode, to be long enough for the modes to freeze out

as there is no super horizon evolution in these models once USR has ended. Notice that the USR can only last about $\mathcal{O}(3)$ e -folds without making perturbations grow beyond the validity of perturbation theory. Additionally, for simple shapes of the potential, we find that evolving ~ 100 modes in k and interpolating between them yields sufficient precision.

4. Lastly, $\mathcal{P}_\zeta(k)$ is computed without resorting to the SR approximation using Eq. (3.32). This quantity is then passed to the algorithm computing $\Omega_{\text{GW}}h^2$ which can then be passed to the LISA likelihood.

Fig. 26 shows the evolution of a number of modes in \mathcal{P}_ζ as a function of N across the USR phase. As this algorithm is called many times when sampling the LISA likelihood, we are using the package `diffraX` [412] to solve the inflationary perturbation equation of motion.

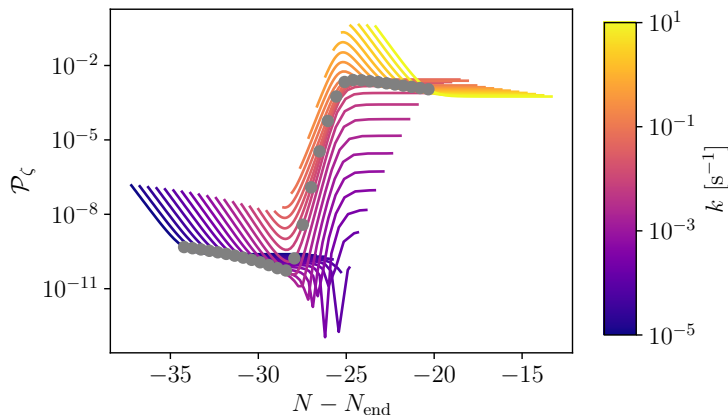


Figure 26. Power spectrum as a function of N for different modes k indicated by the color palette, close to the onset of the USR phase $N - N_{\text{end}} \simeq -28$. This plot shows the evolution and freezing out of modes for different values of k for the potential from Eq. (2.4). The evolution of each mode is traced for around $\Delta N \simeq 10$ e -folds from within the Hubble sphere to sufficiently after Hubble crossing and freezing. The time of Hubble crossing is marked with gray dots.

A.2 Computation of SIGWs from the spectrum of curvature perturbations

For a given shape of $\mathcal{P}_\zeta(k)$, computing $\Omega_{\text{GW}}h^2$ is relatively straightforward by evaluating the double integral in Eq. (4.20). The main concern here is making this computation as fast as possible, as this dominates the time it takes for each likelihood evaluation. To take full advantage of vectorization, we compute s, t, k on a grid, where s is linearly spaced, and t, k are logarithmically spaced. The integration in t is convergent for any realistic shape of \mathcal{P}_ζ as both the value of $\overline{I^2(k, s, t)}$ tends towards 0 for large t and there needs to be some cutoff controlling the amplitude of \mathcal{P}_ζ at large momenta not to violate BBN bounds. If $\mathcal{P}_\zeta(k)$ features a scale after which it drops rapidly, it can be advantageous to define a custom $t(k)$ and compute the grid as $s, t(k), k$.

After evaluating the integrand in Eq. (4.20) on the grid, the integral is computed with Simpson-integration. Depending on the shape of \mathcal{P}_ζ , we found a number of points in the grid around $N_s \sim 10 - 100$, $N_t \sim 300 - 1000$ and $N_k \sim 100$ would give sufficient precision.

To take full advantage of threading, we use JAX and just-in-time compilation [375] for computing the integrand and performing the integration itself. Altogether, this results in a significant speedup over other publicly available codes (e.g. [413]). We record wall-clock times of $\sim 10^{-2}$ s for calculating 100 values of Ω_{GW} for \mathcal{P}_ζ containing only JAX-native functions. In the case discussed in Sec. 6.2.2 this time rises to about 1 s. Crucially, this speedup allows us to sample the posterior distribution efficiently and obtain good MCMC convergence with a laptop on timescales of $\mathcal{O}(\text{hours})$.

A.3 Computation of SIGWs using binned coefficients

In the case where we bin $\mathcal{P}_\zeta(p)$ in momentum space, $\Omega_{\text{GW}}(k)$ can be computed in a straightforward manner through Eq. (4.27). The most computationally expensive part of this is the computation of the coefficients $\Omega_{\text{GW}}^{(i,j)}(k)$. Luckily we can precompute these coefficients on a grid and save them as a $N_k \times N_p \times N_p$ tensor $K_{ij}^k \equiv \Omega_{\text{GW}}^{(i,j)}(k)$. At runtime, we then compute a $N_p \times N_p$ tensor of $B = A \otimes A$, with which we can conveniently re-write Eq. (4.27) as

$$\Omega_{\text{GW}}^k = \Omega_{ij}^k B^{ij}, \quad (\text{A.2})$$

where we used Einstein sum convention. The reason for doing this arguably very simple conversion is that the matrix equation is fully vectorizable with JAX.

Using this trick we are able to compute Ω_{GW} from \mathcal{P}_ζ in $\lesssim 10^{-3}$ s for $N_k = N_p = 50$, thus making inference possible despite a large number of parameters to sample.

A.4 Computation of SIGWs including primordial NGs

In this appendix, we provide additional technical details regarding the MCMC analyses that resulted in Figures 24 and 23, as well as the parameter scan leading to Fig. 22. As reported in Sec. 4.5, the trispectrum arising from the local expansion Eq. (4.37) leads to additional contributions to the SIGW spectrum. In particular, from the connected part, one obtains the following two terms

$$\begin{aligned} \Omega_{\text{GW}}(k, \eta)|_{\text{t}} = & \frac{1}{12\pi} \left(\frac{k}{aH} \right)^2 \left(\frac{3}{5} f_{\text{NL}} \right)^2 \int_0^\infty dt_1 \int_{-1}^1 ds_1 \int_0^\infty dt_2 \int_{-1}^1 ds_2 \\ & \times \int_0^{2\pi} d\varphi_{12} \cos 2\varphi_{12} \frac{u_1 v_1}{(u_2 v_2)^2} \frac{1}{w_{a,12}^3} \overline{\tilde{J}(u_1, v_1, x) \tilde{J}(u_2, v_2, x)} \\ & \times \mathcal{P}_{\zeta_g}(v_2 k) \mathcal{P}_{\zeta_g}(u_2 k) \mathcal{P}_{\zeta_g}(w_{a,12} k), \end{aligned} \quad (\text{A.3})$$

and

$$\begin{aligned}
\Omega_{\text{GW}}(k, \eta)|_{\text{u}} &= \frac{1}{12\pi} \left(\frac{k}{aH} \right)^2 \left(\frac{3}{5} f_{\text{NL}} \right)^2 \int_0^\infty dt_1 \int_{-1}^1 ds_1 \int_0^\infty dt_2 \int_{-1}^1 ds_2 \\
&\times \int_0^{2\pi} d\varphi_{12} \cos 2\varphi_{12} \frac{u_1 u_2}{(v_1 v_2)^2} \frac{1}{w_{b,12}^3} \overline{\tilde{J}(u_1, v_1, x) \tilde{J}(u_2, v_2, x)} \quad (\text{A.4}) \\
&\times \mathcal{P}_{\zeta_g}(v_1 k) \mathcal{P}_{\zeta_g}(v_2 k) \mathcal{P}_{\zeta_g}(w_{b,12} k),
\end{aligned}$$

were the integration variables t_i and s_i are defined as in Eq. (4.19). To keep the equation concise, some terms have been left expressed as functions of u_i and v_i , but they have to be intended as depending on the integration variables t_i and s_i . Moreover, we introduced $\tilde{J}(u_i, v_i, x) = v_i^2 k^2 \sin^2 \theta I(u_i, v_i, x)$, with $I(u, v, x)$ the integration kernel defined in the main text and $w_{a,12}$ and $w_{b,12}$, defined as

$$w_{a,12} = [v_1^2 + v_2^2 - 2v_1 v_2 (\cos \theta_1 \cos \theta_2 + \sin \theta_1 \sin \theta_2 \cos \varphi_{12})]^{1/2}, \quad (\text{A.5})$$

and

$$\begin{aligned}
w_{b,12} &= [1 + v_1^2 + v_2^2 + 2v_1 v_2 (\cos \theta_1 \cos \theta_2 + \sin \theta_1 \sin \theta_2 \cos \varphi_{12}) \\
&\quad - 2v_1 \cos \theta_1 - 2v_2 \cos \theta_2]^{1/2}. \quad (\text{A.6})
\end{aligned}$$

The sine and cosine functions are related to the integration variables by

$$\cos \theta_i = \frac{1 - s_i(1 + t_i)}{t_i - s_i + 1}, \quad \sin^2 \theta_i = \frac{(1 - s_i^2)t_i(2 + t_i)}{(t_i - s_i + 1)^2}. \quad (\text{A.7})$$

As shown in Eqs. (A.3) and (A.4), the evaluation of the NG corrections requires a 5 dimensional integration for each of the frequencies at which the final GW spectrum is evaluated. However, f_{NL} and A_s are multiplicative parameters and the effect of k_* just results in a shift of the spectrum along the k -axis. Hence, once the spectrum is evaluated for a fixed width Δ , it can be used for different values of the parameters reported above, without requiring further evaluation. When Δ is varied, instead, a new evaluation of the spectrum is required each time. Hence, just a single evaluation of the spectrum would require relatively little time, but the evaluation of the whole spectrum for each point of the MCMC would notably slow down the run, making it difficult to get the final posterior in a reasonable time, also considering the presence of other parameters in the MCMC evaluation.

For this reason, to speed up the evaluation we proceed as follows: we numerically pre-compute a grid of NG contributions to the GW spectra as a function of frequency for different widths, in order to explore the range $\log_{10} \Delta \in [-1, 1]$. This grid is then used to obtain the NG corrections to the spectrum corresponding to any value of Δ in the range considered, by interpolating them from the pre-computed ones. In detail, to get the spectrum corresponding to those values of $\bar{\Delta}$ not present in the grid, we first search for Δ_{max} and Δ_{min} , respectively immediately above and below $\bar{\Delta}$. Then we compute the interpolated spectrum by Taylor expanding around these values, obtaining

$$\Omega_{\text{GW}}(\bar{\Delta}) = \Omega_{\text{GW}}(\Delta_{\text{max}})w_{\text{min}} + \Omega_{\text{GW}}(\Delta_{\text{min}})(1 - w_{\text{min}}), \quad (\text{A.8})$$

with

$$w_{\min} = \frac{(\bar{\Delta} - \Delta_{\min})}{(\Delta_{\max} - \Delta_{\min})}. \quad (\text{A.9})$$

For the evaluation of the scans that require a Fisher forecast and hence the derivatives with respect to the parameters, we proceed in a similar way. We pre-compute a grid of derivatives²⁰ in the range $\log_{10} \Delta \in [-1, 1]$ and then we interpolate as explained above.

A.5 Inference

Once Ω_{GW} has been computed by the `SIGWAY`, the resulting spectrum is interpolated in log-space and passed to the `SGWBinner` which computes the posterior distribution according to Eq. (5.21). `Cobaya` [374, 414] is used as an inference-framework. We use different samplers for Monte Carlo sampling depending on the dimensionality, requirements, and structure of the posterior surface:

- The inferences in Figs. 3, 4, 8, 9, 11, 12, and 21 have been run using the nested sampler `nessai` [415–417].
- Figs. 5, 6, 19, 23, and 24 have been obtained using `Cobaya`’s `CosmoMC` [418, 419] MCMC, where we started the chains at the injected values and injected FIM estimates of the covariance matrix to speed up convergence.
- The evidences in Sec. 7 have been computed with the nested sampler `PolyChord` [403, 404]
- The inference for Figs. 14 and 15 was performed using the active learning algorithm `GPry` [420, 421] due to the prohibitively slow speed of computing \mathcal{P}_ζ stemming from the Bessel functions in its equation.

All corner plots have been created with `GetDist` [422]. In the corner plots, we omitted showing the marginalised constraints on A_{noise} and P_{noise} , as in all cases they were well constrained and showed weak degeneracies with the signal parameters. To give an idea of how tightly these parameters tend to be constrained, Fig. 27 shows a corner plot including the constraints on A_{noise} and P_{noise} for the injected lognormal \mathcal{P}_ζ (see Eq. (3.5)).

B Challenges with binned analyses and a large number of bins

The binned approach to performing the double integration going from \mathcal{P}_ζ to Ω_{GW} introduced in Sec. 4.4 – while in principle extremely powerful at reconstructing any SIGW spectrum without model-dependence – unfortunately suffers from some crucial shortcomings as will be explained in this section.

For the sake of illustration, we will only consider the case where all modes reenter during radiation domination (see Sec. 4.2) where the kernel is k -independent. The situation

²⁰Note that when taking the derivative with respect to A_s and f_{NL} the integrals remain unchanged, hence we consider the same pre-computed NG contributions used in the MCMC runs. When taking the derivative with respect to k_* or Δ , instead, since the integrand is varied, we pre-compute a grid for each of these two derivatives.

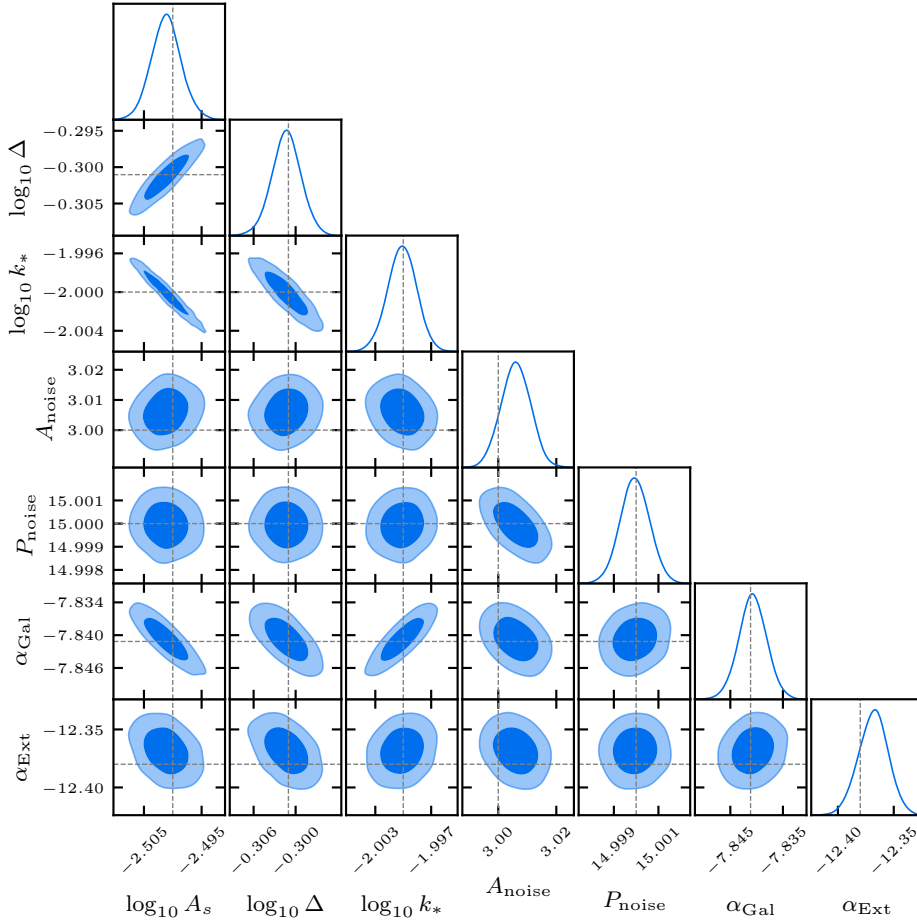


Figure 27. Same as Fig. 5 but showing the marginalised contours for all sampled parameters including the noise parameters $A_{\text{noise}}, P_{\text{noise}}$. There is a relatively mild degeneracy between A_{noise} and α_{Gal} but no correlations between the signal parameters A_s, Δ, k_* and the noise parameters. We found similar correlations (or the lack thereof) for all other injections.

changes a bit if the kernel has a k -dependence such as is the case during an early matter domination era (see Sec. 4.3), however, our main arguments remain unchanged.

It is clear from the structure of the integral in Eq. (4.20), that a single wavenumber k in \mathcal{P}_ζ affects multiple frequencies in Ω_{GW} . An easy way to understand this is to consider a \mathcal{P}_ζ that is sufficiently close to a monochromatic source $\mathcal{P}_\zeta(k) = A_s \delta(k - k_*)$. In our binned approach this translates to one single bin A_* being non-zero. Fig. 28 shows three such spectra with 100 bins, where each one contains a single non-zero bin A_* (bin nr. 85, 86, 87 in this case). It is evident from this figure that if the peak towards k_* is not resolved, and only the causality tail in the IR regime enters the LISA sensitivity, these spectra become entirely degenerate. This means that there is not necessarily a unique mapping $\Omega_{\text{GW}} \mapsto \mathcal{P}_\zeta$. In other words, the power from the bins is “leaking” into adjacent bins.

In reality, this means that, for many bins and towards low SNR, the binned recon-

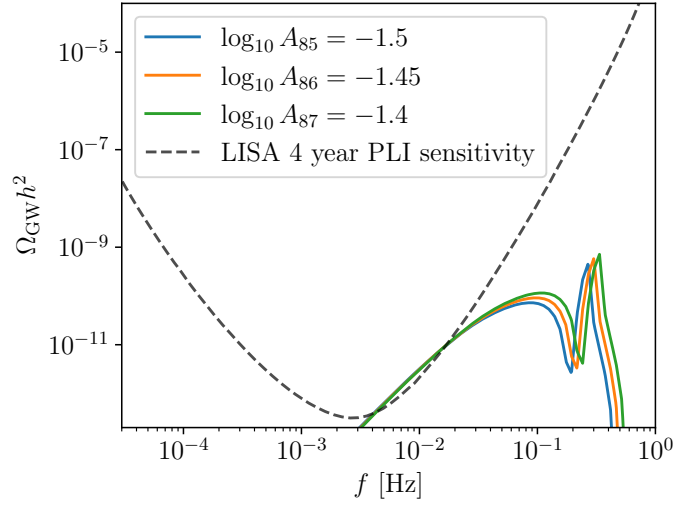


Figure 28. Three different spectra in Ω_{GW} generated with the binned approach with 100 bins where for each spectrum only one of the bins is non-zero. The black dashed line shows the approximate power law integrated sensitivity of LISA assuming a 4-year mission. It is clear from this picture that the three adjacent bins shown are entirely degenerate when trying to resolve them with LISA as the peaks are well outside the sensitivity and the causality tails generated are exactly the same.

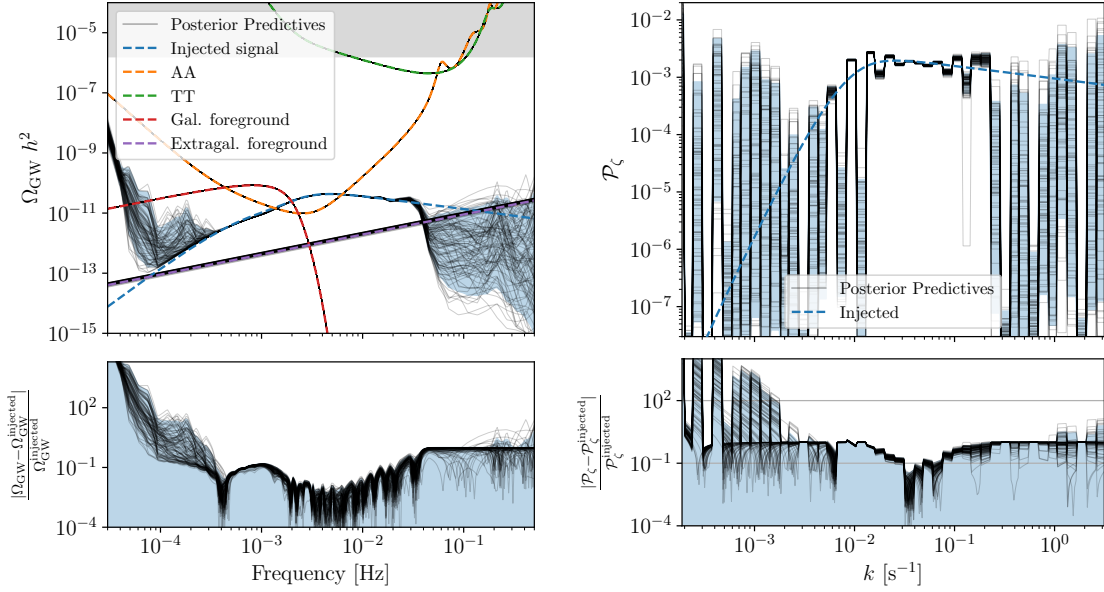


Figure 29. Same as Fig. 3, but for an injected BPL spectrum following the benchmark USR model and using 50 bins.

structed \mathcal{P}_ζ is highly degenerate, and valid reconstructions include “oscillations” between the bins as lower power in one bin can be compensated by higher power in an adjacent one.

The aforementioned degeneracies are not unexpected and are really just a feature of the physical properties of the process of scalar-induced gravitational waves. However, they

do induce some practical complications. In an ideal template-agnostic pipeline, we would want to perform inference on the N_{bins} bins in \mathcal{P}_ζ to reconstruct the signal with the highest evidence parameterization. Due to the large (non-linear) degeneracies between the bins, the likelihood is far from Gaussian and the FIM approximation is invalid, making MC-sampling necessary. Sampling over this space is very computationally challenging due to (a) the very narrow degeneracies (b) the resulting large number of posterior modes and (c) the high dimensionality of the parameter space. In practice, this leads to overconfidence in the reconstruction, as some posterior modes are inevitably missed or underexplored by the MC sampler. Fig. 29 shows the binned reconstruction of the USR model injection from Sec. 2.4 with 50 bins. The oscillation effect is clearly visible in the low SNR region, where \mathcal{P}_ζ oscillates between high power and low power, thus overconstraining certain bins. These degeneracies are partially broken by fewer bins, as visible in Fig. 3.

This leaves us in a dilemma: we would like to bin \mathcal{P}_ζ as finely as possible to increase the frequency resolution of the template, but as one increases N_{bins} the posterior becomes much more difficult to sample. In our tests, we found $N_{\text{bins}} = 15$ to be reliable in terms of convergence for the BPL signal (Fig. 3) and $N_{\text{bins}} = 40$ for the injected lognormal signals in Ω_{GW} and \mathcal{P}_ζ (Fig. 25) that occupy less of the frequency range. However, it is clear that this low number of bins cannot reconstruct the shape of \mathcal{P}_ζ with high fidelity.

Luckily, this problem does not appear when no signal is present, as the posterior distribution in A_i becomes a simple upper bound, an unimodal structure that is easy to map by a nested sampler, even in high dimensions. We can therefore conclude that the upper bounds obtained by this method are reliable even with many bins.

Future work on this approach could include studying improved bases for the reconstructed bins (a basis of Gaussians or other wide kernels in \mathcal{P}_ζ may be less multi-modal), or improving sampling by manually adding jump proposals to the degenerate modes of the posterior in a given basis (e.g. as is done for LISA black hole binary sampling in BBHx [56]).

C Testing the resolvability of Non-Gaussian corrections: Additional plots

Fig. 30 shows a corner plot that was obtained by injecting a purely Gaussian SIGW signal with a lognormal shape in \mathcal{P}_ζ (see Eq. (3.5)) that is equivalent to the cases discussed in Figs. 23 and 24 with $f_{\text{NL}} = \tau_{\text{NL}} = 0$. The remaining injected parameters are the same as in Section 6.5: $\log_{10} A_s = -2$, $\log_{10} \Delta = -0.75$, $\log_{10}(k_*/\text{s}^{-1}) = -2.3$. By comparing these results to the one obtained for $f_{\text{NL}} = 1$ shown in Fig. 23 and $f_{\text{NL}} = 10$ shown in Fig. 24, we see that the NG contribution neither significantly improves, nor worsens the constraints on the signal and foreground parameters.

D Testing the scalar-induced hypothesis: Additional plots

Figure 31 provides further insight into the quality of reconstruction when comparing the **SGWBinner** and the **SIGWAY** methods. The noise is accurately reconstructed in all cases, with only a slight underestimation in case 1 (left panel) using the **SIGWAY** template recon-

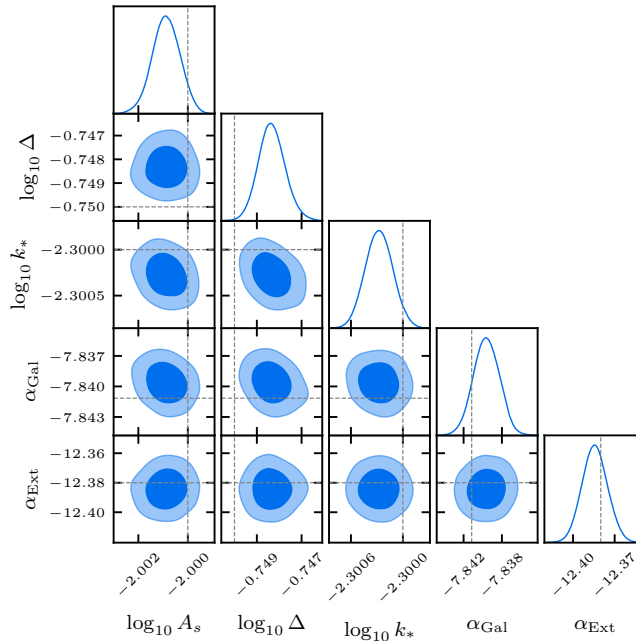


Figure 30. Same as Fig. 5 for the same injected parameters as in Sec. 6.5.

struction. In contrast, the extragalactic background is reconstructed less accurately with the **SGWBinner** compared to the other methods.

A particularly notable observation is that in case 1 (left column), the **SIGWAY** template method significantly underestimates both the extragalactic and galactic foregrounds. This underestimation can be attributed to the model compensating for excess power in the causality tail by reducing the power allocated to the foregrounds, due to the limited flexibility in the shape of Ω_{GW} provided by the template. Interestingly, in case 2 (right column), the **SIGWAY** method – using the template or not – performs better than the **SGWBinner** in reconstructing the foregrounds. This improvement arises because the assumption of SIGWs enforces a specific shape for Ω_{GW} , which cannot be easily mimicked by the foregrounds. In contrast, the **SGWBinner** does not impose such restrictions during reconstruction. This result stresses the importance of adopting optimal modeling of the eventual cosmological signal even when reconstructing the astrophysical properties of the foreground sources.

References

- [1] LISA collaboration, *Laser Interferometer Space Antenna*, [1702.00786](#).
- [2] LISA COSMOLOGY WORKING GROUP collaboration, *Cosmology with the Laser Interferometer Space Antenna*, *Living Rev. Rel.* **26** (2023) 5 [[2204.05434](#)].
- [3] LISA collaboration, *New horizons for fundamental physics with LISA*, *Living Rev. Rel.* **25** (2022) 4 [[2205.01597](#)].

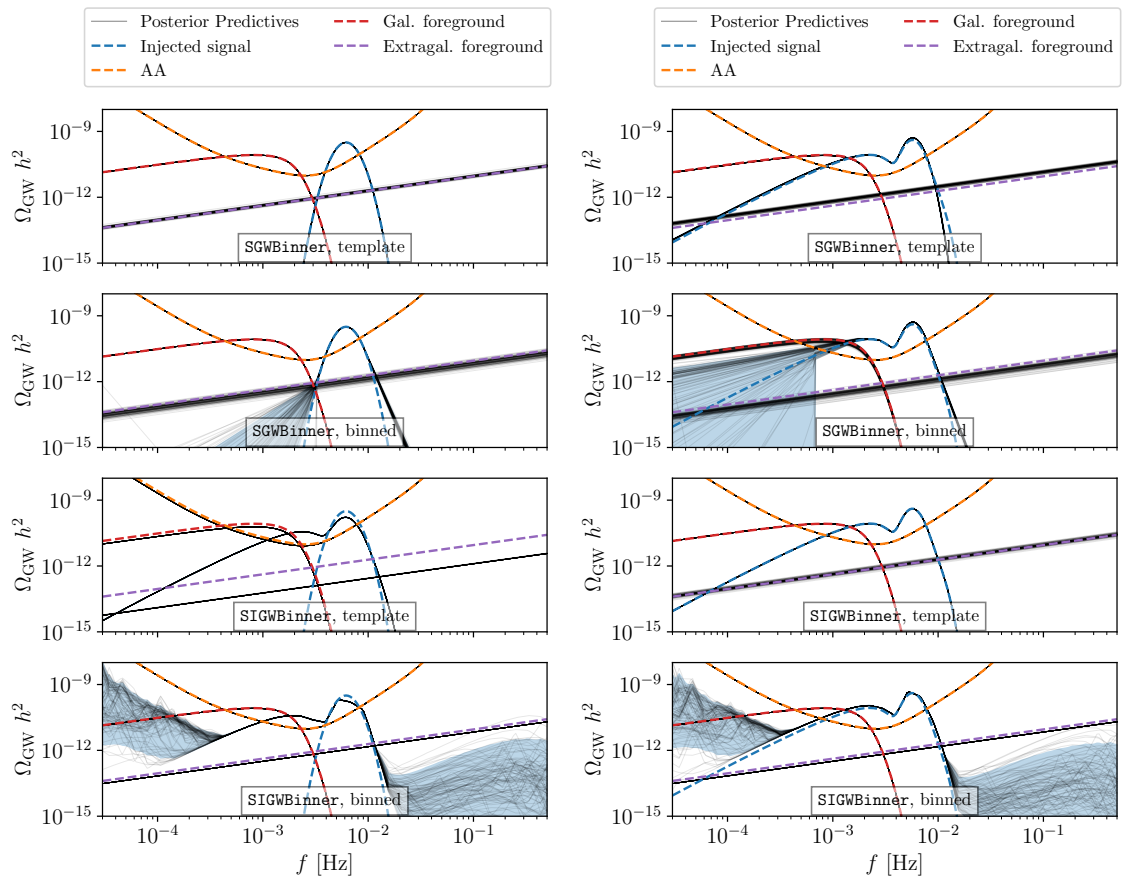


Figure 31. Reconstruction of Ω_{GW} for case 1 (left) and case 2 (right) including the noise and foreground. See Sec. 7 for more details. The TT-channel component of the noise is above 10^{-7} and we therefore omit it. We denote the wrapper to perform the analysis using SIGWAY as SIGWBinner in this plot.

- [4] LISA collaboration, *Astrophysics with the Laser Interferometer Space Antenna*, *Living Rev. Rel.* **26** (2023) 2 [2203.06016].
- [5] N. Bartolo et al., *Science with the space-based interferometer LISA. IV: Probing inflation with gravitational waves*, *JCAP* **12** (2016) 026 [1610.06481].
- [6] LISA COSMOLOGY WORKING GROUP collaboration, *Gravitational waves from inflation in LISA: reconstruction pipeline and physics interpretation*, *JCAP* **11** (2024) 032 [2407.04356].
- [7] M. Maggiore, *Gravitational Waves. Vol. 1: Theory and Experiments*. Oxford University Press, 2007, 10.1093/acprof:oso/9780198570745.001.0001.
- [8] M. C. Guzzetti, N. Bartolo, M. Liguori and S. Matarrese, *Gravitational waves from inflation*, *Riv. Nuovo Cim.* **39** (2016) 399 [1605.01615].
- [9] R.-G. Cai, Z. Cao, Z.-K. Guo, S.-J. Wang and T. Yang, *The Gravitational-Wave Physics*, *Natl. Sci. Rev.* **4** (2017) 687 [1703.00187].
- [10] C. Caprini and D. G. Figueroa, *Cosmological Backgrounds of Gravitational Waves*, *Class.*

- Quant. Grav.* **35** (2018) 163001 [[1801.04268](#)].
- [11] K. Tomita, *Evolution of Irregularities in a Chaotic Early Universe*, *Prog. Theor. Phys.* **54** (1975) 730.
- [12] S. Matarrese, O. Pantano and D. Saez, *A General relativistic approach to the nonlinear evolution of collisionless matter*, *Phys. Rev. D* **47** (1993) 1311.
- [13] S. Matarrese, O. Pantano and D. Saez, *General relativistic dynamics of irrotational dust: Cosmological implications*, *Phys. Rev. Lett.* **72** (1994) 320 [[astro-ph/9310036](#)].
- [14] S. Matarrese, S. Mollerach and M. Bruni, *Second order perturbations of the Einstein-de Sitter universe*, *Phys. Rev. D* **58** (1998) 043504 [[astro-ph/9707278](#)].
- [15] V. Acquaviva, N. Bartolo, S. Matarrese and A. Riotto, *Second order cosmological perturbations from inflation*, *Nucl. Phys. B* **667** (2003) 119 [[astro-ph/0209156](#)].
- [16] S. Mollerach, D. Harari and S. Matarrese, *CMB polarization from secondary vector and tensor modes*, *Phys. Rev. D* **69** (2004) 063002 [[astro-ph/0310711](#)].
- [17] C. Carbone and S. Matarrese, *A Unified treatment of cosmological perturbations from super-horizon to small scales*, *Phys. Rev. D* **71** (2005) 043508 [[astro-ph/0407611](#)].
- [18] K. N. Ananda, C. Clarkson and D. Wands, *The Cosmological gravitational wave background from primordial density perturbations*, *Phys. Rev. D* **75** (2007) 123518 [[gr-qc/0612013](#)].
- [19] D. Baumann, P. J. Steinhardt, K. Takahashi and K. Ichiki, *Gravitational Wave Spectrum Induced by Primordial Scalar Perturbations*, *Phys. Rev. D* **76** (2007) 084019 [[hep-th/0703290](#)].
- [20] G. Domènech, *Scalar Induced Gravitational Waves Review*, *Universe* **7** (2021) 398 [[2109.01398](#)].
- [21] Y. B. Zel'dovich and I. D. Novikov, *The Hypothesis of Cores Retarded during Expansion and the Hot Cosmological Model*, *Sov. Astron.* **10** (1967) 602.
- [22] S. Hawking, *Gravitationally collapsed objects of very low mass*, *Mon. Not. Roy. Astron. Soc.* **152** (1971) 75.
- [23] B. J. Carr and S. W. Hawking, *Black holes in the early Universe*, *Mon. Not. Roy. Astron. Soc.* **168** (1974) 399.
- [24] B. J. Carr, *The Primordial black hole mass spectrum*, *Astrophys. J.* **201** (1975) 1.
- [25] G. F. Chapline, *Cosmological effects of primordial black holes*, *Nature* **253** (1975) 251.
- [26] N. Bartolo, V. De Luca, G. Franciolini, A. Lewis, M. Peloso and A. Riotto, *Primordial Black Hole Dark Matter: LISA Serendipity*, *Phys. Rev. Lett.* **122** (2019) 211301 [[1810.12218](#)].
- [27] N. Bartolo, V. De Luca, G. Franciolini, M. Peloso, D. Racco and A. Riotto, *Testing primordial black holes as dark matter with LISA*, *Phys. Rev. D* **99** (2019) 103521 [[1810.12224](#)].
- [28] LISA COSMOLOGY WORKING GROUP collaboration, *Primordial black holes and their gravitational-wave signatures*, [2310.19857](#).
- [29] A. Gangui, F. Lucchin, S. Matarrese and S. Mollerach, *The Three point correlation function of the cosmic microwave background in inflationary models*, *Astrophys. J.* **430** (1994) 447 [[astro-ph/9312033](#)].

- [30] S. Matarrese, L. Verde and R. Jimenez, *The Abundance of high-redshift objects as a probe of non-Gaussian initial conditions*, *Astrophys. J.* **541** (2000) 10 [[astro-ph/0001366](#)].
- [31] N. Bartolo, S. Matarrese and A. Riotto, *Nongaussianity from inflation*, *Phys. Rev. D* **65** (2002) 103505 [[hep-ph/0112261](#)].
- [32] J. M. Maldacena, *Non-Gaussian features of primordial fluctuations in single field inflationary models*, *JHEP* **05** (2003) 013 [[astro-ph/0210603](#)].
- [33] N. Bartolo, E. Komatsu, S. Matarrese and A. Riotto, *Non-Gaussianity from inflation: Theory and observations*, *Phys. Rept.* **402** (2004) 103 [[astro-ph/0406398](#)].
- [34] X. Chen, *Primordial Non-Gaussianities from Inflation Models*, *Adv. Astron.* **2010** (2010) 638979 [[1002.1416](#)].
- [35] C. T. Byrnes and K.-Y. Choi, *Review of local non-Gaussianity from multi-field inflation*, *Adv. Astron.* **2010** (2010) 724525 [[1002.3110](#)].
- [36] D. Wands, *Local non-Gaussianity from inflation*, *Class. Quant. Grav.* **27** (2010) 124002 [[1004.0818](#)].
- [37] S. Renaux-Petel, *Primordial non-Gaussianities after Planck 2015: an introductory review*, *Comptes Rendus Physique* **16** (2015) 969 [[1508.06740](#)].
- [38] A. Achúcarro et al., *Inflation: Theory and Observations*, [2203.08128](#).
- [39] T. Nakama, J. Silk and M. Kamionkowski, *Stochastic gravitational waves associated with the formation of primordial black holes*, *Phys. Rev. D* **95** (2017) 043511 [[1612.06264](#)].
- [40] J. Garcia-Bellido, M. Peloso and C. Unal, *Gravitational Wave signatures of inflationary models from Primordial Black Hole Dark Matter*, *JCAP* **09** (2017) 013 [[1707.02441](#)].
- [41] C. Unal, *Imprints of Primordial Non-Gaussianity on Gravitational Wave Spectrum*, *Phys. Rev. D* **99** (2019) 041301 [[1811.09151](#)].
- [42] R.-g. Cai, S. Pi and M. Sasaki, *Gravitational Waves Induced by non-Gaussian Scalar Perturbations*, *Phys. Rev. Lett.* **122** (2019) 201101 [[1810.11000](#)].
- [43] R.-G. Cai, S. Pi, S.-J. Wang and X.-Y. Yang, *Resonant multiple peaks in the induced gravitational waves*, *JCAP* **05** (2019) 013 [[1901.10152](#)].
- [44] H. V. Ragavendra, P. Saha, L. Sriramkumar and J. Silk, *Primordial black holes and secondary gravitational waves from ultraslow roll and punctuated inflation*, *Phys. Rev. D* **103** (2021) 083510 [[2008.12202](#)].
- [45] C. Yuan and Q.-G. Huang, *Gravitational waves induced by the local-type non-Gaussian curvature perturbations*, *Phys. Lett. B* **821** (2021) 136606 [[2007.10686](#)].
- [46] P. Adshead, K. D. Lozanov and Z. J. Weiner, *Non-Gaussianity and the induced gravitational wave background*, *JCAP* **10** (2021) 080 [[2105.01659](#)].
- [47] M. W. Davies, P. Carrilho and D. J. Mulryne, *Non-Gaussianity in inflationary scenarios for primordial black holes*, *JCAP* **06** (2022) 019 [[2110.08189](#)].
- [48] K. T. Abe, R. Inui, Y. Tada and S. Yokoyama, *Primordial black holes and gravitational waves induced by exponential-tailed perturbations*, *JCAP* **05** (2023) 044 [[2209.13891](#)].
- [49] S. Garcia-Saenz, L. Pinol, S. Renaux-Petel and D. Werth, *No-go theorem for scalar-trispectrum-induced gravitational waves*, *JCAP* **03** (2023) 057 [[2207.14267](#)].

- [50] S. Garcia-Saenz, Y. Lu and Z. Shuai, *Scalar-induced gravitational waves from ghost inflation and parity violation*, *Phys. Rev. D* **108** (2023) 123507 [2306.09052].
- [51] J.-P. Li, S. Wang, Z.-C. Zhao and K. Kohri, *Complete analysis of the background and anisotropies of scalar-induced gravitational waves: primordial non-Gaussianity f_{NL} and g_{NL} considered*, *JCAP* **06** (2024) 039 [2309.07792].
- [52] C. Yuan, D.-S. Meng and Q.-G. Huang, *Full analysis of the scalar-induced gravitational waves for the curvature perturbation with local-type non-Gaussianities*, *JCAP* **12** (2023) 036 [2308.07155].
- [53] G. Perna, C. Testini, A. Ricciardone and S. Matarrese, *Fully non-Gaussian Scalar-Induced Gravitational Waves*, *JCAP* **05** (2024) 086 [2403.06962].
- [54] M. Colpi et al., *LISA Definition Study Report*, 2402.07571.
- [55] T. B. Littenberg and N. J. Cornish, *Prototype global analysis of LISA data with multiple source types*, *Phys. Rev. D* **107** (2023) 063004 [2301.03673].
- [56] M. L. Katz, N. Karnesis, N. Korsakova, J. R. Gair and N. Stergioulas, *An efficient GPU-accelerated multi-source global fit pipeline for LISA data analysis*, 2405.04690.
- [57] S. H. Strub, L. Ferraioli, C. Schmelzbach, S. C. Stähler and D. Giardini, *Global analysis of LISA data with Galactic binaries and massive black hole binaries*, *Phys. Rev. D* **110** (2024) 024005 [2403.15318].
- [58] M. Le Jeune and S. Babak, *Lisa data challenge sangria (ldc2a)*, Oct., 2022. 10.5281/zenodo.7132178.
- [59] R. Rosati and T. B. Littenberg, *Prototype Stochastic Gravitational Wave Background Recovery in the LISA Global Fit Residual*, 2410.17180.
- [60] N. Karnesis, M. Lilley and A. Petiteau, *Assessing the detectability of a Stochastic Gravitational Wave Background with LISA, using an excess of power approach*, *Class. Quant. Grav.* **37** (2020) 215017 [1906.09027].
- [61] C. Caprini, D. G. Figueroa, R. Flauger, G. Nardini, M. Peloso, M. Pieroni et al., *Reconstructing the spectral shape of a stochastic gravitational wave background with LISA*, *JCAP* **11** (2019) 017 [1906.09244].
- [62] R. Flauger, N. Karnesis, G. Nardini, M. Pieroni, A. Ricciardone and J. Torrado, *Improved reconstruction of a stochastic gravitational wave background with LISA*, *JCAP* **01** (2021) 059 [2009.11845].
- [63] M. Pieroni and E. Barausse, *Foreground cleaning and template-free stochastic background extraction for LISA*, *JCAP* **07** (2020) 021 [2004.01135].
- [64] Q. Baghi, N. Karnesis, J.-B. Bayle, M. Besançon and H. Inchauspé, *Uncovering gravitational-wave backgrounds from noises of unknown shape with LISA*, *JCAP* **04** (2023) 066 [2302.12573].
- [65] F. Pozzoli, R. Buscicchio, C. J. Moore, F. Haardt and A. Sesana, *Weakly parametric approach to stochastic background inference in LISA*, *Phys. Rev. D* **109** (2024) 083029 [2311.12111].
- [66] A. Dimitriou, D. G. Figueroa and B. Zaldivar, *Fast likelihood-free reconstruction of gravitational wave backgrounds*, *JCAP* **09** (2024) 032 [2309.08430].

- [67] LISA COSMOLOGY WORKING GROUP collaboration, *Gravitational waves from inflation in LISA: reconstruction pipeline and physics interpretation*, *JCAP* **11** (2024) 032 [[2407.04356](#)].
- [68] A. J. Iovino, S. Matarrese, G. Perna, A. Ricciardone and A. Riotto, *How Well Do We Know the Scalar-Induced Gravitational Waves?*, [2412.06764](#).
- [69] A. A. Starobinsky, *A New Type of Isotropic Cosmological Models Without Singularity*, *Phys. Lett. B* **91** (1980) 99.
- [70] A. H. Guth, *The Inflationary Universe: A Possible Solution to the Horizon and Flatness Problems*, *Phys. Rev. D* **23** (1981) 347.
- [71] A. D. Linde, *A New Inflationary Universe Scenario: A Possible Solution of the Horizon, Flatness, Homogeneity, Isotropy and Primordial Monopole Problems*, *Phys. Lett. B* **108** (1982) 389.
- [72] A. Albrecht and P. J. Steinhardt, *Cosmology for Grand Unified Theories with Radiatively Induced Symmetry Breaking*, *Phys. Rev. Lett.* **48** (1982) 1220.
- [73] PLANCK collaboration, *Planck 2018 results. X. Constraints on inflation*, *Astron. Astrophys.* **641** (2020) A10 [[1807.06211](#)].
- [74] P. Ivanov, P. Naselsky and I. Novikov, *Inflation and primordial black holes as dark matter*, *Phys. Rev. D* **50** (1994) 7173.
- [75] W. H. Kinney, *A Hamilton-Jacobi approach to nonslow roll inflation*, *Phys. Rev. D* **56** (1997) 2002 [[hep-ph/9702427](#)].
- [76] S. Inoue and J. Yokoyama, *Curvature perturbation at the local extremum of the inflaton's potential*, *Phys. Lett. B* **524** (2002) 15 [[hep-ph/0104083](#)].
- [77] W. H. Kinney, *Horizon crossing and inflation with large eta*, *Phys. Rev. D* **72** (2005) 023515 [[gr-qc/0503017](#)].
- [78] J. Martin, H. Motohashi and T. Suyama, *Ultra Slow-Roll Inflation and the non-Gaussianity Consistency Relation*, *Phys. Rev. D* **87** (2013) 023514 [[1211.0083](#)].
- [79] H. Motohashi and W. Hu, *Primordial Black Holes and Slow-Roll Violation*, *Phys. Rev. D* **96** (2017) 063503 [[1706.06784](#)].
- [80] O. Özsoy and G. Tasinato, *On the slope of the curvature power spectrum in non-attractor inflation*, *JCAP* **04** (2020) 048 [[1912.01061](#)].
- [81] A. Karam, N. Koivunen, E. Tomberg, V. Vaskonen and H. Veermäe, *Anatomy of single-field inflationary models for primordial black holes*, *JCAP* **03** (2023) 013 [[2205.13540](#)].
- [82] J. Garcia-Bellido and E. Ruiz Morales, *Primordial black holes from single field models of inflation*, *Phys. Dark Univ.* **18** (2017) 47 [[1702.03901](#)].
- [83] K. Kannike, L. Marzola, M. Raidal and H. Veermäe, *Single Field Double Inflation and Primordial Black Holes*, *JCAP* **09** (2017) 020 [[1705.06225](#)].
- [84] G. Ballesteros and M. Taoso, *Primordial black hole dark matter from single field inflation*, *Phys. Rev. D* **97** (2018) 023501 [[1709.05565](#)].
- [85] C. Germani and T. Prokopec, *On primordial black holes from an inflection point*, *Phys. Dark Univ.* **18** (2017) 6 [[1706.04226](#)].

- [86] J. M. Ezquiaga, J. Garcia-Bellido and E. Ruiz Morales, *Primordial Black Hole production in Critical Higgs Inflation*, *Phys. Lett. B* **776** (2018) 345 [[1705.04861](#)].
- [87] H. Di and Y. Gong, *Primordial black holes and second order gravitational waves from ultra-slow-roll inflation*, *JCAP* **07** (2018) 007 [[1707.09578](#)].
- [88] M. P. Hertzberg and M. Yamada, *Primordial Black Holes from Polynomial Potentials in Single Field Inflation*, *Phys. Rev. D* **97** (2018) 083509 [[1712.09750](#)].
- [89] S. Rasanen and E. Tomberg, *Planck scale black hole dark matter from Higgs inflation*, *JCAP* **01** (2019) 038 [[1810.12608](#)].
- [90] M. Cicoli, V. A. Diaz and F. G. Pedro, *Primordial Black Holes from String Inflation*, *JCAP* **06** (2018) 034 [[1803.02837](#)].
- [91] O. Özsoy, S. Parameswaran, G. Tasinato and I. Zavala, *Mechanisms for Primordial Black Hole Production in String Theory*, *JCAP* **07** (2018) 005 [[1803.07626](#)].
- [92] T.-J. Gao and Z.-K. Guo, *Primordial Black Hole Production in Inflationary Models of Supergravity with a Single Chiral Superfield*, *Phys. Rev. D* **98** (2018) 063526 [[1806.09320](#)].
- [93] V. Atal, J. Garriga and A. Marcos-Caballero, *Primordial black hole formation with non-Gaussian curvature perturbations*, *JCAP* **09** (2019) 073 [[1905.13202](#)].
- [94] V. Atal, J. Cid, A. Escrivà and J. Garriga, *PBH in single field inflation: the effect of shape dispersion and non-Gaussianities*, *JCAP* **05** (2020) 022 [[1908.11357](#)].
- [95] S. S. Mishra and V. Sahni, *Primordial Black Holes from a tiny bump/dip in the Inflaton potential*, *JCAP* **04** (2020) 007 [[1911.00057](#)].
- [96] G. Ballesteros, J. Rey and F. Rompineve, *Detuning primordial black hole dark matter with early matter domination and axion monodromy*, *JCAP* **06** (2020) 014 [[1912.01638](#)].
- [97] I. Dalianis, A. Kehagias and G. Tringas, *Primordial black holes from α -attractors*, *JCAP* **01** (2019) 037 [[1805.09483](#)].
- [98] N. Bhaumik and R. K. Jain, *Primordial black holes dark matter from inflection point models of inflation and the effects of reheating*, *JCAP* **01** (2020) 037 [[1907.04125](#)].
- [99] M. Drees and Y. Xu, *Overshooting, Critical Higgs Inflation and Second Order Gravitational Wave Signatures*, *Eur. Phys. J. C* **81** (2021) 182 [[1905.13581](#)].
- [100] I. Dalianis and G. Tringas, *Primordial black hole remnants as dark matter produced in thermal, matter, and runaway-quintessence postinflationary scenarios*, *Phys. Rev. D* **100** (2019) 083512 [[1905.01741](#)].
- [101] G. Ballesteros, J. Rey, M. Taoso and A. Urbano, *Primordial black holes as dark matter and gravitational waves from single-field polynomial inflation*, *JCAP* **07** (2020) 025 [[2001.08220](#)].
- [102] D. V. Nanopoulos, V. C. Spanos and I. D. Stamou, *Primordial Black Holes from No-Scale Supergravity*, *Phys. Rev. D* **102** (2020) 083536 [[2008.01457](#)].
- [103] L. Iacconi, H. Assadullahi, M. Fasiello and D. Wands, *Revisiting small-scale fluctuations in α -attractor models of inflation*, *JCAP* **06** (2022) 007 [[2112.05092](#)].
- [104] I. D. Stamou, *Mechanisms of producing primordial black holes by breaking the $SU(2,1)/SU(2) \times U(1)$ symmetry*, *Phys. Rev. D* **103** (2021) 083512 [[2104.08654](#)].

- [105] L. Wu, Y. Gong and T. Li, *Primordial black holes and secondary gravitational waves from string inspired general no-scale supergravity*, *Phys. Rev. D* **104** (2021) 123544 [2105.07694].
- [106] K.-W. Ng and Y.-P. Wu, *Constant-rate inflation: primordial black holes from conformal weight transitions*, *JHEP* **11** (2021) 076 [2102.05620].
- [107] K. Rezazadeh, Z. Teimoori, S. Karimi and K. Karami, *Non-Gaussianity and secondary gravitational waves from primordial black holes production in α -attractor inflation*, *Eur. Phys. J. C* **82** (2022) 758 [2110.01482].
- [108] Q. Wang, Y.-C. Liu, B.-Y. Su and N. Li, *Primordial black holes from the perturbations in the inflaton potential in peak theory*, *Phys. Rev. D* **104** (2021) 083546 [2111.10028].
- [109] B.-M. Gu, F.-W. Shu, K. Yang and Y.-P. Zhang, *Primordial black holes from an inflationary potential valley*, *Phys. Rev. D* **107** (2023) 023519 [2207.09968].
- [110] D. Frolovsky, S. V. Ketov and S. Saburov, *E-models of inflation and primordial black holes*, *Front. in Phys.* **10** (2022) 1005333 [2207.11878].
- [111] M. Cicoli, F. G. Pedro and N. Pedron, *Secondary GWs and PBHs in string inflation: formation and detectability*, *JCAP* **08** (2022) 030 [2203.00021].
- [112] A. Ghoshal, A. Moursy and Q. Shafi, *Cosmological probes of grand unification: Primordial black holes and scalar-induced gravitational waves*, *Phys. Rev. D* **108** (2023) 055039 [2306.04002].
- [113] Y.-F. Cai, X.-H. Ma, M. Sasaki, D.-G. Wang and Z. Zhou, *One small step for an inflaton, one giant leap for inflation: A novel non-Gaussian tail and primordial black holes*, *Phys. Lett. B* **834** (2022) 137461 [2112.13836].
- [114] K. Inomata, E. McDonough and W. Hu, *Amplification of primordial perturbations from the rise or fall of the inflaton*, *JCAP* **02** (2022) 031 [2110.14641].
- [115] K. Inomata, E. McDonough and W. Hu, *Primordial black holes arise when the inflaton falls*, *Phys. Rev. D* **104** (2021) 123553 [2104.03972].
- [116] K. Kefala, G. P. Kodaxis, I. D. Stamou and N. Tetradis, *Features of the inflaton potential and the power spectrum of cosmological perturbations*, *Phys. Rev. D* **104** (2021) 023506 [2010.12483].
- [117] I. Dalianis, G. P. Kodaxis, I. D. Stamou, N. Tetradis and A. Tsigkas-Kouvelis, *Spectrum oscillations from features in the potential of single-field inflation*, *Phys. Rev. D* **104** (2021) 103510 [2106.02467].
- [118] J. Yokoyama, *Chaotic new inflation and formation of primordial black holes*, *Phys. Rev. D* **58** (1998) 083510 [astro-ph/9802357].
- [119] R. Saito, J. Yokoyama and R. Nagata, *Single-field inflation, anomalous enhancement of superhorizon fluctuations, and non-Gaussianity in primordial black hole formation*, *JCAP* **06** (2008) 024 [0804.3470].
- [120] E. Bugaev and P. Klimai, *Large curvature perturbations near horizon crossing in single-field inflation models*, *Phys. Rev. D* **78** (2008) 063515 [0806.4541].
- [121] C. Fu, P. Wu and H. Yu, *Primordial black holes and oscillating gravitational waves in slow-roll and slow-climb inflation with an intermediate noninflationary phase*, *Phys. Rev. D* **102** (2020) 043527 [2006.03768].
- [122] V. Briaud and V. Vennin, *Uphill inflation*, *JCAP* **06** (2023) 029 [2301.09336].

- [123] A. Karam, N. Koivunen, E. Tomberg, A. Racioppi and H. Veermäe, *Primordial black holes and inflation from double-well potentials*, *JCAP* **09** (2023) 002 [2305.09630].
- [124] R.-G. Cai, Z.-K. Guo, J. Liu, L. Liu and X.-Y. Yang, *Primordial black holes and gravitational waves from parametric amplification of curvature perturbations*, *JCAP* **06** (2020) 013 [1912.10437].
- [125] G. Tasinato, *An analytic approach to non-slow-roll inflation*, *Phys. Rev. D* **103** (2021) 023535 [2012.02518].
- [126] Z. Zhou, J. Jiang, Y.-F. Cai, M. Sasaki and S. Pi, *Primordial black holes and gravitational waves from resonant amplification during inflation*, *Phys. Rev. D* **102** (2020) 103527 [2010.03537].
- [127] Z.-Z. Peng, C. Fu, J. Liu, Z.-K. Guo and R.-G. Cai, *Gravitational waves from resonant amplification of curvature perturbations during inflation*, *JCAP* **10** (2021) 050 [2106.11816].
- [128] K. Inomata, M. Braglia, X. Chen and S. Renaux-Petel, *Questions on calculation of primordial power spectrum with large spikes: the resonance model case*, *JCAP* **04** (2023) 011 [2211.02586].
- [129] J. Fumagalli, S. Bhattacharya, M. Peloso, S. Renaux-Petel and L. T. Witkowski, *One-loop infrared rescattering by enhanced scalar fluctuations during inflation*, *JCAP* **04** (2024) 029 [2307.08358].
- [130] A. Caravano, K. Inomata and S. Renaux-Petel, *Inflationary Butterfly Effect: Nonperturbative Dynamics from Small-Scale Features*, *Phys. Rev. Lett.* **133** (2024) 151001 [2403.12811].
- [131] D. Frolovsky, S. V. Ketov and S. Saburov, *Formation of primordial black holes after Starobinsky inflation*, *Mod. Phys. Lett. A* **37** (2022) 2250135 [2205.00603].
- [132] G. Ballesteros, J. Beltran Jimenez and M. Pieroni, *Black hole formation from a general quadratic action for inflationary primordial fluctuations*, *JCAP* **06** (2019) 016 [1811.03065].
- [133] C. Fu, P. Wu and H. Yu, *Primordial Black Holes from Inflation with Nonminimal Derivative Coupling*, *Phys. Rev. D* **100** (2019) 063532 [1907.05042].
- [134] C. Fu, P. Wu and H. Yu, *Scalar induced gravitational waves in inflation with gravitationally enhanced friction*, *Phys. Rev. D* **101** (2020) 023529 [1912.05927].
- [135] S. Heydari and K. Karami, *Primordial black holes in nonminimal derivative coupling inflation with quartic potential and reheating consideration*, *Eur. Phys. J. C* **82** (2022) 83 [2107.10550].
- [136] S. Heydari and K. Karami, *Primordial black holes ensued from exponential potential and coupling parameter in nonminimal derivative inflation model*, *JCAP* **03** (2022) 033 [2111.00494].
- [137] S. Kawai and J. Kim, *Primordial black holes from Gauss-Bonnet-corrected single field inflation*, *Phys. Rev. D* **104** (2021) 083545 [2108.01340].
- [138] R. Arya, *Formation of Primordial Black Holes from Warm Inflation*, *JCAP* **09** (2020) 042 [1910.05238].

- [139] A. Ashoorioon, A. Rostami and J. T. Firouzjaee, *EFT compatible PBHs: effective spawning of the seeds for primordial black holes during inflation*, *JHEP* **07** (2021) 087 [[1912.13326](#)].
- [140] M. Bastero-Gil and M. S. Díaz-Blanco, *Gravity waves and primordial black holes in scalar warm little inflation*, *JCAP* **12** (2021) 052 [[2105.08045](#)].
- [141] O. Özsoy and Z. Lalak, *Primordial black holes as dark matter and gravitational waves from bumpy axion inflation*, *JCAP* **01** (2021) 040 [[2008.07549](#)].
- [142] M. Solbi and K. Karami, *Primordial black holes and induced gravitational waves in k -inflation*, *JCAP* **08** (2021) 056 [[2102.05651](#)].
- [143] M. Solbi and K. Karami, *Primordial black holes formation in the inflationary model with field-dependent kinetic term for quartic and natural potentials*, *Eur. Phys. J. C* **81** (2021) 884 [[2106.02863](#)].
- [144] Z. Teimoori, K. Rezazadeh, M. A. Rasheed and K. Karami, *Mechanism of primordial black holes production and secondary gravitational waves in α -attractor Galileon inflationary scenario*, *JCAP* **10** (2021) [[2107.07620](#)].
- [145] M. Correa, M. R. Gangopadhyay, N. Jaman and G. J. Mathews, *Primordial black-hole dark matter via warm natural inflation*, *Phys. Lett. B* **835** (2022) 137510 [[2207.10394](#)].
- [146] R. Kawaguchi and S. Tsujikawa, *Primordial black holes from Higgs inflation with a Gauss-Bonnet coupling*, *Phys. Rev. D* **107** (2023) 063508 [[2211.13364](#)].
- [147] A. Poisson, I. Timiryasov and S. Zell, *Critical points in Palatini Higgs inflation with small non-minimal coupling*, *JHEP* **03** (2024) 130 [[2306.03893](#)].
- [148] O. Özsoy and G. Tasinato, *Inflation and Primordial Black Holes*, *Universe* **9** (2023) 203 [[2301.03600](#)].
- [149] J. Kristiano and J. Yokoyama, *Constraining Primordial Black Hole Formation from Single-Field Inflation*, *Phys. Rev. Lett.* **132** (2024) 221003 [[2211.03395](#)].
- [150] A. Riotto, *The Primordial Black Hole Formation from Single-Field Inflation is Not Ruled Out*, [2301.00599](#).
- [151] J. Kristiano and J. Yokoyama, *Note on the bispectrum and one-loop corrections in single-field inflation with primordial black hole formation*, *Phys. Rev. D* **109** (2024) 103541 [[2303.00341](#)].
- [152] A. Riotto, *The Primordial Black Hole Formation from Single-Field Inflation is Still Not Ruled Out*, [2303.01727](#).
- [153] H. Firouzjahi, *One-loop corrections in power spectrum in single field inflation*, *JCAP* **10** (2023) 006 [[2303.12025](#)].
- [154] H. Firouzjahi and A. Riotto, *Primordial Black Holes and loops in single-field inflation*, *JCAP* **02** (2024) 021 [[2304.07801](#)].
- [155] G. Franciolini, A. Iovino, Junior., M. Taoso and A. Urbano, *Perturbativity in the presence of ultraslow-roll dynamics*, *Phys. Rev. D* **109** (2024) 123550 [[2305.03491](#)].
- [156] S.-L. Cheng, D.-S. Lee and K.-W. Ng, *Primordial perturbations from ultra-slow-roll single-field inflation with quantum loop effects*, *JCAP* **03** (2024) 008 [[2305.16810](#)].
- [157] S. Maity, H. V. Ragavendra, S. K. Sethi and L. Sriramkumar, *Loop contributions to the scalar power spectrum due to quartic order action in ultra slow roll inflation*, *JCAP* **05** (2024) 046 [[2307.13636](#)].

- [158] M. W. Davies, L. Iacconi and D. J. Mulryne, *Numerical 1-loop correction from a potential yielding ultra-slow-roll dynamics*, *JCAP* **04** (2024) 050 [[2312.05694](#)].
- [159] G. Ballesteros and J. G. Egea, *One-loop power spectrum in ultra slow-roll inflation and implications for primordial black hole dark matter*, *JCAP* **07** (2024) 052 [[2404.07196](#)].
- [160] J. Fumagalli, *Absence of one-loop effects on large scales from small scales in non-slow-roll dynamics*, [2305.19263](#).
- [161] Y. Tada, T. Terada and J. Tokuda, *Cancellation of quantum corrections on the soft curvature perturbations*, *JHEP* **01** (2024) 105 [[2308.04732](#)].
- [162] K. Inomata, *Superhorizon Curvature Perturbations Are Protected against One-Loop Corrections*, *Phys. Rev. Lett.* **133** (2024) 141001 [[2403.04682](#)].
- [163] R. Kawaguchi, S. Tsujikawa and Y. Yamada, *Proving the absence of large one-loop corrections to the power spectrum of curvature perturbations in transient ultra-slow-roll inflation within the path-integral approach*, *JHEP* **12** (2024) 095 [[2407.19742](#)].
- [164] J. Fumagalli, *Absence of one-loop effects on large scales from small scales in non-slow-roll dynamics II: Quartic interactions and consistency relations*, [2408.08296](#).
- [165] J. Garcia-Bellido, A. D. Linde and D. Wands, *Density perturbations and black hole formation in hybrid inflation*, *Phys. Rev. D* **54** (1996) 6040 [[astro-ph/9605094](#)].
- [166] M. Kawasaki and Y. Tada, *Can massive primordial black holes be produced in mild waterfall hybrid inflation?*, *JCAP* **08** (2016) 041 [[1512.03515](#)].
- [167] R. Kallosh and A. Linde, *Dilaton-axion inflation with PBHs and GWs*, *JCAP* **08** (2022) 037 [[2203.10437](#)].
- [168] M. Braglia, A. Linde, R. Kallosh and F. Finelli, *Hybrid α -attractors, primordial black holes and gravitational wave backgrounds*, *JCAP* **04** (2023) 033 [[2211.14262](#)].
- [169] Y. Tada and M. Yamada, *Primordial black hole formation in hybrid inflation*, *Phys. Rev. D* **107** (2023) 123539 [[2304.01249](#)].
- [170] Y. Tada and M. Yamada, *Stochastic dynamics of multi-waterfall hybrid inflation and formation of primordial black holes*, *JCAP* **11** (2023) 089 [[2306.07324](#)].
- [171] G. A. Palma, S. Sypsas and C. Zenteno, *Seeding primordial black holes in multifield inflation*, *Phys. Rev. Lett.* **125** (2020) 121301 [[2004.06106](#)].
- [172] J. Fumagalli, S. Renaux-Petel, J. W. Ronayne and L. T. Witkowski, *Turning in the landscape: A new mechanism for generating primordial black holes*, *Phys. Lett. B* **841** (2023) 137921 [[2004.08369](#)].
- [173] J. Fumagalli, S. Renaux-Petel and L. T. Witkowski, *Oscillations in the stochastic gravitational wave background from sharp features and particle production during inflation*, *JCAP* **08** (2021) 030 [[2012.02761](#)].
- [174] M. Braglia, D. K. Hazra, F. Finelli, G. F. Smoot, L. Sriramkumar and A. A. Starobinsky, *Generating PBHs and small-scale GWs in two-field models of inflation*, *JCAP* **08** (2020) 001 [[2005.02895](#)].
- [175] M. Braglia, X. Chen and D. K. Hazra, *Probing Primordial Features with the Stochastic Gravitational Wave Background*, *JCAP* **03** (2021) 005 [[2012.05821](#)].
- [176] S. Bhattacharya and I. Zavala, *Sharp turns in axion monodromy: primordial black holes and gravitational waves*, *JCAP* **04** (2023) 065 [[2205.06065](#)].

- [177] V. Aragam, S. Paban and R. Rosati, *Primordial Stochastic Gravitational Wave Backgrounds from a Sharp Feature in Three-field Inflation*, [2304.00065](#).
- [178] D. H. Lyth and D. Wands, *Generating the curvature perturbation without an inflaton*, *Phys. Lett. B* **524** (2002) 5 [[hep-ph/0110002](#)].
- [179] C. Chen and Y.-F. Cai, *Primordial black holes from sound speed resonance in the inflaton-curvaton mixed scenario*, *JCAP* **10** (2019) 068 [[1908.03942](#)].
- [180] A. D. Gow, T. Miranda and S. Nurmi, *Primordial black holes from a curvaton scenario with strongly non-Gaussian perturbations*, *JCAP* **11** (2023) 006 [[2307.03078](#)].
- [181] L.-H. Liu and T. Prokopec, *Non-minimally coupled curvaton*, *JCAP* **06** (2021) 033 [[2005.11069](#)].
- [182] S. Pi and M. Sasaki, *Primordial black hole formation in nonminimal curvaton scenarios*, *Phys. Rev. D* **108** (2023) L101301 [[2112.12680](#)].
- [183] M. Kawasaki, N. Kitajima and T. T. Yanagida, *Primordial black hole formation from an axionlike curvaton model*, *Phys. Rev. D* **87** (2013) 063519 [[1207.2550](#)].
- [184] K. Ando, K. Inomata, M. Kawasaki, K. Mukaida and T. T. Yanagida, *Primordial black holes for the LIGO events in the axionlike curvaton model*, *Phys. Rev. D* **97** (2018) 123512 [[1711.08956](#)].
- [185] K. Ando, M. Kawasaki and H. Nakatsuka, *Formation of primordial black holes in an axionlike curvaton model*, *Phys. Rev. D* **98** (2018) 083508 [[1805.07757](#)].
- [186] K. Inomata, M. Kawasaki, K. Mukaida and T. T. Yanagida, *NANOGrav Results and LIGO-Virgo Primordial Black Holes in Axionlike Curvaton Models*, *Phys. Rev. Lett.* **126** (2021) 131301 [[2011.01270](#)].
- [187] N. Bartolo, S. Matarrese and A. Riotto, *On nonGaussianity in the curvaton scenario*, *Phys. Rev. D* **69** (2004) 043503 [[hep-ph/0309033](#)].
- [188] N. Bartolo, S. Matarrese and A. Riotto, *Non-Gaussianity of Large-Scale Cosmic Microwave Background Anisotropies beyond Perturbation Theory*, *JCAP* **08** (2005) 010 [[astro-ph/0506410](#)].
- [189] M. Sasaki, J. Valiviita and D. Wands, *Non-Gaussianity of the primordial perturbation in the curvaton model*, *Phys. Rev. D* **74** (2006) 103003 [[astro-ph/0607627](#)].
- [190] K. Enqvist and T. Takahashi, *Signatures of Non-Gaussianity in the Curvaton Model*, *JCAP* **09** (2008) 012 [[0807.3069](#)].
- [191] M. Kawasaki, N. Kitajima and S. Yokoyama, *Gravitational waves from a curvaton model with blue spectrum*, *JCAP* **08** (2013) 042 [[1305.4464](#)].
- [192] G. Ferrante, G. Franciolini, A. Iovino, Junior. and A. Urbano, *Primordial black holes in the curvaton model: possible connections to pulsar timing arrays and dark matter*, *JCAP* **06** (2023) 057 [[2305.13382](#)].
- [193] C. Chen, A. Ghoshal, G. Tasinato and E. Tomberg, *Stochastic Axion-like Curvaton: Non-Gaussianity and Primordial Black Holes Without Large Power Spectrum*, [2409.12950](#).
- [194] N. Barnaby and M. Peloso, *Large Nongaussianity in Axion Inflation*, *Phys. Rev. Lett.* **106** (2011) 181301 [[1011.1500](#)].
- [195] L. Sorbo, *Parity violation in the Cosmic Microwave Background from a pseudoscalar inflaton*, *JCAP* **06** (2011) 003 [[1101.1525](#)].

- [196] R. Namba, M. Peloso, M. Shiraishi, L. Sorbo and C. Unal, *Scale-dependent gravitational waves from a rolling axion*, *JCAP* **01** (2016) 041 [[1509.07521](#)].
- [197] M. Shiraishi, A. Ricciardone and S. Saga, *Parity violation in the CMB bispectrum by a rolling pseudoscalar*, *JCAP* **11** (2013) 051 [[1308.6769](#)].
- [198] A. Linde, S. Mooij and E. Pajer, *Gauge field production in supergravity inflation: Local non-Gaussianity and primordial black holes*, *Phys. Rev. D* **87** (2013) 103506 [[1212.1693](#)].
- [199] E. Bugaev and P. Klimai, *Axion inflation with gauge field production and primordial black holes*, *Phys. Rev. D* **90** (2014) 103501 [[1312.7435](#)].
- [200] J. Garcia-Bellido, M. Peloso and C. Unal, *Gravitational waves at interferometer scales and primordial black holes in axion inflation*, *JCAP* **12** (2016) 031 [[1610.03763](#)].
- [201] A. Caravano, E. Komatsu, K. D. Lozanov and J. Weller, *Lattice simulations of axion- $U(1)$ inflation*, *Phys. Rev. D* **108** (2023) 043504 [[2204.12874](#)].
- [202] D. G. Figueroa, J. Lizarraga, A. Urrio and J. Urrestilla, *The strong backreaction regime in axion inflation*, [2303.17436](#).
- [203] A. Caravano and M. Peloso, *Unveiling the nonlinear dynamics of a rolling axion during inflation*, [2407.13405](#).
- [204] D. G. Figueroa, J. Lizarraga, N. Loayza, A. Urrio and J. Urrestilla, *The non-linear dynamics of axion inflation: a detailed lattice study*, [2411.16368](#).
- [205] L. Kofman, A. D. Linde and A. A. Starobinsky, *Reheating after inflation*, *Phys. Rev. Lett.* **73** (1994) 3195 [[hep-th/9405187](#)].
- [206] L. Kofman, A. D. Linde and A. A. Starobinsky, *Towards the theory of reheating after inflation*, *Phys. Rev. D* **56** (1997) 3258 [[hep-ph/9704452](#)].
- [207] F. Finelli and R. H. Brandenberger, *Parametric amplification of gravitational fluctuations during reheating*, *Phys. Rev. Lett.* **82** (1999) 1362 [[hep-ph/9809490](#)].
- [208] B. A. Bassett, F. Tamburini, D. I. Kaiser and R. Maartens, *Metric preheating and limitations of linearized gravity. 2.*, *Nucl. Phys. B* **561** (1999) 188 [[hep-ph/9901319](#)].
- [209] K. Jedamzik and G. Sigl, *On metric preheating*, *Phys. Rev. D* **61** (2000) 023519 [[hep-ph/9906287](#)].
- [210] B. A. Bassett and F. Viniegra, *Massless metric preheating*, *Phys. Rev. D* **62** (2000) 043507 [[hep-ph/9909353](#)].
- [211] K. Jedamzik, M. Lemoine and J. Martin, *Generation of gravitational waves during early structure formation between cosmic inflation and reheating*, *JCAP* **04** (2010) 021 [[1002.3278](#)].
- [212] K. Jedamzik, M. Lemoine and J. Martin, *Collapse of Small-Scale Density Perturbations during Preheating in Single Field Inflation*, *JCAP* **09** (2010) 034 [[1002.3039](#)].
- [213] J. Martin, T. Papanikolaou and V. Vennin, *Primordial black holes from the preheating instability in single-field inflation*, *JCAP* **01** (2020) 024 [[1907.04236](#)].
- [214] J. Martin, T. Papanikolaou, L. Pinol and V. Vennin, *Metric preheating and radiative decay in single-field inflation*, *JCAP* **05** (2020) 003 [[2002.01820](#)].
- [215] G. Ballesteros, J. Iguaz Juan, P. D. Serpico and M. Taoso, *Primordial black hole formation from self-resonant preheating?*, [2406.09122](#).

- [216] B. A. Bassett, D. I. Kaiser and R. Maartens, *General relativistic preheating after inflation*, *Phys. Lett. B* **455** (1999) 84 [[hep-ph/9808404](#)].
- [217] A. M. Green and K. A. Malik, *Primordial black hole production due to preheating*, *Phys. Rev. D* **64** (2001) 021301 [[hep-ph/0008113](#)].
- [218] B. A. Bassett and S. Tsujikawa, *Inflationary preheating and primordial black holes*, *Phys. Rev. D* **63** (2001) 123503 [[hep-ph/0008328](#)].
- [219] T. Suyama, T. Tanaka, B. Bassett and H. Kudoh, *Are black holes over-produced during preheating?*, *Phys. Rev. D* **71** (2005) 063507 [[hep-ph/0410247](#)].
- [220] E. Torres-Lomas and L. A. Urena-LAlpez, *Primordial black hole production during preheating in a chaotic inflationary model*, *AIP Conf. Proc.* **1548** (2013) 238 [[1308.1268](#)].
- [221] E. Torres-Lomas, J. C. Hidalgo, K. A. Malik and L. A. Ureña López, *Formation of subhorizon black holes from preheating*, *Phys. Rev. D* **89** (2014) 083008 [[1401.6960](#)].
- [222] X.-X. Kou, C. Tian and S.-Y. Zhou, *Oscillon Preheating in Full General Relativity*, *Class. Quant. Grav.* **38** (2021) 045005 [[1912.09658](#)].
- [223] C. Joana, *Gravitational dynamics in Higgs inflation: Preinflation and preheating with an auxiliary field*, *Phys. Rev. D* **106** (2022) 023504 [[2202.07604](#)].
- [224] P. Adshead, J. T. Giblin, R. Grutkoski and Z. J. Weiner, *Gauge preheating with full general relativity*, *JCAP* **03** (2024) 017 [[2311.01504](#)].
- [225] R. Easther, R. Flauger and J. B. Gilmore, *Delayed Reheating and the Breakdown of Coherent Oscillations*, *JCAP* **04** (2011) 027 [[1003.3011](#)].
- [226] Y. Cui and E. I. Sfakianakis, *Detectable gravitational wave signals from inflationary preheating*, *Phys. Lett. B* **840** (2023) 137825 [[2112.00762](#)].
- [227] R. H. Brandenberger, *The Matter Bounce Alternative to Inflationary Cosmology*, [1206.4196](#).
- [228] Y.-F. Cai, D. A. Easson and R. Brandenberger, *Towards a Nonsingular Bouncing Cosmology*, *JCAP* **08** (2012) 020 [[1206.2382](#)].
- [229] Y.-F. Cai, E. McDonough, F. Duplessis and R. H. Brandenberger, *Two Field Matter Bounce Cosmology*, *JCAP* **10** (2013) 024 [[1305.5259](#)].
- [230] J.-W. Chen, J. Liu, H.-L. Xu and Y.-F. Cai, *Tracing Primordial Black Holes in Nonsingular Bouncing Cosmology*, *Phys. Lett. B* **769** (2017) 561 [[1609.02571](#)].
- [231] S. Banerjee, T. Papanikolaou and E. N. Saridakis, *Constraining $F(R)$ bouncing cosmologies through primordial black holes*, *Phys. Rev. D* **106** (2022) 124012 [[2206.01150](#)].
- [232] T. Papanikolaou, S. Banerjee, Y.-F. Cai, S. Capozziello and E. N. Saridakis, *Primordial black holes and induced gravitational waves in non-singular matter bouncing cosmology*, *JCAP* **06** (2024) 066 [[2404.03779](#)].
- [233] T. Papanikolaou, V. Vennin and D. Langlois, *Gravitational waves from a universe filled with primordial black holes*, *JCAP* **03** (2021) 053 [[2010.11573](#)].
- [234] G. Domènech, C. Lin and M. Sasaki, *Gravitational wave constraints on the primordial black hole dominated early universe*, *JCAP* **04** (2021) 062 [[2012.08151](#)].
- [235] G. Domènech, V. Takhistov and M. Sasaki, *Exploring evaporating primordial black holes with gravitational waves*, *Phys. Lett. B* **823** (2021) 136722 [[2105.06816](#)].

- [236] G. Domènech, S. Passaglia and S. Renaux-Petel, *Gravitational waves from dark matter isocurvature*, *JCAP* **03** (2022) 023 [2112.10163].
- [237] G. Domènech, *Cosmological gravitational waves from isocurvature fluctuations*, *AAPPS Bull.* **34** (2024) 4 [2311.02065].
- [238] T. Papanikolaou, X.-C. He, X.-H. Ma, Y.-F. Cai, E. N. Saridakis and M. Sasaki, *New probe of non-Gaussianities with primordial black hole induced gravitational waves*, *Phys. Lett. B* **857** (2024) 138997 [2403.00660].
- [239] X.-C. He, Y.-F. Cai, X.-H. Ma, T. Papanikolaou, E. N. Saridakis and M. Sasaki, *Gravitational waves from primordial black hole isocurvature: the effect of non-Gaussianities*, *JCAP* **12** (2024) 039 [2409.11333].
- [240] T. Papanikolaou, C. Tzerefos, S. Basilakos and E. N. Saridakis, *Scalar induced gravitational waves from primordial black hole Poisson fluctuations in $f(R)$ gravity*, *JCAP* **10** (2022) 013 [2112.15059].
- [241] T. Papanikolaou, C. Tzerefos, S. Basilakos and E. N. Saridakis, *No constraints for $f(T)$ gravity from gravitational waves induced from primordial black hole fluctuations*, *Eur. Phys. J. C* **83** (2023) 31 [2205.06094].
- [242] C. Tzerefos, T. Papanikolaou, E. N. Saridakis and S. Basilakos, *Scalar induced gravitational waves in modified teleparallel gravity theories*, *Phys. Rev. D* **107** (2023) 124019 [2303.16695].
- [243] G. Dvali, L. Eisemann, M. Michel and S. Zell, *Black hole metamorphosis and stabilization by memory burden*, *Phys. Rev. D* **102** (2020) 103523 [2006.00011].
- [244] G. Domènech and M. Sasaki, *Gravitational wave hints black hole remnants as dark matter*, *Class. Quant. Grav.* **40** (2023) 177001 [2303.07661].
- [245] G. Franciolini and P. Pani, *Stochastic gravitational-wave background at $\mathcal{I}G$ detectors as a smoking gun for microscopic dark matter relics*, *Phys. Rev. D* **108** (2023) 083527 [2304.13576].
- [246] S. Balaji, G. Domènech, G. Franciolini, A. Ganz and J. Tränkle, *Probing modified Hawking evaporation with gravitational waves from the primordial black hole dominated universe*, *JCAP* **11** (2024) 026 [2403.14309].
- [247] G. Dvali, J. S. Valbuena-Bermúdez and M. Zantedeschi, *Memory burden effect in black holes and solitons: Implications for PBH*, *Phys. Rev. D* **110** (2024) 056029 [2405.13117].
- [248] K. Kohri, T. Terada and T. T. Yanagida, *Induced Gravitational Waves probing Primordial Black Hole Dark Matter with Memory Burden*, 2409.06365.
- [249] N. Bhaumik, M. R. Haque, R. K. Jain and M. Lewicki, *Memory burden effect mimics reheating signatures on SGWB from ultra-low mass PBH domination*, *JHEP* **10** (2024) 142 [2409.04436].
- [250] G. Domènech and J. Tränkle, *From formation to evaporation: Induced gravitational wave probes of the primordial black hole reheating scenario*, 2409.12125.
- [251] D. Wands, *Duality invariance of cosmological perturbation spectra*, *Phys. Rev. D* **60** (1999) 023507 [gr-qc/9809062].
- [252] P. S. Cole, A. D. Gow, C. T. Byrnes and S. P. Patil, *Primordial black holes from single-field inflation: a fine-tuning audit*, *JCAP* **08** (2023) 031 [2304.01997].

- [253] E. Madge, E. Morgante, C. Puchades-Ibáñez, N. Ramberg, W. Ratzinger, S. Schenk et al., *Primordial gravitational waves in the nano-Hertz regime and PTA data — towards solving the GW inverse problem*, *JHEP* **10** (2023) 171 [[2306.14856](#)].
- [254] PLANCK collaboration, *Planck 2018 results. X. Constraints on inflation*, *Astron. Astrophys.* **641** (2020) A10 [[1807.06211](#)].
- [255] S. Pi and M. Sasaki, *Gravitational Waves Induced by Scalar Perturbations with a Lognormal Peak*, *JCAP* **09** (2020) 037 [[2005.12306](#)].
- [256] V. Dandoy, V. Domcke and F. Rompineve, *Search for scalar induced gravitational waves in the international pulsar timing array data release 2 and NANOgrav 12.5 years datasets*, *SciPost Phys. Core* **6** (2023) 060 [[2302.07901](#)].
- [257] C. T. Byrnes, P. S. Cole and S. P. Patil, *Steepest growth of the power spectrum and primordial black holes*, *JCAP* **06** (2019) 028 [[1811.11158](#)].
- [258] C.-Z. Li, C. Yuan and Q.-g. Huang, *Gravitational Waves Induced by Scalar Perturbations with a Broken Power-law Peak*, [2407.12914](#).
- [259] J. Chluba, J. Hamann and S. P. Patil, *Features and New Physical Scales in Primordial Observables: Theory and Observation*, *Int. J. Mod. Phys. D* **24** (2015) 1530023 [[1505.01834](#)].
- [260] A. Slosar et al., *Scratches from the Past: Inflationary Archaeology through Features in the Power Spectrum of Primordial Fluctuations*, *Bull. Am. Astron. Soc.* **51** (2019) 98 [[1903.09883](#)].
- [261] A. A. Starobinsky, *Spectrum of adiabatic perturbations in the universe when there are singularities in the inflation potential*, *JETP Lett.* **55** (1992) 489.
- [262] J. Fumagalli, S. Renaux-Petel and L. T. Witkowski, *Resonant features in the stochastic gravitational wave background*, *JCAP* **08** (2021) 059 [[2105.06481](#)].
- [263] L. T. Witkowski, G. Domènech, J. Fumagalli and S. Renaux-Petel, *Expansion history-dependent oscillations in the scalar-induced gravitational wave background*, *JCAP* **05** (2022) 028 [[2110.09480](#)].
- [264] J. Fumagalli, M. Pieroni, S. Renaux-Petel and L. T. Witkowski, *Detecting primordial features with LISA*, *JCAP* **07** (2022) 020 [[2112.06903](#)].
- [265] S. Groot Nibbelink and B. J. W. van Tent, *Density perturbations arising from multiple field slow roll inflation*, [hep-ph/0011325](#).
- [266] S. Groot Nibbelink and B. J. W. van Tent, *Scalar perturbations during multiple field slow-roll inflation*, *Class. Quant. Grav.* **19** (2002) 613 [[hep-ph/0107272](#)].
- [267] P. S. Cole, A. D. Gow, C. T. Byrnes and S. P. Patil, *Smooth vs instant inflationary transitions: steepest growth re-examined and primordial black holes*, *JCAP* **05** (2024) 022 [[2204.07573](#)].
- [268] G. Franciolini and A. Urbano, *Primordial black hole dark matter from inflation: The reverse engineering approach*, *Phys. Rev. D* **106** (2022) 123519 [[2207.10056](#)].
- [269] J. Ellis and D. Wands, *Inflation (2023)*, [2312.13238](#).
- [270] M. Sasaki, *Large Scale Quantum Fluctuations in the Inflationary Universe*, *Prog. Theor. Phys.* **76** (1986) 1036.

- [271] V. F. Mukhanov, *Quantum Theory of Gauge Invariant Cosmological Perturbations*, *Sov. Phys. JETP* **67** (1988) 1297.
- [272] BICEP, KECK collaboration, *Improved Constraints on Primordial Gravitational Waves using Planck, WMAP, and BICEP/Keck Observations through the 2018 Observing Season*, *Phys. Rev. Lett.* **127** (2021) 151301 [[2110.00483](#)].
- [273] S.-L. Cheng, D.-S. Lee and K.-W. Ng, *Power spectrum of primordial perturbations during ultra-slow-roll inflation with back reaction effects*, *Phys. Lett. B* **827** (2022) 136956 [[2106.09275](#)].
- [274] J. Kristiano and J. Yokoyama, *Comparing sharp and smooth transitions of the second slow-roll parameter in single-field inflation*, *JCAP* **10** (2024) 036 [[2405.12145](#)].
- [275] L. Iacconi, D. Mulryne and D. Seery, *Loop corrections in the separate universe picture*, *JCAP* **06** (2024) 062 [[2312.12424](#)].
- [276] H. Motohashi and Y. Tada, *Squeezed bispectrum and one-loop corrections in transient constant-roll inflation*, *JCAP* **08** (2023) 069 [[2303.16035](#)].
- [277] G. Tasinato, *Non-Gaussianities and the large $-\eta$ approach to inflation*, *Phys. Rev. D* **109** (2024) 063510 [[2312.03498](#)].
- [278] G. Tasinato, *Large $-\eta$ approach to single field inflation*, *Phys. Rev. D* **108** (2023) 043526 [[2305.11568](#)].
- [279] H. Firouzjahi, *Revisiting loop corrections in single field ultraslow-roll inflation*, *Phys. Rev. D* **109** (2024) 043514 [[2311.04080](#)].
- [280] M. Braglia and L. Pinol, *No time to derive: unraveling total time derivatives in in-in perturbation theory*, *JHEP* **08** (2024) 068 [[2403.14558](#)].
- [281] R. Kawaguchi, S. Tsujikawa and Y. Yamada, *Roles of boundary and equation-of-motion terms in cosmological correlation functions*, *Phys. Lett. B* **856** (2024) 138962 [[2403.16022](#)].
- [282] D. Green and K. Gupta, *Soft Metric Fluctuations During Inflation*, [2410.11973](#).
- [283] A. Caravano, G. Franciolini and S. Renaux-Petel, *Ultra-Slow-Roll Inflation on the Lattice: Backreaction and Nonlinear Effects*, [2410.23942](#).
- [284] V. Atal and C. Germani, *The role of non-gaussianities in Primordial Black Hole formation*, *Phys. Dark Univ.* **24** (2019) 100275 [[1811.07857](#)].
- [285] M. Biagetti, G. Franciolini, A. Kehagias and A. Riotto, *Primordial Black Holes from Inflation and Quantum Diffusion*, *JCAP* **07** (2018) 032 [[1804.07124](#)].
- [286] E. Tomberg, *Stochastic constant-roll inflation and primordial black holes*, *Phys. Rev. D* **108** (2023) 043502 [[2304.10903](#)].
- [287] G. Franciolini, A. Iovino, Junior., V. Vaskonen and H. Veermae, *The recent gravitational wave observation by pulsar timing arrays and primordial black holes: the importance of non-gaussianities*, [2306.17149](#).
- [288] G. Ballesteros, T. Konstandin, A. Pérez Rodríguez, M. Pierre and J. Rey, *Non-Gaussian tails without stochastic inflation*, *JCAP* **11** (2024) 013 [[2406.02417](#)].
- [289] P. Bari, A. Ricciardone, N. Bartolo, D. Bertacca and S. Matarrese, *Signatures of Primordial Gravitational Waves on the Large-Scale Structure of the Universe*, *Phys. Rev. Lett.* **129** (2022) 091301 [[2111.06884](#)].

- [290] P. Bari, D. Bertacca, N. Bartolo, A. Ricciardone, S. Giardiello and S. Matarrese, *An analytical study of the primordial gravitational-wave-induced contribution to the large-scale structure of the Universe*, *JCAP* **07** (2023) 034 [2209.05329].
- [291] P. Bari, N. Bartolo, G. Domènech and S. Matarrese, *Gravitational waves induced by scalar-tensor mixing*, *Phys. Rev. D* **109** (2024) 023509 [2307.05404].
- [292] R. Picard and K. A. Malik, *Induced gravitational waves: the effect of first order tensor perturbations*, *JCAP* **10** (2024) 010 [2311.14513].
- [293] PLANCK collaboration, *Planck 2018 results. VI. Cosmological parameters*, *Astron. Astrophys.* **641** (2020) A6 [1807.06209].
- [294] S. Borsanyi et al., *Calculation of the axion mass based on high-temperature lattice quantum chromodynamics*, *Nature* **539** (2016) 69 [1606.07494].
- [295] J. R. Espinosa, D. Racco and A. Riotto, *A Cosmological Signature of the SM Higgs Instability: Gravitational Waves*, *JCAP* **09** (2018) 012 [1804.07732].
- [296] K. Kohri and T. Terada, *Semianalytic calculation of gravitational wave spectrum nonlinearly induced from primordial curvature perturbations*, *Phys. Rev. D* **97** (2018) 123532 [1804.08577].
- [297] K. A. Malik and D. Wands, *Cosmological perturbations*, *Phys. Rept.* **475** (2009) 1 [0809.4944].
- [298] V. De Luca, G. Franciolini, A. Kehagias and A. Riotto, *On the Gauge Invariance of Cosmological Gravitational Waves*, *JCAP* **03** (2020) 014 [1911.09689].
- [299] K. Inomata and T. Terada, *Gauge Independence of Induced Gravitational Waves*, *Phys. Rev. D* **101** (2020) 023523 [1912.00785].
- [300] C. Yuan, Z.-C. Chen and Q.-G. Huang, *Scalar induced gravitational waves in different gauges*, *Phys. Rev. D* **101** (2020) 063018 [1912.00885].
- [301] G. Domènech and M. Sasaki, *Approximate gauge independence of the induced gravitational wave spectrum*, *Phys. Rev. D* **103** (2021) 063531 [2012.14016].
- [302] K. Inomata, K. Kohri, T. Nakama and T. Terada, *Enhancement of Gravitational Waves Induced by Scalar Perturbations due to a Sudden Transition from an Early Matter Era to the Radiation Era*, *Phys. Rev. D* **100** (2019) 043532 [1904.12879].
- [303] K. Inomata, K. Kohri, T. Nakama and T. Terada, *Gravitational Waves Induced by Scalar Perturbations during a Gradual Transition from an Early Matter Era to the Radiation Era*, *JCAP* **10** (2019) 071 [1904.12878].
- [304] S. Kumar, H. Tai and L.-T. Wang, *Towards a Complete Treatment of Scalar-induced Gravitational Waves with Early Matter Domination*, [2410.17291](#).
- [305] M. Pearce, L. Pearce, G. White and C. Balazs, *Gravitational wave signals from early matter domination: interpolating between fast and slow transitions*, *JCAP* **06** (2024) 021 [2311.12340].
- [306] K. Inomata, M. Kawasaki, K. Mukaida, T. Terada and T. T. Yanagida, *Gravitational Wave Production right after a Primordial Black Hole Evaporation*, *Phys. Rev. D* **101** (2020) 123533 [2003.10455].
- [307] Z. Yi, Z.-Q. You and Y. Wu, *Model-independent reconstruction of the primordial curvature power spectrum from PTA data*, *JCAP* **01** (2024) 066 [2308.05632].

- [308] F. Kuhnel and I. Stamou, *Reconstructing Primordial Black Hole Power Spectra from Gravitational Waves*, [2404.06547](#).
- [309] X.-X. Zeng, R.-G. Cai and S.-J. Wang, *Multiple peaks in gravitational waves induced from primordial curvature perturbations with non-Gaussianity*, [2406.05034](#).
- [310] K. Inomata, *Bound on induced gravitational waves during inflation era*, *Phys. Rev. D* **104** (2021) 123525 [[2109.06192](#)].
- [311] J. Fumagalli, G. A. Palma, S. Renaux-Petel, S. Sypsas, L. T. Witkowski and C. Zenteno, *Primordial gravitational waves from excited states*, *JHEP* **03** (2022) 196 [[2111.14664](#)].
- [312] C. Unal, A. Papageorgiou and I. Obata, *Axion-gauge dynamics during inflation as the origin of pulsar timing array signals and primordial black holes*, *Phys. Lett. B* **856** (2024) 138873 [[2307.02322](#)].
- [313] L. Iacconi and D. J. Mulryne, *Multi-field inflation with large scalar fluctuations: non-Gaussianity and perturbativity*, *JCAP* **09** (2023) 033 [[2304.14260](#)].
- [314] V. Atal and G. Domènech, *Probing non-Gaussianities with the high frequency tail of induced gravitational waves*, *JCAP* **06** (2021) 001 [[2103.01056](#)].
- [315] H. V. Ragavendra, *Accounting for scalar non-Gaussianity in secondary gravitational waves*, *Phys. Rev. D* **105** (2022) 063533 [[2108.04193](#)].
- [316] J. A. Ruiz and J. Rey, *Gravitational waves in ultra-slow-roll and their anisotropy at two loops*, [2410.09014](#).
- [317] R. Inui, C. Joana, H. Motohashi, S. Pi, Y. Tada and S. Yokoyama, *Primordial black holes and induced gravitational waves from logarithmic non-Gaussianity*, [2411.07647](#).
- [318] J. W. Armstrong, F. B. Estabrook and M. Tinto, *Time-delay interferometry for space-based gravitational wave searches*, *The Astrophysical Journal* **527** (1999) 814.
- [319] T. A. Prince, M. Tinto, S. L. Larson and J. W. Armstrong, *The LISA optimal sensitivity*, *Phys. Rev. D* **66** (2002) 122002 [[gr-qc/0209039](#)].
- [320] D. A. Shaddock, *Operating LISA as a Sagnac interferometer*, *Phys. Rev. D* **69** (2004) 022001 [[gr-qc/0306125](#)].
- [321] D. A. Shaddock, M. Tinto, F. B. Estabrook and J. W. Armstrong, *Data combinations accounting for LISA spacecraft motion*, *Phys. Rev. D* **68** (2003) 061303 [[gr-qc/0307080](#)].
- [322] M. Tinto, F. B. Estabrook and J. W. Armstrong, *Time delay interferometry with moving spacecraft arrays*, *Phys. Rev. D* **69** (2004) 082001 [[gr-qc/0310017](#)].
- [323] M. Vallisneri, *Geometric time delay interferometry*, *Phys. Rev. D* **72** (2005) 042003 [[gr-qc/0504145](#)].
- [324] M. Muratore, D. Vetrugno and S. Vitale, *Revisitation of time delay interferometry combinations that suppress laser noise in LISA*, *Class. Quant. Grav.* **37** (2020) 185019 [[2001.11221](#)].
- [325] M. Tinto and S. V. Dhurandhar, *Time-delay interferometry*, *Living Rev. Rel.* **24** (2021) 1.
- [326] M. Muratore, D. Vetrugno, S. Vitale and O. Hartwig, *Time delay interferometry combinations as instrument noise monitors for LISA*, *Phys. Rev. D* **105** (2022) 023009 [[2108.02738](#)].

- [327] O. Hartwig, M. Lilley, M. Muratore and M. Pieroni, *Stochastic gravitational wave background reconstruction for a nonequilateral and unequal-noise LISA constellation*, *Phys. Rev. D* **107** (2023) 123531 [[2303.15929](#)].
- [328] LISA COSMOLOGY WORKING GROUP collaboration, *Gravitational waves from first-order phase transitions in LISA: reconstruction pipeline and physics interpretation*, *JCAP* **10** (2024) 020 [[2403.03723](#)].
- [329] LISA COSMOLOGY WORKING GROUP collaboration, *Gravitational waves from cosmic strings in LISA: reconstruction pipeline and physics interpretation*, [2405.03740](#).
- [330] W. Martens and E. Joffre, *Trajectory Design for the ESA LISA Mission*, [2101.03040](#).
- [331] G. Mentasti, C. R. Contaldi and M. Peloso, *Probing the galactic and extragalactic gravitational wave backgrounds with space-based interferometers*, *JCAP* **06** (2024) 055 [[2312.10792](#)].
- [332] J. Kume, M. Peloso, M. Pieroni and A. Ricciardone, *Assessing the Impact of Unequal Noises and Foreground Modeling on SGWB Reconstruction with LISA*, [2410.10342](#).
- [333] O. Hartwig and M. Muratore, *Characterization of time delay interferometry combinations for the LISA instrument noise*, *Phys. Rev. D* **105** (2022) 062006 [[2111.00975](#)].
- [334] C. J. Hogan and P. L. Bender, *Estimating stochastic gravitational wave backgrounds with Sagnac calibration*, *Phys. Rev. D* **64** (2001) 062002 [[astro-ph/0104266](#)].
- [335] M. R. Adams and N. J. Cornish, *Discriminating between a Stochastic Gravitational Wave Background and Instrument Noise*, *Phys. Rev. D* **82** (2010) 022002 [[1002.1291](#)].
- [336] M. Muratore, O. Hartwig, D. Vetrugno, S. Vitale and W. J. Weber, *Effectiveness of null time-delay interferometry channels as instrument noise monitors in LISA*, *Phys. Rev. D* **107** (2023) 082004 [[2207.02138](#)].
- [337] N. J. Cornish and J. Crowder, *LISA data analysis using MCMC methods*, *Phys. Rev. D* **72** (2005) 043005 [[gr-qc/0506059](#)].
- [338] M. Vallisneri, *A LISA Data-Analysis Primer*, *Class. Quant. Grav.* **26** (2009) 094024 [[0812.0751](#)].
- [339] MOCK LISA DATA CHALLENGE TASK FORCE collaboration, *The Mock LISA Data Challenges: From Challenge 3 to Challenge 4*, *Class. Quant. Grav.* **27** (2010) 084009 [[0912.0548](#)].
- [340] J. Alvey, U. Bhardwaj, V. Domcke, M. Pieroni and C. Weniger, *Simulation-based inference for stochastic gravitational wave background data analysis*, *Phys. Rev. D* **109** (2024) 083008 [[2309.07954](#)].
- [341] T. Robson, N. J. Cornish and C. Liu, *The construction and use of LISA sensitivity curves*, *Class. Quant. Grav.* **36** (2019) 105011 [[1803.01944](#)].
- [342] M. Armano, H. Audley, G. Auger, J. T. Baird, M. Bassan, P. Binetruy et al., *Sub-femto-g free fall for space-based gravitational wave observatories: Lisa pathfinder results*, *Phys. Rev. Lett.* **116** (2016) 231101.
- [343] D. Quang Nam, Y. Lemièrè, A. Petiteau, J.-B. Bayle, O. Hartwig, J. Martino et al., *Time-delay interferometry noise transfer functions for LISA*, *Phys. Rev. D* **108** (2023) 082004 [[2211.02539](#)].

- [344] R. Schneider, V. Ferrari, S. Matarrese and S. F. Portegies Zwart, *Low-frequency gravitational waves from cosmological compact binaries*, *Monthly Notices of the Royal Astronomical Society* **324** (2001) 797 [<https://academic.oup.com/mnras/article-pdf/324/4/797/4142158/324-4-797.pdf>].
- [345] A. J. Farmer and E. S. Phinney, *The gravitational wave background from cosmological compact binaries*, *Mon. Not. Roy. Astron. Soc.* **346** (2003) 1197 [[astro-ph/0304393](#)].
- [346] T. Regimbau, *The astrophysical gravitational wave stochastic background*, *Res. Astron. Astrophys.* **11** (2011) 369 [[1101.2762](#)].
- [347] F. Pozzoli, S. Babak, A. Sesana, M. Bonetti and N. Karnesis, *Computation of stochastic background from extreme-mass-ratio inspiral populations for LISA*, *Phys. Rev. D* **108** (2023) 103039 [[2302.07043](#)].
- [348] S. Babak, C. Caprini, D. G. Figueroa, N. Karnesis, P. Marcoccia, G. Nardini et al., *Stochastic gravitational wave background from stellar origin binary black holes in LISA*, *JCAP* **08** (2023) 034 [[2304.06368](#)].
- [349] S. Staelens and G. Nelemans, *Likelihood of white dwarf binaries to dominate the astrophysical gravitational wave background in the mHz band*, *Astron. Astrophys.* **683** (2024) A139 [[2310.19448](#)].
- [350] A. Toubiana, N. Karnesis, A. Lamberts and M. C. Miller, *The interacting double white dwarf population with LISA; stochastic foreground and resolved sources*, [2403.16867](#).
- [351] C. R. Evans, I. Iben and L. Smarr, *Degenerate dwarf binaries as promising, detectable sources of gravitational radiation*, *Astrophys. J.* **323** (1987) 129.
- [352] P. Bender and D. Hils, *Confusion noise level due to galactic and extragalactic binaries*, *Class. Quant. Grav.* **14** (1997) 1439.
- [353] LIGO SCIENTIFIC, VIRGO collaboration, *Search for the isotropic stochastic background using data from Advanced LIGO's second observing run*, *Phys. Rev.* **D100** (2019) 061101 [[1903.02886](#)].
- [354] S. Nissanke, M. Vallisneri, G. Nelemans and T. A. Prince, *Gravitational-wave emission from compact Galactic binaries*, *Astrophys. J.* **758** (2012) 131 [[1201.4613](#)].
- [355] M. R. Adams and N. J. Cornish, *Detecting a Stochastic Gravitational Wave Background in the presence of a Galactic Foreground and Instrument Noise*, *Phys. Rev. D* **89** (2014) 022001 [[1307.4116](#)].
- [356] M. Hindmarsh, D. C. Hooper, T. Minkinen and D. J. Weir, *Recovering a phase transition signal in simulated LISA data with a modulated galactic foreground*, [2406.04894](#).
- [357] Q. Baghi, N. Korsakova, J. Slutsky, E. Castelli, N. Karnesis and J.-B. Bayle, *Detection and characterization of instrumental transients in LISA Pathfinder and their projection to LISA*, *Phys. Rev. D* **105** (2022) 042002 [[2112.07490](#)].
- [358] T. Robson and N. J. Cornish, *Detecting Gravitational Wave Bursts with LISA in the presence of Instrumental Glitches*, *Phys. Rev. D* **99** (2019) 024019 [[1811.04490](#)].
- [359] P. A. Seoane et al., *The effect of mission duration on LISA science objectives*, *Gen. Rel. Grav.* **54** (2022) 3 [[2107.09665](#)].
- [360] J. Alvey, U. Bhardwaj, V. Domcke, M. Pieroni and C. Weniger, *Leveraging Time-Dependent Instrumental Noise for LISA SGWB Analysis*, [2408.00832](#).

- [361] R. Buscicchio, A. Klein, V. Korol, F. Di Renzo, C. J. Moore, D. Gerosa et al., *A test for LISA foreground Gaussianity and stationarity. I. Galactic white-dwarf binaries*, [2410.08263](#).
- [362] N. Karnesis, A. Sasli, R. Buscicchio and N. Stergioulas, *Characterization of non-Gaussian stochastic signals with heavier-tailed likelihoods*, [2410.14354](#).
- [363] N. Karnesis, S. Babak, M. Pieroni, N. Cornish and T. Littenberg, *Characterization of the stochastic signal originating from compact binary populations as measured by LISA*, *Phys. Rev. D* **104** (2021) 043019 [[2103.14598](#)].
- [364] S. Hofman and G. Nelemans, *On the uncertainty of the White Dwarf Astrophysical Gravitational Wave Background*, [2407.10642](#).
- [365] G. Boileau, T. Bruel, A. Toubiana, A. Lamberts and N. Christensen, *Gravitational Wave Background from Extragalactic Double White Dwarfs for LISA*, [to appear](#).
- [366] N. Seto and K. Kyutoku, *How many extragalactic stellar mass binary black holes will be detected by space gravitational-wave interferometers?*, *Mon. Not. Roy. Astron. Soc.* **514** (2022) 4669 [[2201.02766](#)].
- [367] L. Lehoucq, I. Dvorkin, R. Srinivasan, C. Pellouin and A. Lamberts, *Astrophysical Uncertainties in the Gravitational-Wave Background from Stellar-Mass Compact Binary Mergers*, [2306.09861](#).
- [368] K. Ruiz-Rocha, K. Holley-Bockelmann, K. Jani, M. Mapelli, S. Dunham and W. Gabella, *A Sea of Black Holes: Characterizing the LISA Signature for Stellar-Origin Black Hole Binaries*, [2407.21161](#).
- [369] A. Sesana, *Prospects for Multiband Gravitational-Wave Astronomy after GW150914*, *Phys. Rev. Lett.* **116** (2016) 231102 [[1602.06951](#)].
- [370] R. Buscicchio, J. Torrado, C. Caprini, G. Nardini, N. Karnesis, M. Pieroni et al., *Stellar-mass black-hole binaries in LISA: characteristics and complementarity with current-generation interferometers*, [2410.18171](#).
- [371] KAGRA, VIRGO, LIGO SCIENTIFIC collaboration, *Population of Merging Compact Binaries Inferred Using Gravitational Waves through GWTC-3*, *Phys. Rev. X* **13** (2023) 011048 [[2111.03634](#)].
- [372] KAGRA, VIRGO, LIGO SCIENTIFIC collaboration, *Upper limits on the isotropic gravitational-wave background from Advanced LIGO and Advanced Virgo's third observing run*, *Phys. Rev. D* **104** (2021) 022004 [[2101.12130](#)].
- [373] R. E. Kass and A. E. Raftery, *Bayes Factors*, *J. Am. Statist. Assoc.* **90** (1995) 773.
- [374] J. Torrado and A. Lewis, *Cobaya: Code for Bayesian Analysis of hierarchical physical models*, *JCAP* **05** (2021) 057 [[2005.05290](#)].
- [375] J. Bradbury, R. Frostig, P. Hawkins, M. J. Johnson, C. Leary, D. Maclaurin et al., *JAX: composable transformations of Python+NumPy programs*, 2018.
- [376] C. Germani and I. Musco, *Abundance of Primordial Black Holes Depends on the Shape of the Inflationary Power Spectrum*, *Phys. Rev. Lett.* **122** (2019) 141302 [[1805.04087](#)].
- [377] I. Musco, *Threshold for primordial black holes: Dependence on the shape of the cosmological perturbations*, *Phys. Rev. D* **100** (2019) 123524 [[1809.02127](#)].

- [378] A. Escrivà, C. Germani and R. K. Sheth, *Universal threshold for primordial black hole formation*, *Phys. Rev. D* **101** (2020) 044022 [[1907.13311](#)].
- [379] S. Young, *The primordial black hole formation criterion re-examined: Parametrisation, timing and the choice of window function*, *Int. J. Mod. Phys. D* **29** (2019) 2030002 [[1905.01230](#)].
- [380] R. Saito and J. Yokoyama, *Gravitational wave background as a probe of the primordial black hole abundance*, *Phys. Rev. Lett.* **102** (2009) 161101 [[0812.4339](#)].
- [381] A. D. Gow, C. T. Byrnes, P. S. Cole and S. Young, *The power spectrum on small scales: Robust constraints and comparing PBH methodologies*, *JCAP* **02** (2021) 002 [[2008.03289](#)].
- [382] M. Lewicki, P. Toczec and V. Vaskonen, *Primordial black holes from strong first-order phase transitions*, *JHEP* **09** (2023) 092 [[2305.04924](#)].
- [383] R.-G. Cai, Y.-S. Hao and S.-J. Wang, *Primordial black holes and curvature perturbations from false vacuum islands*, [2404.06506](#).
- [384] M. Lewicki, P. Toczec and V. Vaskonen, *Black holes and gravitational waves from slow phase transitions*, [2402.04158](#).
- [385] T. Nakama, B. Carr and J. Silk, *Limits on primordial black holes from μ distortions in cosmic microwave background*, *Phys. Rev. D* **97** (2018) 043525 [[1710.06945](#)].
- [386] C. Ünal, E. D. Kovetz and S. P. Patil, *Multimessenger probes of inflationary fluctuations and primordial black holes*, *Phys. Rev. D* **103** (2021) 063519 [[2008.11184](#)].
- [387] C. T. Byrnes, J. Lesgourgues and D. Sharma, *Robust μ -distortion constraints on primordial supermassive black holes from non-Gaussian perturbations*, *JCAP* **09** (2024) 012 [[2404.18475](#)].
- [388] A. J. Iovino, G. Perna, A. Riotto and H. Veermäe, *Curbing PBHs with PTAs*, *JCAP* **10** (2024) 050 [[2406.20089](#)].
- [389] A. Hook, G. Marques-Tavares and D. Racco, *Causal gravitational waves as a probe of free streaming particles and the expansion of the Universe*, *JHEP* **02** (2021) 117 [[2010.03568](#)].
- [390] D. Racco and D. Poletti, *Precision cosmology with primordial GW backgrounds in presence of astrophysical foregrounds*, *JCAP* **04** (2023) 054 [[2212.06602](#)].
- [391] C. Caprini, R. Durrer, T. Konstandin and G. Servant, *General Properties of the Gravitational Wave Spectrum from Phase Transitions*, *Phys. Rev. D* **79** (2009) 083519 [[0901.1661](#)].
- [392] R. Allahverdi et al., *The First Three Seconds: a Review of Possible Expansion Histories of the Early Universe*, [2006.16182](#).
- [393] S. Allegrini, L. Del Grosso, A. J. Iovino and A. Urbano, *Is the formation of primordial black holes from single-field inflation compatible with standard cosmology?*, [2412.14049](#).
- [394] H. Assadullahi and D. Wands, *Gravitational waves from an early matter era*, *Phys. Rev. D* **79** (2009) 083511 [[0901.0989](#)].
- [395] B. Eggemeier, J. C. Niemeyer, K. Jedamzik and R. Easther, *Stochastic gravitational waves from postinflationary structure formation*, *Phys. Rev. D* **107** (2023) 043503 [[2212.00425](#)].
- [396] N. Fernandez, J. W. Foster, B. Lillard and J. Shelton, *Stochastic Gravitational Waves from Early Structure Formation*, *Phys. Rev. Lett.* **133** (2024) 111002 [[2312.12499](#)].

- [397] L. E. Padilla, J. C. Hidalgo, K. A. Malik and D. Mulryne, *Detecting the Stochastic Gravitational Wave Background from Primordial Black Holes in Slow-reheating Scenarios*, [2405.19271](#).
- [398] A. Escrivà, Y. Tada and C.-M. Yoo, *Primordial Black Holes and Induced Gravitational Waves from a Smooth Crossover beyond Standard Model*, [2311.17760](#).
- [399] A. Escrivà, R. Inui, Y. Tada and C.-M. Yoo, *The LISA forecast on a smooth crossover beyond the Standard Model through the scalar-induced gravitational waves*, [2404.12591](#).
- [400] T. Suyama and M. Yamaguchi, *Non-Gaussianity in the modulated reheating scenario*, *Phys. Rev. D* **77** (2008) 023505 [[0709.2545](#)].
- [401] C. T. Byrnes, S. Nurmi, G. Tasinato and D. Wands, *Scale dependence of local f_{NL}* , *JCAP* **02** (2010) 034 [[0911.2780](#)].
- [402] C. T. Byrnes, M. Gerstenlauer, S. Nurmi, G. Tasinato and D. Wands, *Scale-dependent non-Gaussianity probes inflationary physics*, *JCAP* **10** (2010) 004 [[1007.4277](#)].
- [403] W. J. Handley, M. P. Hobson and A. N. Lasenby, *PolyChord: nested sampling for cosmology*, *Mon. Not. Roy. Astron. Soc.* **450** (2015) L61 [[1502.01856](#)].
- [404] W. J. Handley, M. P. Hobson and A. N. Lasenby, *POLYCHORD: next-generation nested sampling*, *Mon. Not. Roy. Astron. Soc.* **453** (2015) 4384 [[1506.00171](#)].
- [405] H. Akaike, *A new look at the statistical model identification*, *IEEE Trans. Automatic Control* **19** (1974) 716.
- [406] S. R. Geller, W. Qin, E. McDonough and D. I. Kaiser, *Primordial black holes from multifield inflation with nonminimal couplings*, *Phys. Rev. D* **106** (2022) 063535 [[2205.04471](#)].
- [407] W. Qin, S. R. Geller, S. Balaji, E. McDonough and D. I. Kaiser, *Planck constraints and gravitational wave forecasts for primordial black hole dark matter seeded by multifield inflation*, *Phys. Rev. D* **108** (2023) 043508 [[2303.02168](#)].
- [408] G. Autieri and M. Redi, *Reconstructing the Inflaton Potential: Primordial Black Holes and Gravitational Waves in Slow Roll and Ultra Slow Roll Single Field Inflation*, [2408.12587](#).
- [409] N. Bartolo, D. Bertacca, V. De Luca, G. Franciolini, S. Matarrese, M. Peloso et al., *Gravitational wave anisotropies from primordial black holes*, *JCAP* **02** (2020) 028 [[1909.12619](#)].
- [410] LISA COSMOLOGY WORKING GROUP collaboration, *Probing anisotropies of the Stochastic Gravitational Wave Background with LISA*, *JCAP* **11** (2022) 009 [[2201.08782](#)].
- [411] J.-P. Li, S. Wang, Z.-C. Zhao and K. Kohri, *Primordial non-Gaussianity f_{NL} and anisotropies in scalar-induced gravitational waves*, *JCAP* **10** (2023) 056 [[2305.19950](#)].
- [412] P. Kidger, *On Neural Differential Equations*, Ph.D. thesis, University of Oxford, 2021.
- [413] L. T. Witkowski, *SIGWfast: a python package for the computation of scalar-induced gravitational wave spectra*, [2209.05296](#).
- [414] J. Torrado and A. Lewis, “Cobaya: Bayesian analysis in cosmology.” Astrophysics Source Code Library, record ascl:1910.019, Oct., 2019.
- [415] M. J. Williams, *nessai: Nested sampling with artificial intelligence*, Feb., 2021. [10.5281/zenodo.4550693](#).

- [416] M. J. Williams, J. Veitch and C. Messenger, *Nested sampling with normalizing flows for gravitational-wave inference*, *Phys. Rev. D* **103** (2021) 103006 [[2102.11056](#)].
- [417] M. J. Williams, J. Veitch and C. Messenger, *Importance nested sampling with normalising flows*, [2302.08526](#).
- [418] A. Lewis and S. Bridle, *Cosmological parameters from CMB and other data: A Monte Carlo approach*, *Phys. Rev.* **D66** (2002) 103511 [[astro-ph/0205436](#)].
- [419] A. Lewis, *Efficient sampling of fast and slow cosmological parameters*, *Phys. Rev.* **D87** (2013) 103529 [[1304.4473](#)].
- [420] J. El Gammal, N. Schöneberg, J. Torrado and C. Fidler, *Fast and robust bayesian inference using gaussian processes with gprry*, *Journal of Cosmology and Astroparticle Physics* **2023** (2023) 021.
- [421] J. Torrado, N. Schöneberg and J. El Gammal, *Parallelized acquisition for active learning using monte carlo sampling*, 2023.
- [422] A. Lewis, *GetDist: a Python package for analysing Monte Carlo samples*, [1910.13970](#).